Numerical Investigation of the Effect of Scaling on the Performance of Large Scale Axial Flow Fans

by
Timo W. Meissner

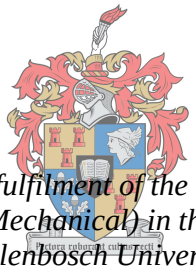

Thesis presented in partial fulfilment of the requirements for the degree of Master of Engineering (Mechanical) in the Faculty of Engineering at Stellenbosch University

UNIVERSITEIT
iYUNIVESITHI
STELLENBOSCH
UNIVERSITY

"The financial assistance of the National Research Foundation (NRF) towards this research is hereby acknowledged. Opinions expressed and conclusions arrived at, are those of the author and are not necessarily to be attributed to the NRF."

Supervisor: Prof S.J. van der Spuy
Co-supervisor: Prof C.J. Meyer

December 2018

Declaration

By submitting this thesis electronically, I declare that the entirety of the work contained therein is my own, original work, that I am the sole author thereof (save to the extent explicitly otherwise stated), that reproduction and publication thereof by Stellenbosch University will not infringe any third party rights and that I have not previously in its entirety or in part submitted it for obtaining any qualification.

Date: December 2018

UNIVERSITEIT·STELLENBOSCH·UNIVERSITY
jou kennisvennoot • your knowledge partner

Plagiaatverklaring / Plagiarism *Declaration*

1 Plagiaat is die oorneem en gebruik van die idees, materiaal en ander intellektuele eiendom van ander persone asof dit jou eie werk is.
Plagiarism is the use of ideas, material and other intellectual property of another's work and to present is as my own.

2 Ek erken dat die pleeg van plagiaat 'n strafbare oortreding is aangesien dit 'n vorm van diefstal is.
I agree that plagiarism is a punishable offence because it constitutes theft.

3 Ek verstaan ook dat direkte vertalings plagiaat is.
I also understand that direct translations are plagiarism.

4 Dienooreenkomstig is alle aanhalings en bydraes vanuit enige bron (ingesluit die internet) volledig verwys (erken). Ek erken dat die woordelikse aanhaal van teks sonder aanhalingstekens (selfs al word die bron volledig erken) plagiaat is.
Accordingly all quotations and contributions from any source whatsoever (including the internet) have been cited fully. I understand that the reproduction of text without quotation marks (even when the source is cited) is plagiarism.

5 Ek verklaar dat die werk in hierdie skryfstuk vervat, behalwe waar anders aangedui, my eie oorspronklike werk is en dat ek dit nie vantevore in die geheel of gedeeltelik ingehandig het vir bepunting in hierdie module/werkstuk of 'n ander module/werkstuk nie.
I declare that the work contained in this assignment, except where otherwise stated, is my original work and that I have not previously (in its entirety or in part) submitted it for grading in this module/assignment or another module/assignment.

Studentenommer / *Student number*	**Handtekening / *Signature***
Voorletters en van / *Initials and surname*	**Datum / *Date***

Abstract

Numerical Investigation of the Effect of Scaling on the Performance of Large Scale Axial Flow Fans

T.W. Meissner

Department of Mechanical and Mechatronic Engineering,
University of Stellenbosch,
Private Bag X1, Matieland 7602, South Africa.

Thesis: MEng (Mech)

December 2018

Large-scale axial flow fans are utilised in air-cooled heat exchanger systems in power plants. Due to the size of these fans, their performance cannot be experimentally tested. A common practice is to test a smaller, scaled-down version of the fan in a fan test facility and use the results to determine the performance of the large scale fan. Improving the accuracy of the scaled fan performance allows for a more accurate assessment of the fan performance and subsequently of the efficiency of the power plant.

The parameters influencing fan performance and their variation in magnitude with scaling are investigated. The performance of the Pelz scaling method for up- and down-scale scenarios compared to experimental data is assessed. The results show that the scaling method over-predicts the change in efficiency. The accuracy of a CFD analysis compared to experimental results of the B2a-fan at different sizes is investigated, showing an over-prediction of the numerical results at low flow rates and a under-prediction at high flow rates. The numerical results of a 0.63 m, 1.542 m and 9 m diameter B2a-fan show an increase in fan static efficiency and -pressure with fan size. Due to the similarity set between the fans, the Reynolds number range over the blade span increases with an increase in fan size. An increase in fan size and thus Reynolds number over the fan blade results in a logarithmic increase in fan static efficiency. As a result the increase in efficiency between the 0.63 m and 1.542 m diameter B2a-fan is about the same as the increase in efficiency between the 1.542 m and 9 m diameter fan, even though the increase in size of the later is more than double the size increase from 0.63 m to 1.542 m.

A two dimensional analysis investigating the accuracy of the turbulence models and the effect of Reynolds number on the lift and drag characteristics of an airfoil is conducted. The analysis showed an over-prediction in lift and drag by the Realizable k-ε turbulence model. The Spalart Allmaras turbulence model produces results with a much smaller deviation to the experimental results. A numerical analysis of the B2a-fan using the Spalart Allmaras turbulence model does, however, not reduce the deviation between the numerical- and experimental results. It is observed that the change in lift-to-drag ratio of the two-dimensional airfoil over a change in Reynolds number produces a similar trend than the results of the peak fan static efficiency over a change in Reynolds number in the three-dimensional analysis. The fan static efficiency is a function of the lift-to-drag ratio. A comparison showed that three-dimensional losses have a greater effect on the total losses at a high Reynolds number than at a low Reynolds number.

Uittreksel

Numeriese Ondersoek na die Effek van Skaal op die Verrigting van Grootskaalse Aksiale Vloei Waaiers

("Numerical Investigation of the Effect of Scaling on the Performance of Large Scale Axial Flow Fans")

T.W. Meissner

Departement Meganiese en Megatroniese Ingenieurswese,
Universiteit van Stellenbosch,
Privaatsak X1, Matieland 7602, Suid Afrika.

Tesis: MIng (Meg)

Desember 2018

Grootskaal aksiale vloei waaiers word in lugverkoelde hitteruilerstelsels in kragsentrales gebruik. As gevolg van die grootte van hierdie waaiers, kan hulle werkverrigting nie eksperimenteel getoets word nie. 'n Algemene praktyk is om 'n kleiner, afgeskaalde weergawe van die waaier in 'n waaier toetsfasiliteit te toets en die resultate te gebruik om die werkverrigting van die grootskaalse waaier te bepaal. Verbetering van die akkuraatheid van die skaalwaaier werkverrigting kan 'n meer akkurate assessering van die waaier werkverrigting en vervolgens van die doeltreffendheid van die kragstasie teweeg bring.

Die parameters wat die werkverrigting van die waaiers beïnvloed en hul variasie in grootte met skalering word ondersoek. Die prestasie van die Pelz-skaalmetode vir op- en af-skaal scenario's in vergelyking met eksperimentele data word beoordeel. Die resultate toon dat die skaalmetode die verandering in statiese doeltreffendheid oorvoorspel. Die akkuraatheid van 'n CFD-analise in vergelyking met die eksperimentele resultate van die B2a-fan in verskillende groottes word ondersoek, wat 'n oorvoorspelling van die numeriese resultate toon by lae vloeitempo's en 'n ondervoorspelling by hoë vloeitempo's. Die numeriese resultate van 'n 0.63 m, 1.542 m en 9 m deursnee B2a-fan wys 'n toename in die statiese doeltreffendheid en druk van die waaier met waaiergrootte. Vanweë die gelyksoortgelyk tussen die waaiers styg die Reynoldsgetalreeks oor die lemspan met 'n toename in waaiergrootte. 'n Toename in waaiergrootte en dus Reynolds getal oor die waaierlem lei tot 'n logaritmiese

toename in die waaier statiese doeltreffendheid. Gevolglik is die toename in doeltreffendheid tussen die 0.63 m en 1.542 m deursnee B2a-waaier ongeveer dieselfde as die toename in doeltreffendheid tussen die 1.542 m en 9 m deursnee waaier, alhoewel die toename in die grootte van die laasgenoemde meer as dubbel is as dié van 0,63 m na 1,542 m.

'n Tweedimensionele analise wat die akkuraatheid van die turbulensiemodelle en die effek van Reynolds-getal op die hef- en sleurkarakteristieke van 'n vleuelprofiel ondersoek het, is uitgevoer. Die analise het 'n oorvoorspelling in hef en sleur deur die 'Realizable' k-ε turbulensie model gewys. Die Spalart Allmaras-turbulensie model het resultate opgelewer met 'n veel kleiner afwyking van die eksperimentele resultate. 'n Numeriese analise van die B2a-fan met behulp van die Spalart Allmaras turbulensie model het egter nie die afwyking tussen die numeriese en eksperimentele resultate verminder nie. Daar is opgemerk dat die hef-tot-sleur-verhouding met 'n verandering in Reynolds-getal 'n soortgelyke tendens lewer as die resultate van die statiese doeltreffendheid van die waaier se verandering as gevolg van 'n verandering in Reynolds-getal. Die statiese doeltreffendheid van die waaier is 'n funksie van die hef-tot-sleur-verhouding. 'n Vergelyking het getoon dat driedimensionele verliese 'n groter effek het op die totale verliese teen 'n hoë Reynolds-getal as by 'n lae Reynolds-getal.

Acknowledgements

I would like to express my sincere gratitude to the following people and organisations:

Prof. S.J. van der Spuy and Prof C.J. Meyer for their support and guidance throughout the duration of this thesis. Thank you for your advice and teaching me to think more critically.

My family and friends for their continued support and encouragement.

The National Research Foundation (NRF) for their financial support.

Contents

List of Figures

List of Tables

Nomenclature

Variables

c	Coefficient	[ ]
ch	Chord length	[m]
D	Diameter	[m]
F	Force	[N]
i	Incidence angle	[°]
L	Characteristic length	[m]
$\dot{m}$	Mass flow rate	[kg/s]
Ma	Mach number	[ ]
N	Rotational speed	[rpm]
P	Pressure	[Pa]
r	Radius	[m]
Re	Reynolds number	[ ]
s	Blade span / blade spacing	[m]
S	Strain rate tensor	[s^{-1}]
t	Tip clearance	[m]
T	Torque	[N·m]
U	Velocity	[m/s]
V	Volume	[m^3]
$\dot{V}$	Volumetric flow rate	[m^3/s]

Greek symbols

α	Angle of attack	[°]
β	Air inlet angle	[°]
γ	Blade setting angle	[°]
ϵ	Inefficiency	[%]
ε	Surface roughness	[mm]
ζ	Stagger angle	[°]
η	Efficiency	[%]

κ	Von Kármán constant	[ ]
μ	Dynamic viscosity	[kg/m·s]
ρ	Density	[kg/m^3]
φ	Flow coefficient	[ ]
ω	Rotational speed	[rad/s]
Γ	Power coefficient	[ ]
Δ	Differential	[ ]
Ψ	Pressure coefficient	[ ]
Ω	Mean vorticity	[s^{-1}]

Subscripts

a	Axial
c	Circumference
d	Drag
f	Surface/skin friction
fs	Fan Static
L	Lift
m	Model
o	Optimum
p	Prototype
r	Relative

Chapter 1

Introduction

1.1 Background

Axial flow fans are primarily used for cooling and ventilation purposes, finding applications in electronic equipment, vehicles (radiators, intercoolers), temperature regulators (air-conditioners, ceiling fans) and industrial heat exchangers (Kröger, 1998). The size of these fans can vary from a 50 mm diameter cooling fan, found in laptops, to a 14.63 m (48 ft) diameter fan, typically used in air-cooled heat exchanger systems in power plants (Augustyn, 2013).

The fan efficiency and performance of two geometrically similar fans of different diameters typically differs. This is mainly attributed to the difference in Reynolds number for the flow over the fan blades, which causes dissimilar boundary layers between the two fans (Grimes *et al.*, 2005). A large diameter fan, such as the 14.63 m fan mentioned above, cannot be tested in a fan test facility due to its size. A smaller fan is thus tested and the results extrapolated to predict the performance of the large diameter fan. The large size difference between the fan that can be tested in a fan test facility and the large-scale model means that matching the Reynolds number of the two different sized fans is often not possible. Therefore it is crucial to accurately predict and quantify any differences in fan performance resulting from the scaling of fans and formulate a method that can accurately scale the performance of the smaller test fan to predict the performance of the large fan.

Air-cooled heat exchangers and condensers, in which large scale axial flow fans are typically used, belong to thermal discharge systems, which dissipate excess heat to a low temperature fluid medium. This fluid medium is typically air or water but can also be refrigerant or oil (Kröger, 1998). Dry- or air-cooled systems utilize air instead of water as a cooling medium. Axial flow fans are used to force the air over the heat exchanger bundles, transferring the heat from the heat exchangers to the air. Such as system is called a direct

air-cooled system or a mechanical draft system. The rate of heat transfer to the air directly influences the efficiency of the thermodynamic cycle. (Kröger, 1998)

$$\eta = \frac{W_{out}}{Q_{in}} \tag{1.1}$$

The efficiency of a thermodynamic cycle is determined by the ratio of output energy to input energy, as given by Equation 1.1. In a thermodynamic cycle in which heat energy is converted to mechanical energy the output energy is the work output of the turbine. The work output of the turbine is a function of the inlet and outlet pressure difference of the turbine.

A decrease in the rate of heat rejection (Q_{out}), due to the action of axial flow fans in an air-cooled condenser (ACC), and the subsequent decrease in the rate of steam condensation causes the steam condensation temperature to increase. As a result the steam back pressure increases. The increased back pressure reduces the work output, decreasing the process efficiency, as demonstrated by Equation 1.1. A further increase in back pressure will lead to the plant having to reduce the load (decrease Q_{in}) to prevent turbine trip and damage to the rear stages of the turbine. Therefore the efficiency of the condenser, and in effect the axial flow fan, is imperative for the efficiency of the thermodynamic cycle, as well as the plant integrity.

A typical direct air-cooled condenser (ACC) setup used in power plants consists of a rectangular array of axial cooling fans with an A-frame, forced draft, heat exchanger setup, as shown in Figure 1.1 & 1.2. The finned tube bundles of the A-frame heat exchanger are sloped at an angle in order to increase the surface area of the heat exchanger (Kröger, 1998). Steam exiting the turbine, flows through the steam header and down through the finned tubes that make up the heat exchanger bundles. Ambient air is forced over and past the finned tubes by the axial flow fans. The air cools the steam inside the finned tubes, causing the steam to condense to water. The water is pumped back to the boiler in which the water is converted to steam again. This forms a closed process with minimal water losses. The layout of the process is shown in Figure 1.1.

Utilizing air instead of water as a cooling medium, makes dry-cooled systems very attractive for use in semi-arid and arid regions, in which the water supply is expensive or its availability is limited. With 72% of South Africa receiving an annual rainfall below 600 mm, water availability is a constant concern (Palmer and Ainslie, 2006). The majority of newly built and cur-

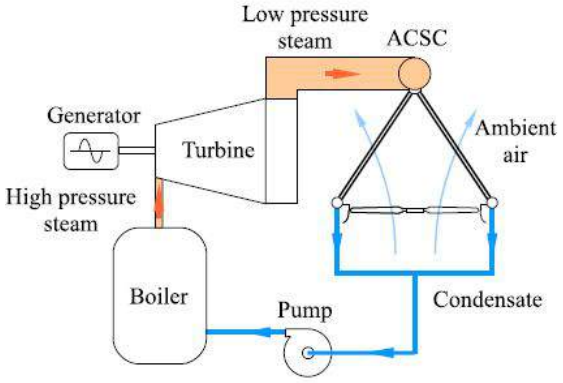

Figure 1.1: A typical direct air-cooled steam cycle used for electricity generation

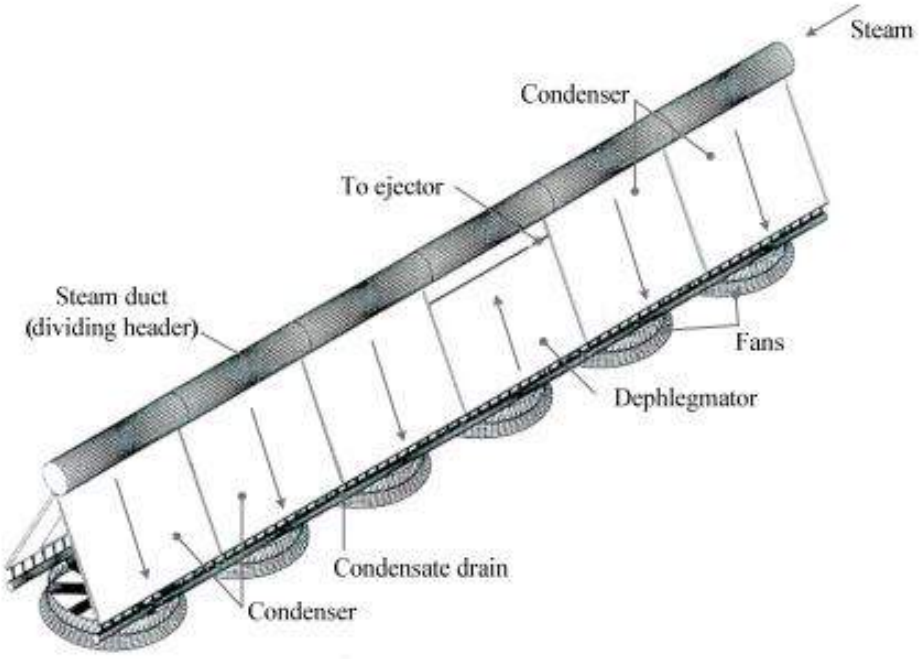

Figure 1.2: Schematic of an A-frame, dry-cooled condenser street

rently constructed power stations in South Africa are located in water scarce regions, thus the use of wet cooled systems is not feasible from an environmental and economical perspective (Augustyn, 2013). According to Tindale and Sagris (2013), direct air-cooled systems, utilizing axial flow fans, consume in average 0.1 litres of water per kWh of electricity produced, while wet-cooled systems consume 20 times more, with an average consumption of 2 liters per kWh. This water saving characteristic makes dry-cooled systems suitable for solar thermal power plants, as they are typically located in arid regions with

very little water availability. Ndebele (2015) states that, apart from one, all South African concentrated solar power (CSP) plants use dry-cooled systems, which result in a 90 % water saving compared to a wet cooled system.

Figure 1.3, given by Lennon (2011), shows that the combined water consumption of the power stations in South Africa has significantly decreased with an increased application of dry-cooling systems.

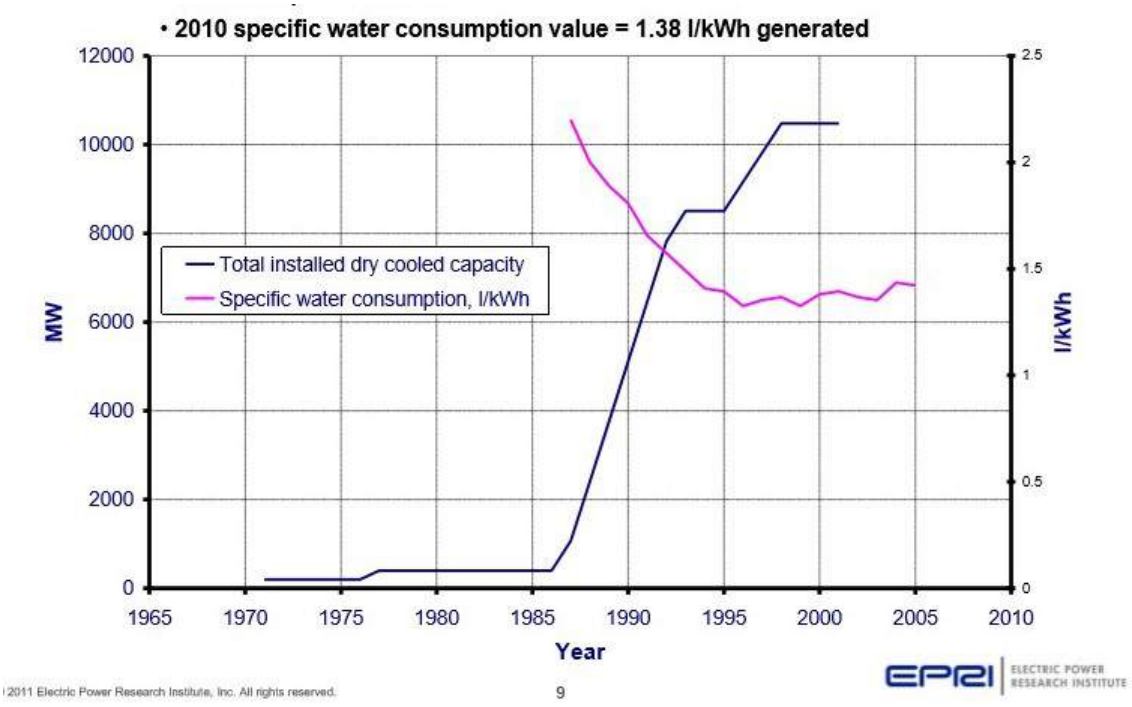

Figure 1.3: Impact of increased dry-cooled systems in South African power plants on the specific water consumption (Lennon, 2011)

The trade-offs to the significant water saving of the dry-cooled system are higher capital and operating costs and a lower overall process efficiency compared to a wet-cooled system. An estimation by Eskom predicts that the capital cost of a dry-cooled system is 70% higher than the capital cost of an equivalent wet-cooled system. The use of a direct dry-cooled system requires more auxiliary power than other systems. On average 2% of the total energy capacity is used to power the cooling fans. In the case of the South African Medupi coal power station the auxiliary power of the dry-cooled system can be up to 12.4 MWe of 4.8 GWe output. The use of air as a cooling medium results in a greater sensitivity to meteorological factors such as dry-bulb temperature, humidity and wind, resulting in a reduction of 10 to 15% in generation capacity.

Overall process efficiency is also lower in dry-cooled systems, since lower process temperatures can be reached with wet-cooling. (Tindale and Sagris, 2013)

It is the lower plant efficiency and generation capacity that creates a need to improve the efficiency of dry-cooled ACC's, specifically improving the performance and effectiveness of the axial cooling fans. Improving the fan performance decreases the operational cost and the environmental footprint of the thermodynamic process. Accurately predicting the performance of large scale fans is therefore essential. Since the size of the axial flow fans, used in the dry-cooled systems, permits testing of the fans in the controlled environment provided by a fan test facility, the fan performance of a large-scale fan must be accurately determined by assessing a scaled-down version of the fan. It is therefore important to identify and account for differences in losses and flow structures that occur due to a difference in fan size.

1.2 Research objectives and approach

The objectives of this study are:

- **Obtaining a better understanding of the existing axial flow fan scaling laws.**

  Identify existing scaling laws and assess their advantages and shortcomings. Assess the performance of these scaling laws with regard to the B2a-fan.

- **Determine and assess the parameters influencing the performance of small and large scale axial flow fans**

  To obtain a better understanding of the scaling effect, the factors influencing the performance of axial flow fans need to be determined and their role assessed. The effect of the change in flow regime, i.e. the difference in scaled performance due to propagation from a laminar to a turbulent flow regime and vice versa is investigated.

- **Assess the relative accuracy of CFD predicted fan performance**

  A computational fluid dynamic (CFD) model of fans of different sizes is constructed. The accuracy of the numerical results, compared to experimental results of the fans is determined. The difference in fan performance for variation in fan size is also assessed. For a more accurate assessment of fan performance, the performance is established not only at the design and peak efficiency point but also at off-design conditions.

- **Develop an improved scaling law for axial flow fans**

  The numerical and experimental fan performance prediction results will be used to improve the accuracy of existing fan laws.

The project is based on the B2a-fan which was developed by Bruneau (1994) and modified by Louw *et al.* (2012). The fan is designed specifically for use in ACHEs. The 1.542 m diameter model is shown in Figure 1.4. The specifications and further detail of the fan are given in Appendix A.

Figure 1.4: The model of the B2a-fan installed in the testing facility at the University of Stellenbosch

To fulfill the project objectives, the following approach is implemented:

- **Numerical modelling of a simplified domain and a full flow domain**

  A three-dimensional flow simulation is performed using ANSYS computational fluid dynamics (CFD) software. One of eight blades of the B2a-fan is modelled based on the assumption that the flow is rotationally periodic. As a result a periodic three-dimensional model with periodic sides and a single fan blade is created.

  The numerical analysis is conducted in three stages. A ducted domain with a constant height is modelled first, providing low complexity and

a relative small mesh size and short computational time. The flow and mesh complexity is increased in the second stage by including a blade tip clearance. In the final stage the inlet and outlet domain are build such as to resemble the British standard BS 848 type A fan test facility. In this model a ball-nose hub and bell mouth shroud is included.

- **Numerical modelling of three B2a-fans of different sizes**

  A 0.63 m, 1.542 m and a 9 m diameter axial fan are modelled using CFD. The 0.63 m and the 9 m fans are scaled copies of the 1.542 m fan model. The performance of each fan is assessed and a comparison is made between the three different sized fans.

- **Numerical modelling at different flow conditions**

  The fan performance of each of the different sizes of fans modelled is determined for a range of volumetric flows.

1.3 Framework of the study

This study will proceed with an analysis of the relevant literature in Chapter 2. Previous studies, conducted by Conradie (2010) and Louw (2015), have focused on the experimental testing of individual small-scale fans in a fan test facility. In Chapter 3 the experimental setup of these studies will be examined. In contrast, this study is based on CFD modelling. Chapter 4 will outline the CFD configuration used in this scaling exercise. In the following chapter the results are provided and a comparison between the CFD method of this study and the previously conducted experimental testing is drawn. The study will conclude with a brief discussion of the results and recommendation for future work.

Chapter 2

Literature study

The literature study provides an overview of the research done in the field of scaling axial fans and provides background information and explanation of key concepts.

2.1 Fan similarity

To allow the performance of fans at different size, speed or different flow conditions, such as air temperature and density, to be comparable a form of similarity between the fans must exist (Pelz and Hess, 2010). This forms the principle of scaling and the basis of scaling laws.

Three forms of similarity exist, as pointed out by the BS 848-1:2007 standard for industrial fans:

1. Geometric similarity
2. Kinematic similarity
3. Dynamic similarity

Full similarity is achieved when all three similarity forms are fulfilled and thus the dimensional products of the model and prototype are identical (Pelz and Hess, 2010).

Geometric similarity is the dimensional similarity between a model and prototype. The dimensions such as diameter, blade thickness, -chord length, tip clearance, etc. must all differ by an identical scaling factor. All corresponding angles between a model and prototype must be equal. (British Standard, 2007)

Kinematic similarity is achieved when the velocity vector magnitudes at corresponding points of the model and prototype differ by a constant factor and are pointed in the same direction. To fulfil kinematic similarity the model and prototype must have the same length- and time scale ratio, which translates to the velocity scale ratio to be equal. The similarity of velocity magnitude and direction causes the streamline pattern in the model flow to be a scaled copy of the prototype flow. Kinematic similarity is automatically achieved if both geometric and dynamic similarity exists. (Cengel and Cimbala, 2010)

Mach number equality between the model and prototype is relevant when the compressibility effect is prominent, which is for a Mach number (Ma) above 0.15, according to the BS 848-1:2007 standard. Most scaling laws do not consider compressibility effects. Separate Mach number scaling laws have to be used for such cases. For Ma $<$ 0.15, fan performance and efficiency will increase with an increase in Mach number. For Ma $>$ 0.15 the compressibility of flow causes additional losses due to the increase in the density of the flow. The fan performance and efficiency will thus stagnate and then deteriorate for a further increase in Mach number. The effect depends on the blade geometry, -angle and operating point of the fan (Saul and Pelz, 2016).

Dynamic similarity is achieved if all forces at a corresponding point on the model and prototype differ by a constant scaling factor. Dynamic similarity exists when the model and prototype have the same length- time- and force scale ratio. This means that a model and prototype can achieve both geometric and kinematic similarity but may not achieve dynamic similarity. A model can therefore be geometrically similar and have scaled velocity triangles but this does not necessarily result in equal Reynolds number (Cengel and Cimbala, 2010). Similarity of the Reynolds number results in equal relative boundary layer thickness, velocity profiles and friction losses between the model and prototype. (British Standard, 2007)

2.2 Reynolds number effect

To ensure complete dynamic similarity, the Reynolds number and the Mach number of the model must be equal to the Reynolds number and Mach number of the prototype at the corresponding location, as shown in Equation 2.1. If the Mach number is smaller than 0.15, the compressibility effects are negligible, in which case Reynolds number equality between the model and prototype is sufficient for dynamic similarity.

$$Re_m = \frac{\rho_m U_m L_m}{\mu_m} = \frac{\rho_p U_p L_p}{\mu_p} = Re_p \tag{2.1}$$

The tip speed of the fan blade at a specified radius, r, is defined as follows:

$$U = \frac{2\pi N r}{60} \tag{2.2}$$

Since it can be assumed that the temperature, hence the density (ρ) and dynamic viscosity (μ) of the model and prototype are the same, the only two variables that influence the Reynolds number similarity, as indicated by equation 2.1, is the velocity (U) and the characteristic length (L) of the blades. The velocity is dependent on the rotational speed of the blade (N), as shown in Equation 2.2, and the chord length (ch) of the blade is used as the characteristic length (L). Therefore, in order to match the Reynolds number of two fans at different sizes, the rotational speed of the smaller fan model has to be significantly larger to make up for its shorter chord length. For a large-scale fan with a diameter of 9 m, a chord length of 0.893 m and rotating at a speed of 125 rpm, for example, the geometrically scaled 1.542 m diameter fan needs to rotate at a speed of 4258 rpm in order to achieve the same Reynolds number flow. This equates to a Mach number of 0.99 at the fan tip, which is far above the 0.15 Mach number threshold above which compressibility effects occur. Therefore, in addition to equal Reynolds number between the model and prototype, the Mach number of the model must be equal to the Mach number of the prototype to account for the effects of compressibility. Due to the high rotational speed necessary to match the Reynolds number of the model to the Reynolds number of the prototype, dynamic similarity can be unfeasible in many cases.

A possibility is to extrapolate the fan performance of the small-scale fan to the Reynolds number of the full-scale fan. This is demonstrated in Figure 2.1. The extrapolation therefore enables performance predictions of a large scale prototype by using a smaller model. (Augustyn, 2013)

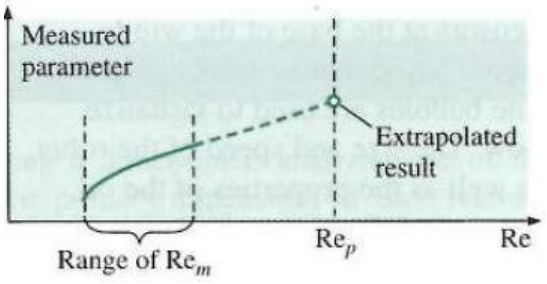

Figure 2.1: Extrapolation of test data of low Re model data to predict high Re prototype behaviour (Cengel and Boles, 2011)

A problem with the extrapolation, as set out by Bahrami (2009) is the high uncertainty in estimation, especially when the difference in Reynolds number between the model and prototype is large. This problem is shown in Figure 2.2. A large difference in Reynolds number can result in different flow regimes existing in the model and prototype. At a high Reynolds number the flow is in the turbulent flow regime while at low Reynolds number the flow is either in the transitional or laminar flow regime. The flow regime dictates the state of the boundary layer. The uncertainty is also caused by the disregard of frictional and Reynolds number effects by the conventional extrapolation / scaling laws, which are used to numerically scale the results of the model.

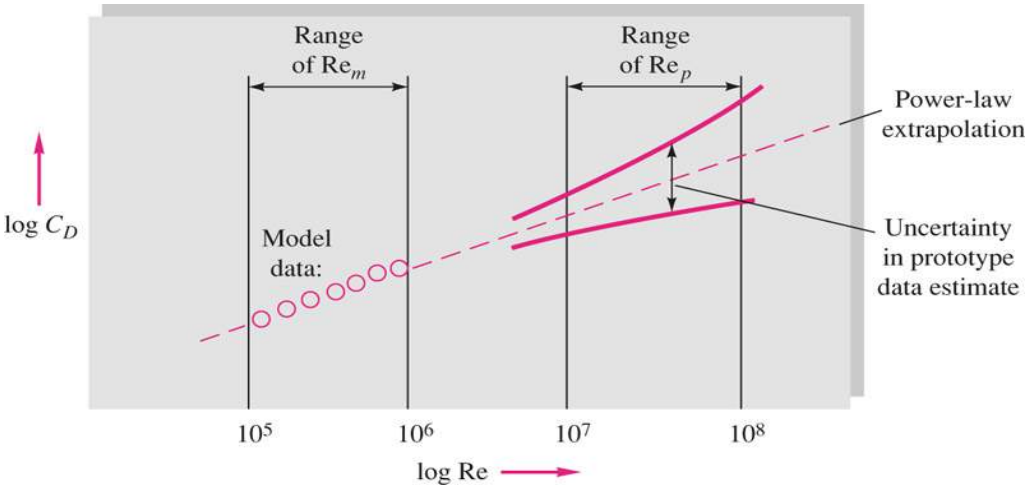

Figure 2.2: Variation of results caused by Reynolds number extrapolation (Bahrami, 2009)

Neglecting dynamic/Reynolds number similarity means that the similarity of the relative boundary layer thickness between the model and prototype is sacrificed. The difference in boundary layer results in dissimilar losses and thus dissimilar fan performance.

Setting the tip speed of the model equal to the tip speed of the prototype results in equal velocity vectors and thus equal Mach numbers in both the model and prototype at a particular position along the span of the blade. The Reynolds number between two different sized fans is thus only dependent on the chord length of the blade and, as a consequence, differs solely by the geometric scaling factor.

$$Re = \frac{Inertial forces}{Viscous forces} \tag{2.3}$$

The Reynolds number expresses the ratio of inertial forces to viscous forces, as shown in Equation 2.3. This means that the magnitude of the relative losses will be reduced with an increase in Reynolds number, due to the dominance of the inertial forces. As the Reynolds number decreases, the viscous forces increase in dominance, resulting in an increase in losses. Thus, as shown in Figure 2.3, the fan efficiency is reduced by a decrease in Reynolds number.

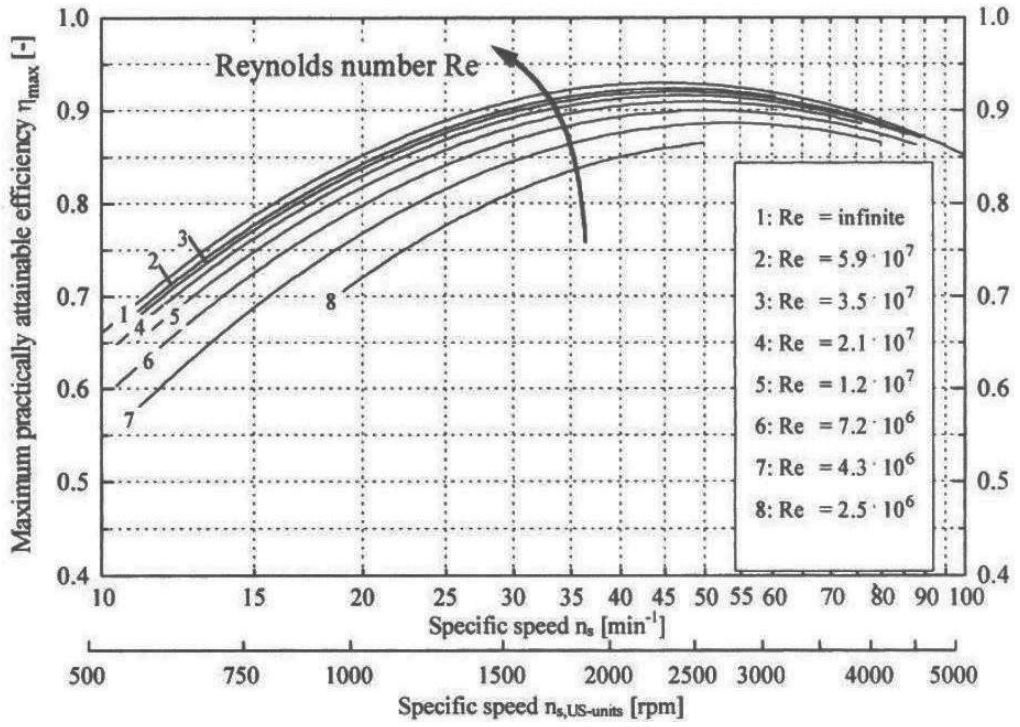

Figure 2.3: The effect of Reynolds number and specific speed on the fan performance (Pelz *et al.*, 2012)

Figure 2.3 also shows that fan efficiency is particularly sensitive to Reynolds number at a low specific speed, while the effect of Reynolds number on efficiency is small at a high specific speed. This is due to the fact that the boundary layer thickness decreases with higher rotational speed. At a high specific speed approximately the same efficiency is achieved, irrespective of the Reynolds number (Grimes *et al.*, 2005). As shown in Figure 2.4 the losses, quantified by the drag coefficient in this case, can vary considerably with a change in Reynolds number. From a certain point little to no change in results occurs with a further increase in Reynolds number. This means that the same drag coefficient is obtained, irrespective of the Reynolds number. This typically occurs when both the boundary layer and the wake are in the same flow regime.

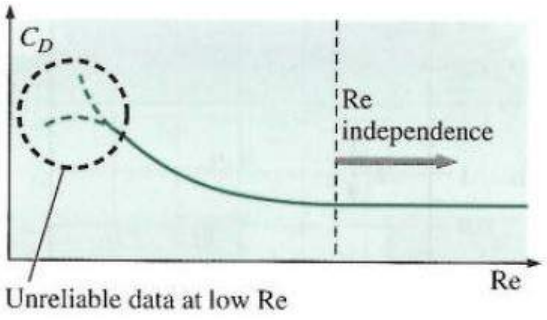

Figure 2.4: Reynolds number independence (Cengel and Cimbala, 2010)

Experimental testing of fans at varying rotational speeds and thus Reynolds number, conducted by Hess (2010) and Pelz *et al.* (2012), showed that the efficiency not only increases with an increase in Reynolds number, but the peak efficiency point also shifts to a higher flow coefficient. This is shown in Figure 2.5. The points of peak efficiency at different Reynolds number flows all align along a sloped straight line. Therefore it is evident that the proportional relation $\Delta\eta \propto \Delta\varphi$ is true. Shifting the curves along this straight line will produce a single curve, called the master efficiency curve. (Pelz *et al.*, 2012).

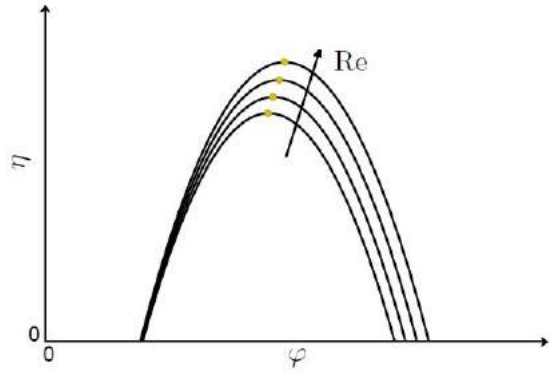

Figure 2.5: Effect of Reynolds number and flow coefficient on the fan efficiency(Hess, 2010)

The reason for the shift of the peak efficiency point to a higher flow coefficient for an increase in Reynolds number is due to a change in air inlet flow angle (β), as explained by Figure 2.6.

The left-hand image in Figure 2.6 shows a cascade of fan blades with normalized velocity vectors. This is done by dividing all velocities by the circumferential velocity (U_c). This conveniently equates to the flow coefficient in the

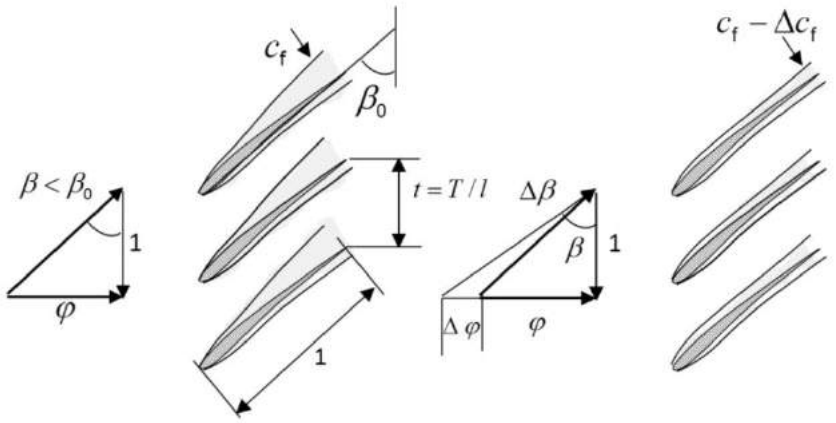

Figure 2.6: Boundary layer thickness due to lower (left image) and higher (right image) Reynolds number flow (Pelz *et al.*, 2012)

axial flow direction ($\varphi = U_a/U_c$). The optimum inlet angle (β_o) shown in Figure 2.6 is the angle of the relative flow at which the losses are at a minimum and as result a maximum fan static efficiency is achieved.

At a low flow coefficient with the air inlet angle (β) lower than the optimum inlet angle (β_o), as shown on the left-hand side of Figure 2.6, an increase in the boundary layer thickness on the suction side of the blade occurs. The thicker boundary layer leads to a wider blade wake and thus to a larger blade drag. This results in low fan efficiency. The effect of the wide blade wake is greater in fans with a smaller space between the blades, as in addition to the increase in blade drag the wide wake results in an obstruction of the flow between the blades.

In order to achieve maximum efficiency an optimal boundary layer thickness distribution between both sides of the blade must be present. This is achieved by increasing the inlet angle (β), as shown in the right-hand image in Figure 2.6. To increase the inlet angle (β), the axial velocity and hence the flow coefficient must increase ($\Delta\varphi$). An increase in air inlet angle past the optimum angle (β_o) will create a thicker boundary layer on the opposite side of the blade. The efficiency will thus decrease for a further increase in axial velocity and hence flow coefficient. (Pelz *et al.*, 2012)

Increasing the rotational speed of the blades increases the relative velocity, which increases the Reynolds number over the fan blade, as shown in Figure 2.7(a). As a result of the increased fluid velocity over the fan blade, the boundary layer thickness decreases, thus increasing the fan efficiency. The boundary layer on the suction side of the blade still increases, as previously

discussed, due to the angle of the flow but the overall thickness of the boundary layer is reduced by the increased Reynolds number.

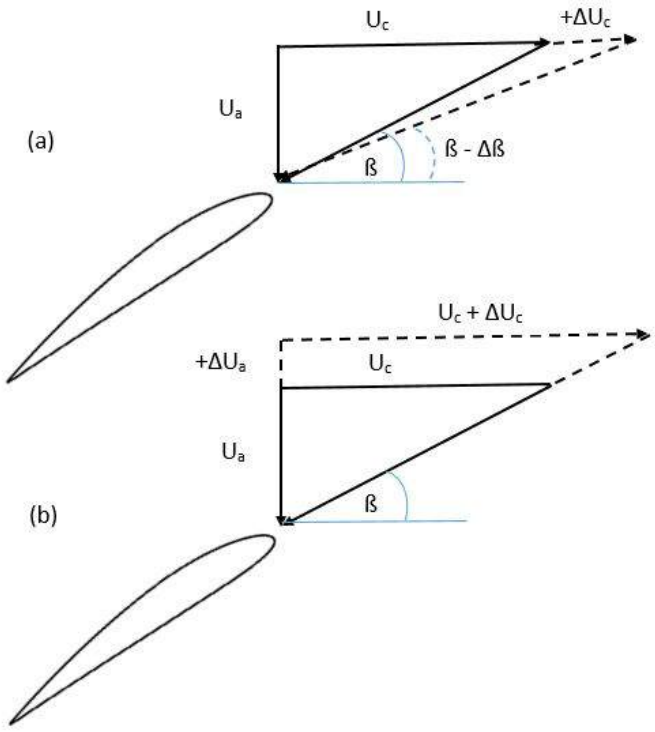

Figure 2.7: Change in air inlet angle (β) with a change in rotational speed (Uc) and subsequently Reynolds number

The increase in rotational speed of the blades increases the circumferential velocity component (U_c). As a result the air inlet angle (β) is reduced, as shown in Figure 2.7(a). To increase the inlet angle, the axial velocity and in effect the flow coefficient (φ) must increase, as shown in Figure 2.7(a). This means that for higher Reynolds number flow the optimum inlet angle (β_o), at which the peak efficiency is achieved, occurs at a higher flow coefficient (φ). Therefore the efficiency curve shifts to a higher flow coefficient at a higher Reynolds number, as shown in Figure 2.5.

Important to note, as pointed out by Hess (2010), is that the effect causing the shift of the efficiency curve is the greatest for flow in the laminar regime. For turbulent flow the friction effects are typically very small, therefore the majority of the losses occurring in the turbulent flow regime are Reynolds number independent, such as tip clearance losses. Therefore the rate at which the fan efficiency increases reduces as the Reynolds number of the flow increases. The increase in Reynolds number reduces the laminar flow region, thus a larger

portion of the blade is dominated by turbulent flow. This results in a smaller increase in efficiency and flow coefficient. More detail on Reynolds number dependent and independent losses will be covered in the following section.

2.3 Losses

As established in the previous sections, fans of different sizes will have significant differences in efficiency and performance. Therefore it is crucial to identify the types of losses occurring in an axial fan and understanding the behaviour of these losses during scaling.

A number of loss mechanisms exist, including tip vortex-, friction-, secondary flow-, incidence-, as well as boundary layer transition and separation losses. These losses are complex in nature and their magnitude is dependent on several factors such as blade airfoil, fan size and Reynolds number, among others (Hess, 2010). Thus the different loss components will behave differently as a result of fan scaling.

Losses are categorized into two types:

- Viscous losses / Reynolds number dependent losses
    - Friction losses
      Profile losses
      Annulus losses
    - Secondary losses
- Inertia losses / Reynolds number independent losses
    - Tip clearance losses
    - Incidence losses

Viscous losses are mainly caused by surface friction. The magnitude of the viscous losses change with both Reynolds number and flow coefficient. Profile-, annulus- and secondary losses all result from surface friction, which decreases with an increase in Reynolds number. Profile losses occur along the span of the blade, while the surface friction along the the hub and shroud surface is classified as the annulus loss. The viscous losses are directly associated with the boundary layer growth, thus the magnitude of the loss can change drastically with boundary layer separation. Separation of the boundary layer results in widening of the blade wake, leading to increased drag and flow blockage. The suction side of the blade is more prone to separation, thus higher aerodynamic losses are present on the suction side of the blade than on any

other surface. The hub annulus loss additionally depends on the blade spacing.

An important consideration in studying the frictional losses is the flow regime. As shown in Figure 2.8, the friction coefficient will decrease with an increase in Reynolds number, but will increase again as the flow regime changes from a laminar to a transitional and eventually to a turbulent flow regime. The Reynolds number at which the flow changes from a laminar to a turbulent state is called the critical Reynolds number. Depending on the surface roughness, expressed by the term: ε/L, the friction coefficient of the turbulent flow regime can decrease and increase several fold until the Reynolds number reaches the value at which the fully rough turbulence state is achieved. In this state the friction coefficient is independent of the Reynolds number and is solely a function of the relative roughness (ε/L) of the surface. (Cengel and Cimbala, 2010)

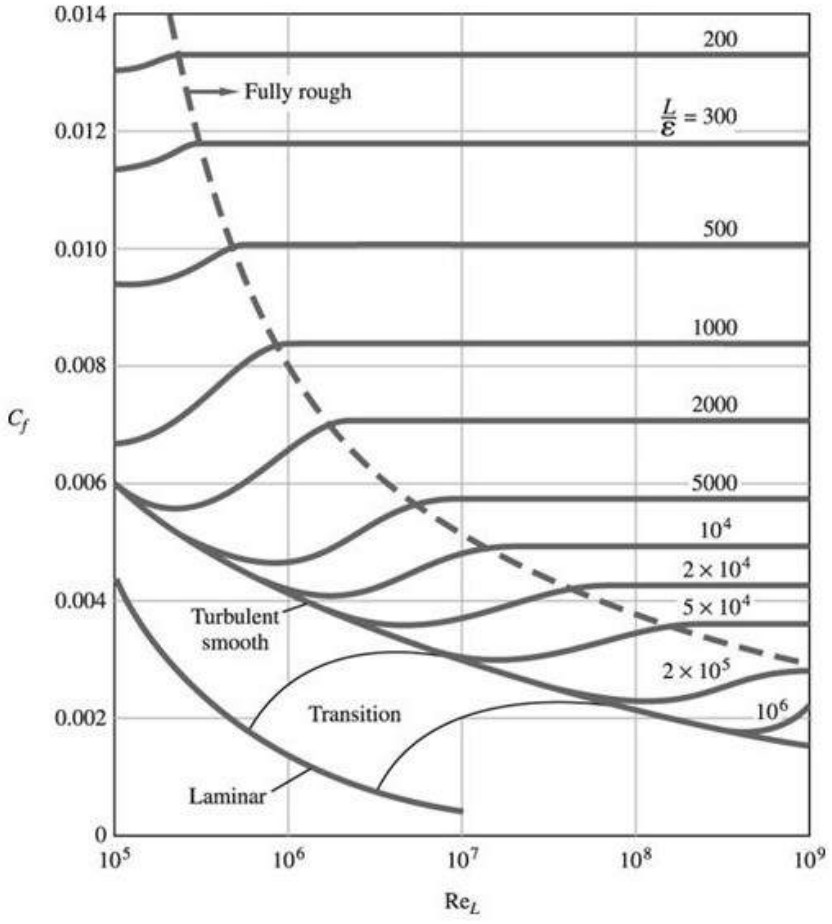

Figure 2.8: The variation of the friction coefficient with the Reynolds number for flow over a flat plate (Cengel and Cimbala, 2010)

The variation of the friction losses can cause a significant impact on the accuracy of scaling formulas (Pelz and Hess, 2010). Fans with a flow close to the critical Reynolds number can experience laminar flow in the region close to the hub, while the region close to the blade tip can experience turbulent flow. Accurately determining the point of transition, as well as the size of the laminar, transitional and turbulent region in the chord- and span-wise direction, is however difficult. It depends on multiple factors such as the velocity of the flow over the blade, the hub-to-tip ratio of the fan, the shape, size and angle of the blade, as well as the characteristics of the fluid, that is its density, viscosity, etc. (Cengel and Cimbala, 2010). The difficulty in predicting the flow regime can be seen in Figure 2.8. For a Reynolds number of 10^5 for example, the flow can be fully laminar but also turbulent smooth depending on the surface roughness. Due to the difficulty in accurately predicting the flow regime the majority of similarity and scaling formulas make the assumption of a fully turbulent flow, if the flow is close or above the critical Reynolds number of a flat plate (Pelz and Hess, 2010).

Secondary losses arise from circulation in the region around the trailing edge of the fan blades. Contrary to the majority of the viscous losses, secondary losses do not arise from friction. Due to the pressure difference between the two sides of the blade, the flow moves from the pressure side to the suction side and thus create vortices, which develop to a wake behind the trailing edge. This circulatory flow will gradually mix with the main passage flow behind the trailing edge of the blade. As a result a mixing loss occurs that is caused by viscous shear between the two flows with different velocities.

The magnitude of the secondary losses are dependent on the pressure difference between the two sides of the blade, which is dependent on the Reynolds number of the flow. The circulatory flow from the pressure to the suction side of the blade can facilitate boundary layer separation. Thus, secondary losses can influence the magnitude of profile loss.

The deflection of the flow from the blade surface decreases as the Reynolds number increases due to thinning of the boundary layer along the chord of the blade. As a result of the reduced flow deflection the flow blockage, and hence the losses, decrease. When the Reynolds number is reduced to the point of flow separation the flow will be deflected to a greater degree, significantly increasing flow deviation and blockage (Rhoden, 1952). The flow deflection along a blade is shown in Figure 2.9. The boundary layer growth and separation depends on the blade geometry, surface roughness and the flow conditions. (Patdiwala *et al.*, 2014)

Inertia or Reynolds independent losses do not change with Reynolds number. They do however change with flow coefficient. Since the axial fans are

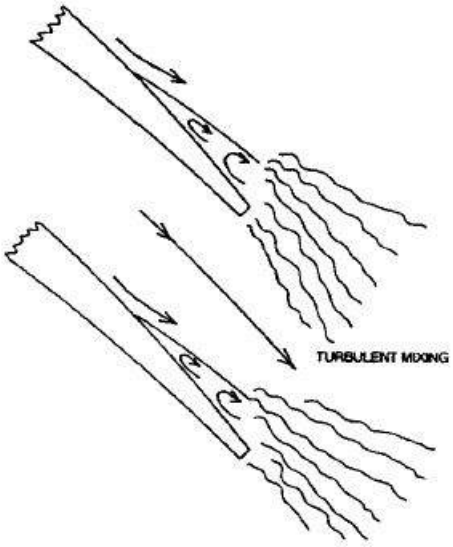

Figure 2.9: Visualization of boundary layer separation leading to a widening of the blade wake and subsequent flow blockage (Denton, 1993)

scaled, adhering to geometric and kinematic similarity, the Reynolds number is directly linked to the geometric scaling factor. Thus, the Reynolds independent losses are non-scalable (Hess, 2010). The inertia losses are dominant at high Reynolds number flow at which the influence of viscous losses is negligible. Inertia losses are typically inlet angle- and tip clearance losses.

Tip clearance losses arise due to flow leakage through the gap of the blade tip and the shroud. This flow leakage cause a reduction in the air passing the fan blades, thus a portion of the air is not accelerated by the fan, decreasing its efficiency. Besides flow leakage, a vortex is formed above the fan blade, which propagates downstream. The vortex is formed by the pressure difference between the pressure and the suction side of the blade. The mixing of the tip vortex with the main passage flow results in drag and flow blockage along the blade span, thus decreasing fan efficiency. Contrary to the secondary flow losses, which are also created by mixing of flows, the tip clearance losses are independent of the Reynolds number. This is because the wake of the secondary losses strongly depends on the boundary layer thickness along the span of the blade, while the tip clearance losses depend on the pressure difference between the two sides of the blade and the gap height. Increasing the Reynolds number causes a higher pressure difference between the two sides of the blade. This increases the tip clearance losses. However, according to Hess (2010) and Augustyn (2013) the increase is minimal such that the tip clearance losses can be regarded as Reynolds number independent.

Tip clearance losses result in a near constant reduction in fan static pressure

and efficiency at an increase in flow rate Augustyn (2013). This is, however, not necessarily true for large scale axial fans. The diameter of the fan shroud or casing in large scale fans is not necessarily constant due to the mere size of the shroud, especially for fans with a diameter of 9 m or more (Conradie, 2010). Thus, the tip clearance can vary with respect to the circumferential position of the blade. The varying tip clearance will have a significant impact at low flow rate and Reynolds number conditions.

Denton (1993) states that negligible change in tip clearance losses will occur for fans at different size if the ratio of the tip clearance to the blade thickness is equal. Two blades with different tip clearance to blade thickness ratio is shown in Figure 2.10.

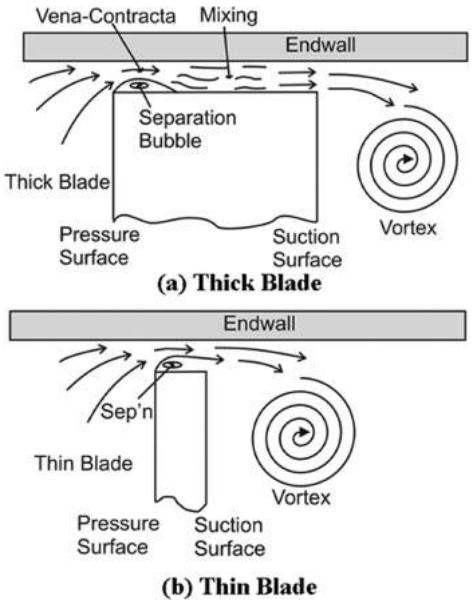

Figure 2.10: Tip clearance flow along the blade thickness (Denton, 1993)

Denton (1993) discussed the effect of the relative motion between the blade tip and the stationary shroud. It was found that the relative motion affected the pressure between the blade rather than the flow pattern. A vortex is formed by the relative motion between the blade tip and the shroud, resulting in an increased pressure on the suction side of the tip clearance gap. Thus, the pressure difference is reduced, decreasing the tip clearance losses. The tip clearance losses can also be reduced by decreasing the thickness of the blade at the blade tip. Denton (1993) found that if the blade thickness is more than four times the tip gap, the tip clearance flow will mix out over the blade tip, resulting in an increase in static pressure, thus increasing the pressure difference between the two sides of the blade. The flow through the blade tip clearance

is shown in Figure 2.10.

Incidence losses are losses caused by the variation in blade incidence angle. The blade incidence angle (i) is the angle between the relative flow and the blade setting angle, as shown in Figure A.6. A change in incidence angle (i) is thus either caused by a change in air inlet angle (β) or by a change in blade setting angle (γ). Variation of the air inlet angle, on the other hand, is caused by changes in either rotational speed of the blades or change in the axial velocity and thus the flow coefficient (φ). The incidence angle should not be mistaken for the angle of attack, which is the angle between the average relative flow of the incoming and outgoing flow vectors and the chord line.

As long as no flow separation occurs, the incidence losses can be regarded as Reynolds number independent (Hess, 2010). At an extreme angle to the blade, that is at a high incidence angle, flow separation is likely to occur. The flow separation causes the flow to follow a different geometry and results in an increase in drag and flow blockage. Apart from the incidence angle, the onset of separation is a function of Reynolds number and surface friction. Flow separation can occur at low- and high Reynolds number flow (Rhoden, 1952). These are laminar and turbulent flow separations, respectively. The occurrence of flow separation, as shown in Figure 2.11, is apparent by the large variation in air outlet angle for different Reynolds number flow at a high- and a negative incidence angle. A large air outlet angle indicates a large blade wake, which is the result of flow separation along the blade. An incidence angle, at which flow separation is likely too occur is typically avoided, for one, due to the close point of stall.

2.4 Review of common scaling formulas

Several scaling formulas have been developed over the years. The basis of these formulas are either empirical or theoretical. The scaling formulas are typically developed to solely scale the efficiency of a fan, although some formulas include the scaling of the full fan performance. The performance of axial fans is commonly characterized by the pressure, efficiency and shaft power in relation to the air flow rate (McPherson, 2009). These variables are typically converted into their non-dimensional form to allow for a better comparison between scaled results.

One of the most commonly used scaling equations are the affinity laws. Derived using dimensional analysis, the affinity laws, also called the fan laws, express a relation between the variables involved in fan performance. The affinity laws for volume flow rate ($\dot{V}$), fan static pressure rise (ΔP), fan power

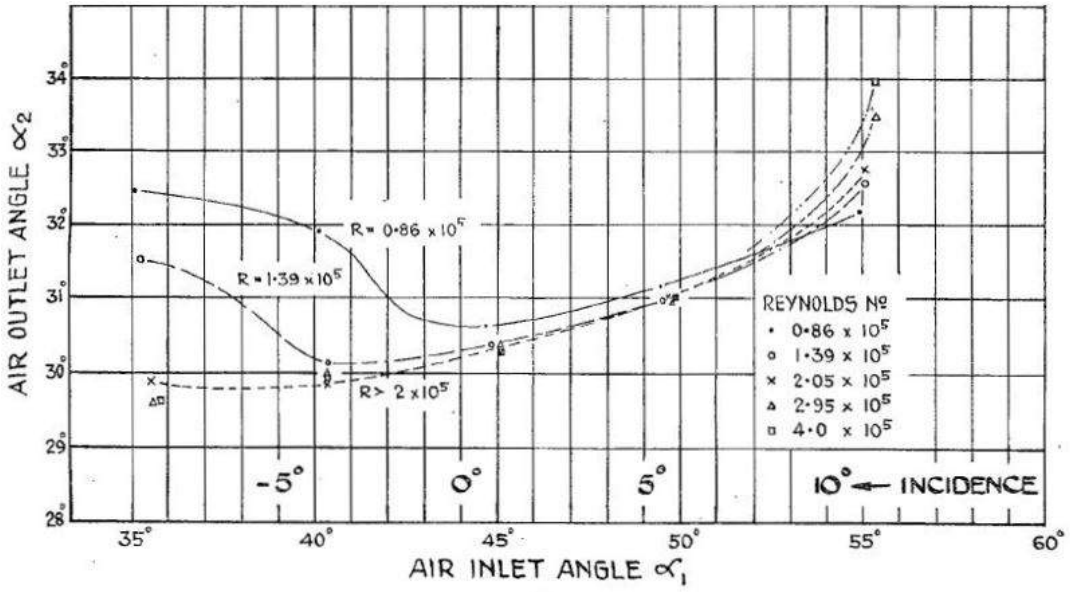

Figure 2.11: Effect of the Reynolds number on the air outlet angle (Rhoden, 1952)

(P) and fan static efficiency (η) are defined as follows:

$$\frac{\dot{V}_p}{\dot{V}_m} = \frac{N_p}{N_m}\left(\frac{d_{p_{fc}}}{d_{m_{fc}}}\right)^3 \tag{2.4}$$

$$\frac{\Delta P_{p_{sf}}}{\Delta P_{m_{sf}}} = \left(\frac{N_p}{N_m}\right)^2\left(\frac{d_{p_{fc}}}{d_{m_{fc}}}\right)^2\left(\frac{\rho_p}{\rho_m}\right) \tag{2.5}$$

$$\frac{P_p}{P_m} = \left(\frac{N_p}{N_m}\right)^3\left(\frac{d_{p_{fc}}}{d_{m_{fc}}}\right)^5\left(\frac{\rho_p}{\rho_m}\right) \tag{2.6}$$

$$\eta_{p_{sf}} = \eta_{m_{sf}} \tag{2.7}$$

In this study the physically larger fan is regarded as the prototype (subscript p) and the smaller fan regarded as the model (subscript m). The fan laws are based on the premise that both geometric- and kinematic similarity exist between the model and prototype fan. As shown in Equation 2.4-2.7, the affinity laws disregard any differences in Reynolds number and viscous effects between the model and the prototype. Therefore the use of the affinity laws alone can result in a discrepancy in predicted fan performance, especially if there is a considerable size or speed difference between the model and prototype.

Hutton (1954) and Hess (2010) studied various scaling formula. These scaling formulas can be divided into three main groups as stated by Hutton (1954).

1. Formulas with pipe friction based losses
2. Formulas dividing losses into frictional and kinetic components
3. Formulas with purely empirical based friction components

Some of the most common and noteworthy scaling formulas are:

Moody (1926):

$$\frac{1-\eta}{1-\eta_m} = \left(\frac{D}{D_m}\right)^{-0.25} \tag{2.8}$$

Staufer (1925):

$$\frac{1-\eta}{1-\eta_m} = \left(\frac{D}{D_m}\sqrt{\frac{H}{H_m}}\right)^{-0.25} = \left(\frac{D}{D_m}\sqrt{\frac{y}{y_m}}\right)^{-0.25} \tag{2.9}$$

Pfleiderer (1955):

$$\frac{1-\eta}{1-\eta_m} = \left(\frac{Re}{Re_m}\right)^{\alpha} \quad \text{where -0.25} < \alpha < -0.1 \tag{2.10}$$

Ackeret (1948):

$$\frac{1-\eta}{1-\eta_m} = V\left[1+\left(\frac{Re}{Re_m}\right)^{-0.2}\right] \quad \text{with V} = 0.5 \tag{2.11}$$

The scaling equation derived by Moody (1926) and Staufer (1925) is one of the first formula describing efficiency scaling. The formula is based on the assumption that the difference in losses between two scaled turbomachines is purely due to frictional effects. The frictional losses are based on an expression of pipe friction. (Hutton, 1954)

Pfleiderer (1955) was the first to treat friction losses in a physical manner, including the Reynolds number and thus making friction losses scalable. Pfleiderer based his method on the thought that inefficiency $(1-\eta)$ is proportional to the friction factor (c_f) and that the friction factor is proportional to the

negative power of Reynolds number ($c_f \sim Re^{-1}$). The exponent (α), given in Equation 2.10, is dependent on Reynolds number and thus cannot be treated as a constant. The problem with this method is that it is based on hydraulically smooth surfaces which can result in some inaccuracy. Another problem is the unrealistic result obtained when the Reynolds number tends to infinity, as the efficiency will tend to the value of one, i.e. 100% efficiency. Pfleiderer's scaling method is based on Reynolds number as shown in Equation 2.10, hence it does not take into account pure inertia losses, which are independent of the Reynolds number.

Ackeret was the first researcher to group the losses present in a fan into two groups: Inertia losses and Viscous losses. As stated by Mühlemann (1948), Ackeret improved Pfleiderer's method by including a loss factor (V) of 0.5, based on the assumption that half of the losses in the fan are inertia losses and thus independent of Reynolds number. The other half are viscous losses and thus depend on Reynolds number and are therefore scalable. The value of the loss factor (V) is based on the assumption of a hydraulically smooth surface. (Hess, 2010)

The Ackeret scaling formula often forms the basis of modern scaling formulas, such as the scaling method derived by Pelz and Hess (2010) and Pelz *et al.* (2012).

Scaling formula derived by Pelz and Hess (2010):

$$\frac{1-\eta}{1-\eta_m} = 1 + V\left[\frac{c_f}{c_{f,m}} - 1\right] \tag{2.12}$$

1st model (analytical):

$$V = 1 - \frac{\eta}{1-\eta}\frac{1}{\psi}\left[\psi_i\left(\varphi_{opt}\right) + \psi\left(\varphi_{opt}\right) - \psi\left(\varphi\right) - \varphi_0'\left(\varphi - \varphi_{opt}\right)\right] \tag{2.13}$$

2nd model (friction loss model):

$$V = b\frac{\eta}{1-\eta}\frac{\varphi^2+1}{\varphi}\lambda(Re, k/d) \tag{2.14}$$

Pelz and Hess (2010) investigated the importance of the loss factor (V) and published two methods that are based on the Ackeret formula. The formula is shown in Equation 2.12. The main difference between the two methods lies in the assessment of the loss factor (V). Hess (2010) states that the value of the loss factor (V) is susceptible to inertia losses, which depends on flow coefficient

and fan geometry.

The first method is an analytical method for which the loss factor (V) is determined analytically and thus does not require experimental performance measurements at different rotational speeds. The analytical assessment of the loss factor is given in Equation 2.13. This method does, however, not consider the shift of the peak efficiency point to a higher flow coefficient for an increase in Reynolds numbers Hess (2010).

The second method, as given in Equation 2.14, predicts the friction losses by using experimental data at varying Reynolds numbers to create a friction loss model. This method uses a geometry dependent factor (factor b), which is determined by experimental data. Thus a new set of experimental data is needed when a different fan model is analysed.

The analytical method provides a good prediction of the fan efficiency at a low flow rate but greatly under-predicts the efficiency at increased flow rate. The second method, using a friction loss model, slightly over-predicts the efficiency at low flow rates and under-predicts the efficiency at high flow rates (Pelz and Hess, 2010). The method performs well in the region close to the design point. Hess (2010) concludes that the results of both methods deviate from the experimental results but that the second method provides greater overall accuracy.

In 2012 Pelz *et al.* (2012) published a new scaling method, aiming to omit empirical functions in scaling in order to gain a universal, physical based scaling method. The scaling method is a modification of the scaling formula derived by Pelz and Hess (2010) and is based on the assumption that inertia losses in the model are the same as in the full-scale prototype. The method consists of two parts: the scaling of the efficiency and the scaling of the flow coefficient. The change in efficiency ($\Delta\eta$) is first determined, after which the flow coefficient at which the efficiency lies is calculated.

$$\epsilon := 1 - \eta = \frac{c_d}{\lambda} \tag{2.15}$$

$$\frac{d\epsilon}{\epsilon} = \frac{dc_d}{c_d} - \frac{d\lambda}{\lambda} \tag{2.16}$$

where:

c_d is the drag coefficient

$\lambda = 2w_{shaft}/U_c^2$ is the power coefficient with w_{shaft} being the specific work done by the shaft (Pelz and Stonjek, 2013).

The scaling method is based on the derivative of the inefficiency, shown in Equation 2.15 and 2.16.

The drag coefficient (c_d) in an incompressible case consists of inertia drag (c_i)and surface friction (c_f). Since the method is based on the assumption that inertia losses in the model are identical to the inertia losses in the prototype, the drag coefficient is set to be equal to surface friction i.e. $c_d = c_f$. The power coefficient (λ) is decomposed into the power transferred to the fluid by the fan, power lost due to flow leakage and power lost due to fluid drag.

The resultant scaling formula derived by Pelz *et al.* (2012) is the following:

$$d\eta = -(1 - \eta_m)\left[\frac{\Delta c_f}{c_{f,m}} + \Theta\frac{\Delta t}{\epsilon\lambda}\right] \tag{2.17}$$

with:

$$\Theta = \begin{cases} \lambda^2 & \text{unshrouded machine} \\ [4\mu d_s \psi^{\frac{3}{2}}]/\varphi & \text{shrouded machine} \end{cases} \tag{2.18}$$

The advantage of the efficiency scaling formula by Pelz *et al.* (2012) is that the formula includes Reynolds number and roughness effects in the first term and the effect of tip clearance differences between the model and prototype in the second term.

The second part of the scaling method developed by Pelz *et al.* (2012) is the scaling of the flow coefficient i.e. the shift in peak efficiency point. The shift to a higher flow coefficient for a increased Reynolds number was discussed in Section 2.2.

$$\Delta\varphi = -\frac{1}{C\left(s_b, \zeta_o\right)}\Delta c_f \tag{2.19}$$

The change in flow coefficient due to scaling is given by Equation 2.19, which was derived by Pelz and Stonjek (2013). The constant C is a function of the dimensionless blade spacing ($s_b = S_b/ch$) and blade stagger angle and is calculated as follows:

$$C\left(s_b, \zeta_o\right) = \frac{s_b}{2}\left(sin\ \zeta_o + cos\ \zeta_o\right) \tag{2.20}$$

Pelz and Stonjek (2013) states that Equation 2.20 was derived without including the pressure gradient of the fan. The constant is thus overestimated.

Experimental tests showed that a constant value of $C = 0.25$ gave more accurate results (Pelz and Stonjek, 2013).

Since the change in efficiency is proportional to the change in flow coefficient ($\Delta\eta \propto \Delta\varphi$), Equation 2.19 can be rewritten as:

$$\frac{\Delta\eta}{\Delta\varphi} = C\left(s_b, \zeta_o\right) \frac{1 - \eta_m}{c_{f.m}} \tag{2.21}$$

Hess (2010) identified two fundamental problems that most common scaling formulae have. The first problem being that in most of the methods the efficiency could increase up to 100 % and that secondly all methods assume complete geometric similarity. This is often not achievable for parameters such as surface roughness and tip clearance. A fan with 3 mm tip clearance, for example, requires the 10 times smaller model to have a tip clearance of 0.3 mm. Therefore scaling tip clearance and surface roughness can be too costly and difficult to machine.

Chapter 3

Reference results

In this chapter the experimental tests, caried out by Conradie (2010) and Louw (2015), are discussed. The experimental results will be used to assess the accuracy of the numerical modelling. The scaling formula derived by Pelz *et al.* (2012) is also discussed and tested. The predicted fan performance by the scaling formula is compared to the experimental results.

3.1 Definition of performance parameters

In this section the variables used to acquire a measure of performance of the fans are presented. Due to the different scale and Reynolds number of the analysed fans, some of the variables have to be converted into dimensionless form to allow comparison. The fan performance is analysed by referring to values of fan static pressure, -efficiency and fan power.

The change in fan static pressure (ΔP_{fs}) is, as defined by the BS 848-1:2007 standard, the difference between the outlet static pressure and the inlet total pressure. Figure 3.1 shows a BS 848 Type A fan test facility as used by Louw (2015) to access the performance of the 1.542 m B2a-fan. The inlet total pressure is measured in the settling chamber, upstream of the fan, denoted as $\Delta P_{s,plen}$ in Figure 3.1.

The **fan static pressure coefficient** is calculated as follows:

$$\Psi_{fs} = \frac{\Delta P_{fs}}{0.5\rho U_{c,tip}^2} \tag{3.1}$$

The **fan static efficiency** is calculated using the following equation:

$$\eta_{fs} = \frac{\Delta P_{fs}\,\dot{V}}{P} \quad [\%] \tag{3.2}$$

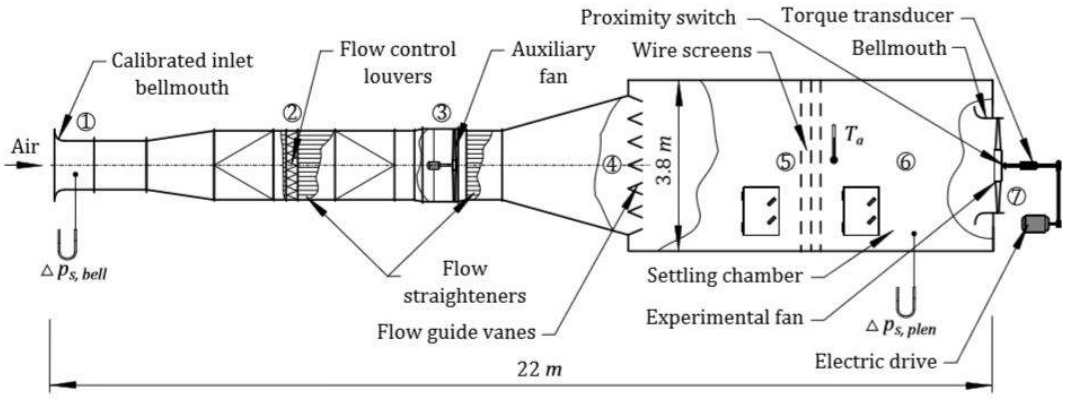

Figure 3.1: Type A fan test facility (Louw, 2015)

The **fan power** is calculated using the following equation:

$$P = T\omega \quad [\text{N·m}] \tag{3.3}$$

The **power coefficient** is calculated using the following equation:

$$\Gamma = \frac{P}{\dot{m}_{design}\, U_{c,tip}^2/2} \tag{3.4}$$

The **flow coefficient** at the blade tip is calculated as follows:

$$\varphi = \frac{U_a}{U_{c,tip}} \tag{3.5}$$

$$U_a = \frac{\dot{V}}{A_F} \quad [\text{m/s}] \tag{3.6}$$

where $\dot{V}$ is the volumetric flow rate and A_F is the fan annulus area.

$$U_{c,tip} = \frac{2\pi}{60} Nr = \omega r \quad [\text{m/s}] \tag{3.7}$$

The Reynolds number, as specified in Equation 2.1, makes use of the blade's chord length as the characteristic length. A number of publications, such as Stonjek and Pelz (2014), Hess (2010) and BS 848-1:2007 standard use a diameter based Reynolds number, since the research often focusses on axial flow fans situated in circular ducts. The chord-based Reynolds number, combined with the blade rotational speed, is used for this research, because ACC cooling fans do not have a ducted installation. The chord-based Reynolds number was

also used by Conradie (2010) and Louw (2015) for the experimental testing of the 0.63 m and the 1.542 m B2a-fan.

3.2 Experimental analysis

The B2a-fan is an eight bladed axial flow fan, with a hub-tip ratio of 0.4. The NASA LS 0413 airfoil is used in the design of the B2a-fan blades. The blades are set at a stagger angle of 59° at the hub as specified by Louw (2015). Figure 3.2 shows a schematic of a 0.63 m diameter B2a-fan. More detailed specifications of the B2a-fan are provided in Appendix A.

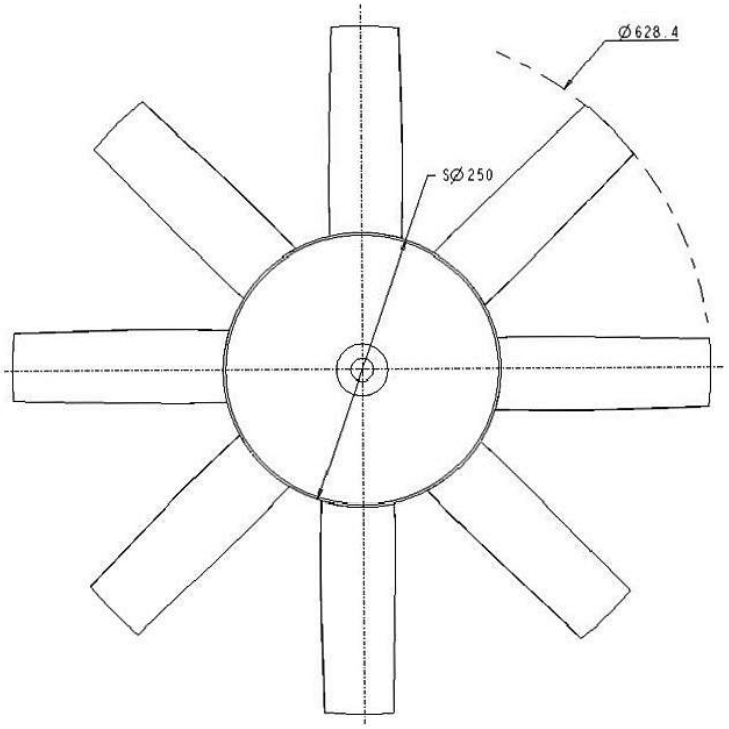

Figure 3.2: Schematic of the B2a-fan (Conradie, 2010)

Experimental testing of a 0.63 m and 1.542 m diameter B2a-fan was conducted by Conradie (2010) and Louw (2015) respectively in a fan test facility at the University of Stellenbosch. The experimental tests were conducted in accordance with the BS 848-1:2007 standard. Conradie (2010) conducted the tests of a 0.63 m B2a-fan in a type B fan test facility, which has a free inlet and a ducted outlet configuration, while the experimental analysis of a 1.542 m B2a-fan, conducted by Louw (2015), was performed in a type A fan test facility, which has a free inlet and outlet configuration. The ducted outlet of the type B setup restricts radial flow and causes additional losses due to pipe friction. The difference in results due to the different fan test facilities are

expected to be small since Conradie (2010) used, as required by the BS 848-1:2007 standard, correction factors for the additional friction losses occurring in the ducted outlet. At a low flow rate the difference in results are expected to increase since the radial flow increases. A comparison of the numerical results for a ducted and type A domain verified the prediction. Details of the numerical model will be discussed in Chapter 4.

The fan static pressure and fan static efficiency plotted against flow coefficient for the experimental results of the 0.63 m and 1.542 m B2a-fan are shown in Figure 3.3 & 3.4. The study by Conradie (2010) put a greater emphasises on the low flow rate conditions. As a result the experimental test of the 0.63 m fan was conducted only up to a flow coefficient of $\varphi = 0.168$. The comparison shows that the fan static pressure correlates well for the two fans at low flow rate, but deviates as the flow rate is increased, such that the fan static pressure of the 0.63 m fan is higher than the fan static pressure of the 1.542 m fan. Since the dimensionless form of the fan static pressure is used, the 0.63 m and the 1.542 m diameter fans should have an equal fan static pressure coefficient.

A contributing factor to the higher fan static pressure of the 0.63 m fan is its proportionally lower tip clearance. The 0.63 m diameter B2a-fan model used by Conradie (2010) has a tip clearance of 0.8 mm or: $t/d = 0.0008/0.63 = 0.127\%$. The 1.542 m model used by Louw (2015) has a tip clearance of 3 mm or 0.2%. The lower tip clearance results in a slightly higher fan static pressure and -efficiency, due to lower tip clearance losses. The difference in tip clearance is expected to be small, such that the effect is minimal. A numerical analysis of the 0.63 m fan with the two different tip clearances is conducted, to determine the difference in fan performance, as discussed in Section 5.2.2.

The difference in fan static efficiency occurs due to the size and Reynolds number difference between the 0.63 m and the 1.542 m B2a-fans, as well as by the difference in tip clearance between the two fans. Therefore a shift in efficiency is expected.

3.3 Analysis of scaling formulas

The scaling formulas were introduced and discussed in Section 2.4. The newest scaling formula is the formula developed by Pelz *et al.* (2012). Pelz suggests that the efficiency is proportional to the flow coefficient ($\Delta\eta \propto \Delta\varphi$). As a result both the efficiency and the flow coefficient are scaled using Equation 2.17 - 2.21.

The flow is assumed to be turbulent, therefore the turbulent smooth and -rough surface friction factor (c_f) is used, as given in Equation 3.8 & 3.9:

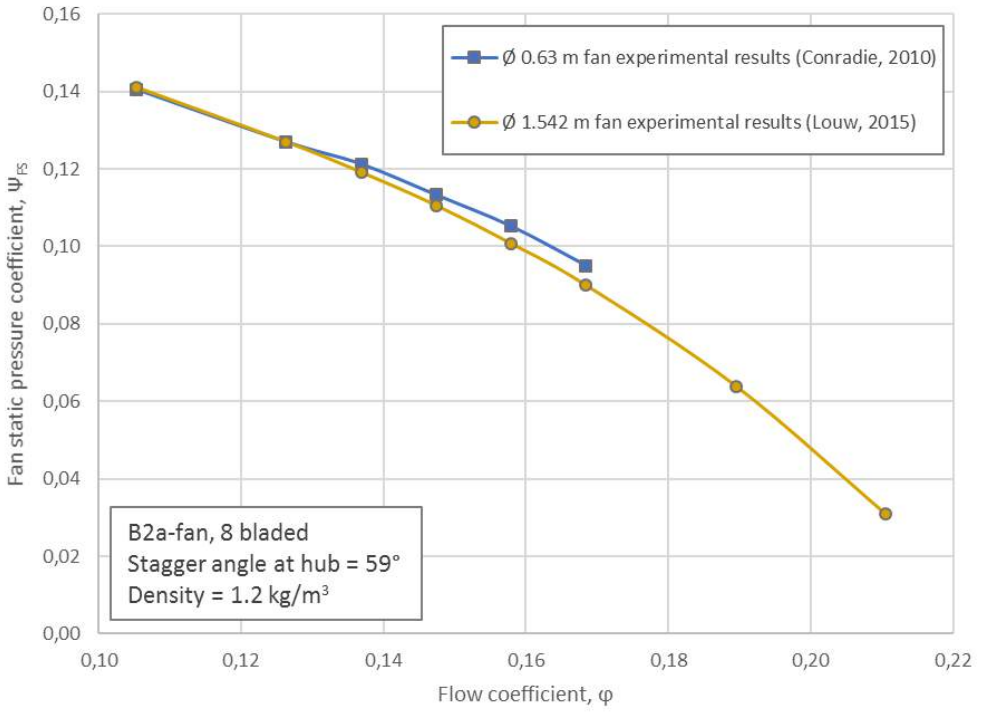

Figure 3.3: Fan static pressure coefficient of the 0.63 m and 1.542 m B2a-fan experimental results

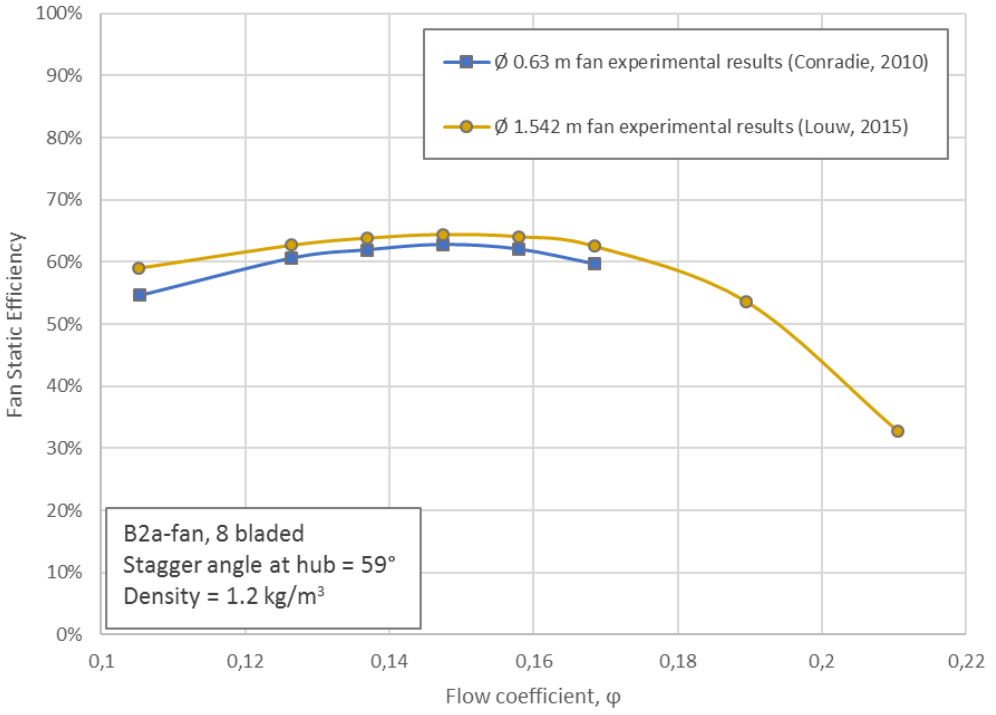

Figure 3.4: Fan static efficiency of the 0.63 m and 1.542 m B2a-fan experimental results

$$c_{f,smooth} = 0.455\ (log_{10}Re)^{-2.58} \tag{3.8}$$

$$c_{f,rough} = (1.89 - 1.62\ log_{10}\frac{\varepsilon}{L})^{-2.5} \tag{3.9}$$

The blade skin is made from a fibre-reinforced polymer which has, according to Teicher *et al.* (2017) a surface roughness between 0.00294 and 0.00123 mm. A surface roughness of 0.00171 mm was chosen. As stated earlier the 0.63 m diameter B2a-fan used in the experimental tests has a relative tip clearance of 0.127 %, while the relative tip clearance of the 1.542 m fan is 0.2 %. The difference in tip clearance Δt, found in Equation 2.17, is defined as the change in relative tip clearance from the model to the full scale machine. Therefore Δt = 0.073 for the case of scaling up and Δt = -0.073 for the case of scaling down. The B2a-fan is classified as an unshrouded machine since there is no tip seal or groove at the blade tip (Pelz and Stonjek, 2013). The results of the scaled-up B2a-fan, using the Pelz scaling method, are shown in Figure 3.5. The experimental data of the 0.63 m fan is used to predict the fan static efficiency of the 1.542 m fan and vice versa.

The results of the Pelz scaling formula, as shown in Figure 3.5, show a over-prediction of the scaled results in comparison to the experimental results. A small difference between the scaled- and experimental results is seen at a low flow coefficient. The difference however increases with an increase in flow coefficient.

Figure 3.6 shows the results of the down-scaled B2a-fan using the Pelz scaling formula. The experimental data of the 1.542 m fan is used to predict the fan static efficiency of the 0.63 m fan. The results show an under-prediction of the fan static efficiency as calculated using the Pelz scaling formula in comparison to the experimental results of the 0.63 m fan. The scaling formula assuming turbulent rough flow over the blade predicts slightly higher efficiency than the turbulent smooth flow assumption. As visible from Figure 3.5 and 3.6 the scaling method derived by Pelz *et al.* (2012) over-predicts the change in efficiency ($\Delta\eta$), such that the predicted fan static efficiency is higher than the experimental results of fan static efficiency for the case of scaling up and lower for the case of scaling down.

A numerical analysis is subsequently conducted to investigate the agreement between the numerical- and the experimental results of the B2a-fan. A comparison between the predicted results, using the Pelz scaling formula, and the numerical results is conducted thereafter. The comparison is shown in Appendix A.2.

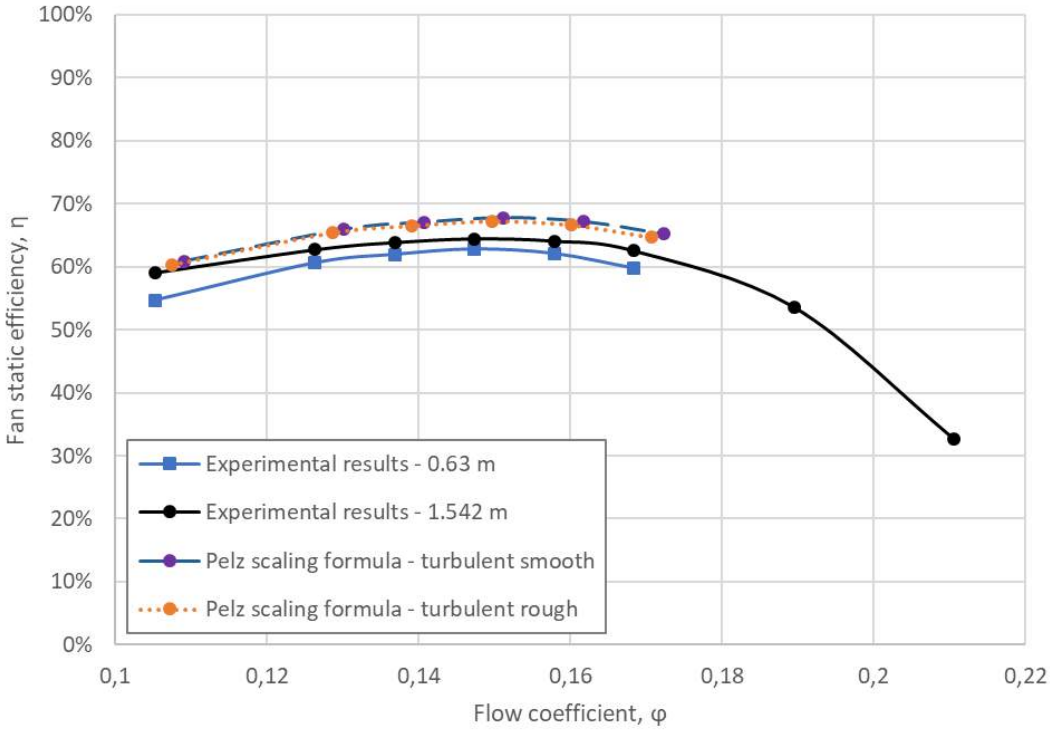

Figure 3.5: Up-scale performance prediction by the Pelz scaling formula of the 1.542 m B2a-fan based on experimental data of the 0.63 m fan

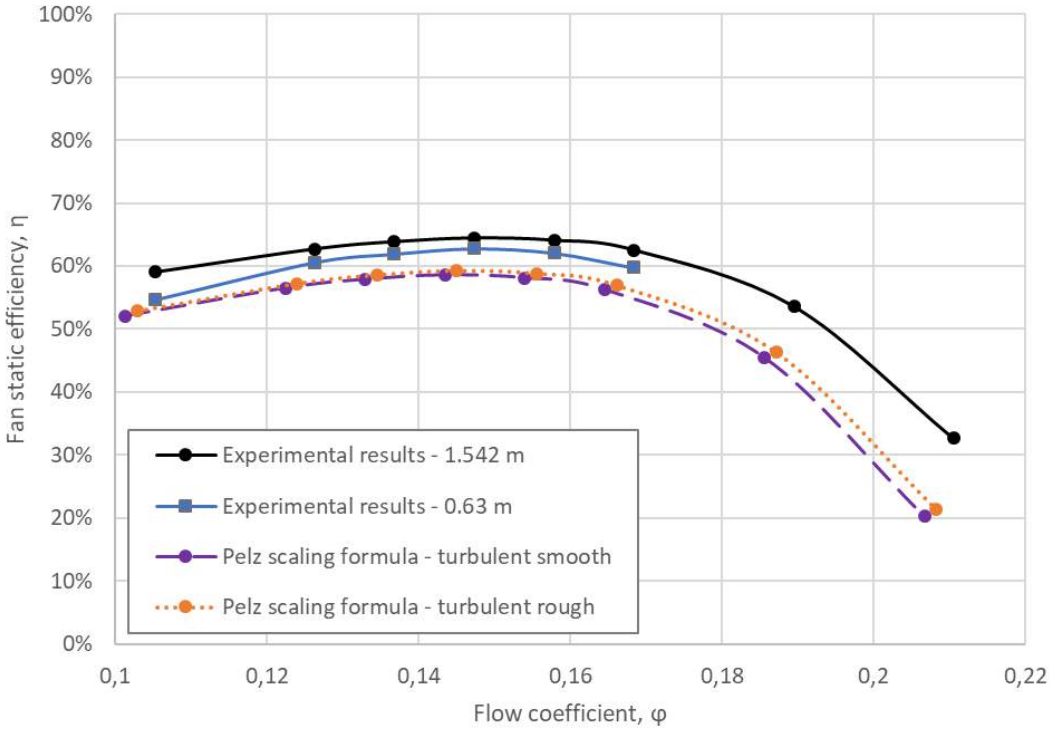

Figure 3.6: Down-scale performance prediction by the Pelz scaling formula of the 0.63 m B2a-fan based on experimental data of the 1.542 m fan

Chapter 4

Numerical modelling

Numerical analysis of the scaling effects of axial fans is considered to be inexpensive compared to experimental analysis, as apart from multiple fans of different sizes, a fan test facility is needed that is able to accommodate and accurately assess a wide range of fan sizes. All of the domain models, meshes and simulation setups are performed using *ANSYS 17.0*. All the programs that are mentioned are part of the *ANSYS Workbench 17.0* software package.

4.1 Computational domain

The computational domain is constructed as a wedge with periodic sides representing $1/8^{th}$ of the full three-dimensional flow domain. As a result only one out of the eight blades of the B2a-fan is modelled. The computational domain is termed the periodic three-dimensional model (P3DM).

The P3DM is built on the assumption that the flow is rotationally periodic, meaning that the rotational flow entering the computational domain through the periodic plane is identical to the flow exiting the domain through the opposite periodic plane. Near or at rotational stall, occurring at low flow rate, the flow pattern is no longer rotationally periodic, thus the P3DM model can no longer be used (Louw, 2015). The flow rates used in the present thesis are sufficiently high to validate the periodic flow assumption.

The P3DM simplifies the numerical simulation greatly, as only a single blade in a periodic, 45° wedge is modelled, compared to a full 3D simulation of the fan. This results in a significantly reduced model size, leading to a reduction in memory and computational time (Louw, 2015).

The numerical analysis is carried out using two different configurations:

1. Ducted domain
2. Type A fan test domain

The analysis is initiated by modelling the axial fan in a ducted domain. In the ducted setup the inlet- and outlet sub-domains are modelled as long annular sections, extending in the axial direction, as shown in Figure 4.1. The inlet- and outlet sub-domain thus form an equal-sized extension of the blade passage domain. Figure 4.1 shows a side and a front view of the configuration. Note that the entire fan and the full domain is shown. In the actual numerical analysis a 45° wedge with a single blade, as indicated in blue, is modelled. The boundary conditions of the top and bottom annulus wall of the inlet and outlet sub-domain are set equivalent to the boundary conditions of the shroud and hub of the fan.

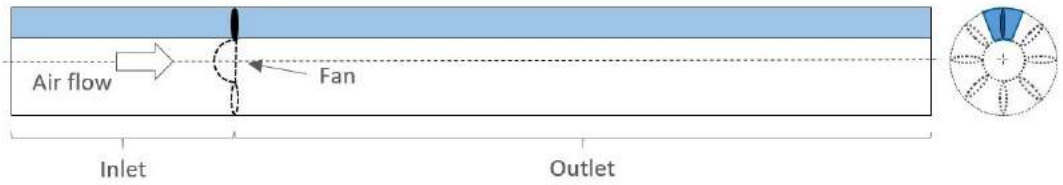

Figure 4.1: Configuration 1: ducted domain

The numerical analysis was first performed without a tip clearance, to create a low complexity numerical model. The ducted domain with no tip clearance allows the creation of a relative simple mesh, resulting in a relative short computational time. This simplification of the numerical model enables setup issues and uncertainties to be resolved and establishes a foundation for more complex simulations. After the appropriate settings were finalized and satisfactory results obtained, a 3 mm tip clearance was included in the numerical analysis of the 1.542 m diameter B2a-fan.

Once the numerical analysis of the ducted B2a-fan, with a 3 mm blade tip clearance, showed good correlation with the results obtained by Louw (2015), a more complex configuration was created. In the second configuration, the inlet- and outlet sub-domains were modelled to represent the shape and size of the BS 848 type A fan test facility, as shown in Figure 4.2. In this configuration the ball-nose hub and bell mouth shroud are included. Figure 4.2 shows a side and a front view of the domain. The entire fan and the full domain is shown. In the actual numerical analysis a 45° wedge, shown in blue, with a single blade is modelled.

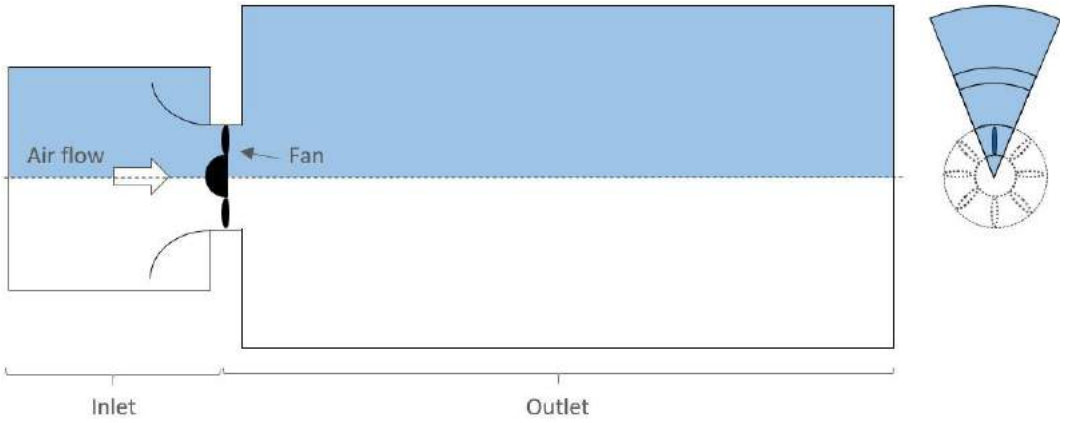

Figure 4.2: Configuration 2: simplified windtunnel domain

A numerical analysis of three different fan sizes is conducted. A 0.63 m, 1.542 m and a 9 m diameter B2a-fan are modelled. Detail of the scaling of the fans is discussed in section 4.5.

4.2 Inlet & Outlet domain and mesh creation

The inlet- and outlet sub-domains are created using *ANSYS Design Modeller*. The dimensions of the inlet- and outlet sub-domain was determined through a sensitivity study done as part of a PhD study by Louw (2015).

After the creation of the domain, *ANSYS Mesher* is used to generate the mesh. In ANSYS Mesher a tetrahedral mesh with prismatic inflation layers near wall surfaces is created. The tetrahedral mesh is converted to a polyhedral mesh in *Fluent*. An unstructured polyhedral mesh is used in the inlet- and outlet sub-domains, as the polyhedral mesh uses less time and iterations to reach convergence, compared to a tetrahedral mesh (Symscape, 2013).

Inflation layers, using prism cells, are created on solid surfaces, such as the shroud, hub, blade, as well as the entrance and exit face to the blade passage. Figure 4.3 shows the polyhedral cells with an inflation layer on the hub. The inflation layer is adjusted for different flow conditions to keep the y+ value in the range required by the selected turbulence model.

In the second configuration (type A fan test domain) a multi-zone approach is used. This means that the domain is split into several zones or regions. The inlet- and outlet sub-domains of the second configuration are each split into three zones, as seen in Figure 4.4, with each zone having a different mesh density. The mesh density is decreased the further away the zone is from the blade. The zone immediately upstream of the fan inlet and the zone immedi-

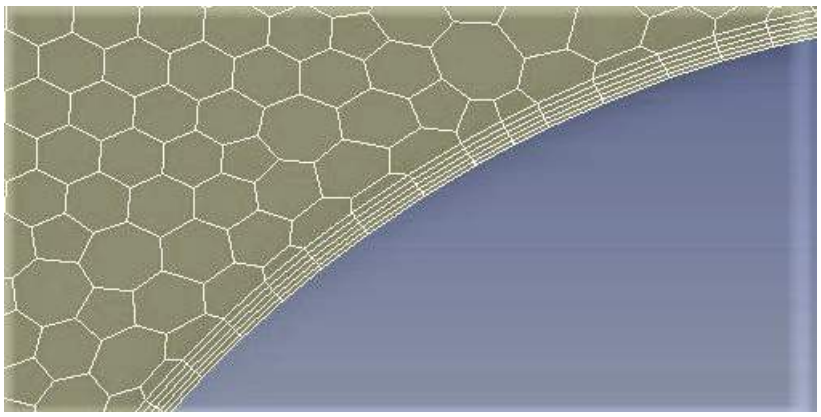

Figure 4.3: Polyhedral mesh with inflation layer along the hub

ately downstream of the fan is meshed with a structured array of hexahedral cells that create a high density mesh with cells aligned with the direction of the flow, which reduces the potential numerical error. Interfaces are created to connect the zones with each other.

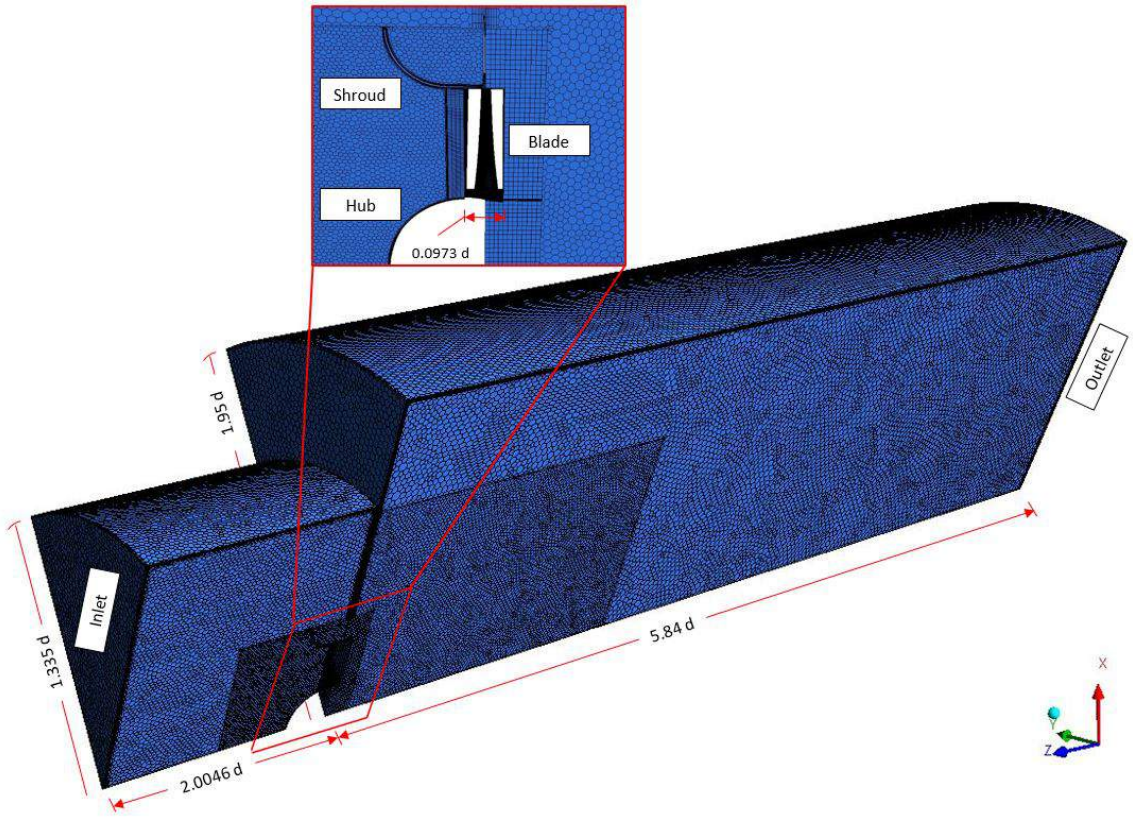

Figure 4.4: Side view of the meshed computational domain in a P3DM configuration

An analysis of the mesh dependency of the sub-domain is provided in Appendix C.

4.3 Blade domain and mesh creation

Contrary to the inlet- and outlet sub-domains, the domain around the fan blade and the subsequent meshing of the domain is done using *ANSYS Turbogrid*. *Turbogrid* is specifically tailored for domain and mesh creation for turbomachinery. The domain created around the blade, as show in Figure 4.5, is referred to as the blade passage domain.

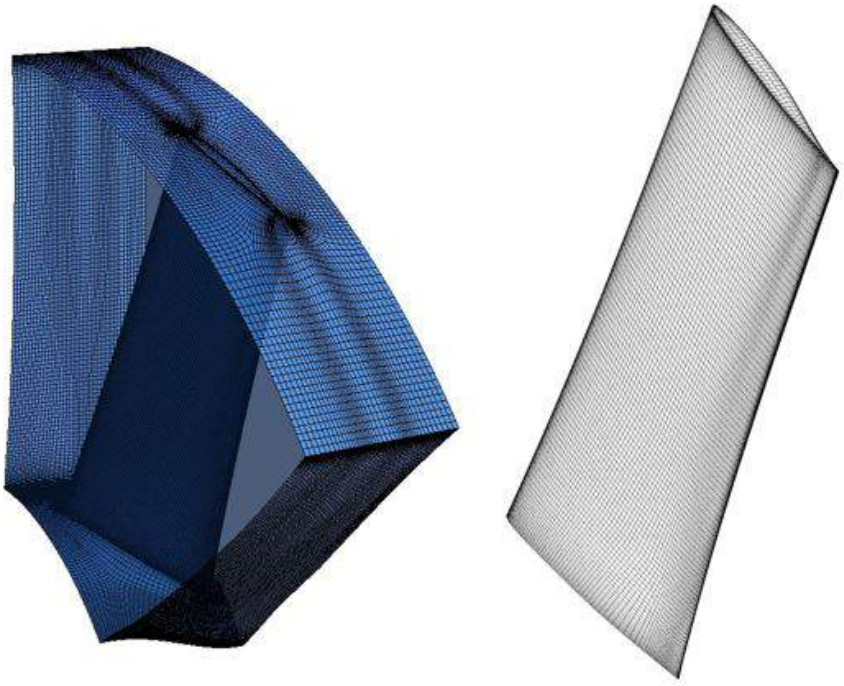

Figure 4.5: TurboGrid domain and blade mesh

A structured, flow aligned hexahedral mesh, with the cell height and inflation set to provide a y+ value in the range required by the turbulence model, is created. The number of cells required to provide a mesh independent solution is determined in a mesh dependency study of the passage domain, as shown in Appendix C. Like the inlet- and outlet sub-domains, the mesh around the blade had to be adjusted for different flow conditions and fan sizes in order to keep the y+ value and mesh quality of the mesh in the required range. The mesh created on the blade surface is shown in Figure 4.5.

An initial analysis was conducted without a blade tip clearance. After satisfactory results were obtained a 3 mm tip clearance was included on the 1.542 m diameter fan. This equates to a percentage tip clearance of $s/d = 0.2\%$. A 12 layer mesh, adhering to the desired y+ range, was created in the region between the blade tip and the shroud.

Appendix C provides a detailed report on the mesh dependency of the blade passage domain created in TurboGrid.

4.4 Domain assembly and Interface creation

The meshed inlet-, blade passage- and outlet sub-domain are each imported into *Fluent*. A tangential offset between the blade passage sub-domain and the inlet- and outlet sub-domain exists, as shown in Figure 4.6, due to the skew trapezoid like sub-domain created by TurboGrid. This offset is inevitable since *TurboGrid* automatically creates the domain shape around the blade, based on the blade profile, flow conditions and the set mesh. As a result a rotational non-conformal interface arises. Since the domain faces and mesh elements of the sub-domains do not align and only part of the two domain faces are in contact with each other, a periodic repeat mesh interface is required to fully combine the off-setted inlet- and outlet sub-domains with the blade passage domain. The periodic repeat interface takes into account the repeating nature of the flow and thus translates or rotates the fluxes by a periodic offset (ANSYS Fluent Inc., 2017).

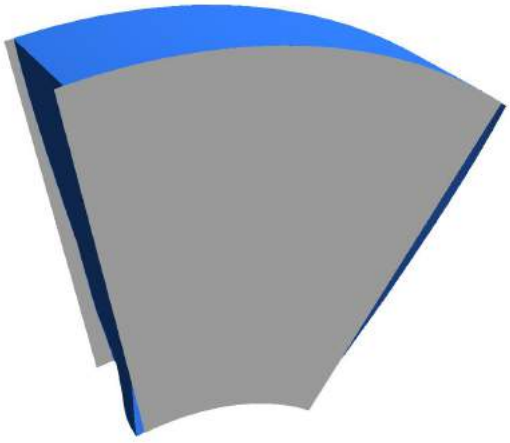

Figure 4.6: The tangential offset of the sub-domain interfaces

A periodic boundary condition interface was created between each side of the inlet-, blade passage and outlet sub-domain to create rotational periodicity between each side of the wedge shape domain. The periodic boundary

condition interface determines the flow conditions at the trailing periodic side by using the flow conditions at the leading periodic side. This is based on the rotational periodic assumption which implies that there is no flow gradient between the two faces in the circumferential direction. Matched interfaces are set for the additional interfaces needed in the Type A fan test domain configuration to connect the three zones that make up the inlet- and outlet sub-domain.

4.5 Fan scaling

A numerical analysis is conducted of three different sizes of the B2a-fan. The initial simulation of the fan is conducted using the 1.542 m diameter B2a-fan model created by Louw (2015). Following the simulation of the 1.542 m fan a 9 m and a 0.63 m fan model were created and analysed.

The entire domain of the 1.542 m simulation model is scaled using the scale function in *ANSYS Fluent* to create a 0.63 m and 9 m diameter fan model. A scaling factor of 0.40856 and 5.8366 is used for the scaling of the 0.63 m and the 9 m diameter fan respectively. The factor is determined by dividing the diameter of the fan model (0.63 m or 9 m) by the diameter of the prototype (1.542 m in this case).

New inlet-, outlet- and fan passage sub-domains are created for both the 0.63 m and the 9 m fan with adjusted inflation layers along the hub, shroud and blade, in order to keep the y+ value in the range desired by the turbulence model. The scaling function in *Fluent* not only scales the size of the domain but also scales the mesh. Down-scaling of the original 1.542 m domain reduces the size of the mesh elements, which reduces the y+ value of the mesh. Thus, the first layer thickness of the inflation layer has to be increased. The opposite is true when up-scaling the domain and mesh.

When simulating the different sized fans, the rotational speed is set to obtain equal tip speed to the prototype. Due to the size difference the rotational speed will thus be higher for fan models with a smaller diameter and lower for larger model fans. The equal tip speed results in an equal Mach number at a particular span fraction of the fan model and prototype. The equal tip speed also implies that at a particular span fraction of the fan blade, the ratio of the Reynolds number of the model to the Reynolds number of the prototype equals the geometric scaling factor.

The tip speed of the 0.63 m and the 9 m fan are set equal to the tip speed of the 1.542 m fan, resulting in the following rotational speeds:

Rotational speed of the 0.63 m fan:

$$\begin{aligned} (\omega r)_p &= (\omega r)_m \\ 78.54\left(\frac{1.542}{2}\right) &= \omega_m\left(\frac{0.63}{2}\right) \\ \Rightarrow \omega_m &= 192.236 \text{ [rad/s]} \end{aligned} \tag{4.1}$$

Rotational speed of the 9 m fan:

$$\begin{aligned} (\omega r)_p &= (\omega r)_m \\ 78.54\left(\frac{1.542}{2}\right) &= \omega_m\left(\frac{9}{2}\right) \\ \Rightarrow \omega_m &= 13.45652 \text{ [rad/s]} \end{aligned} \tag{4.2}$$

To calculate the mass flow inlet for the 0.63 m and the 9 m fan, the volume flow rate is scaled by using the affinity laws as given in Equation 2.4. A sample calculation of the mass flow inlet for the 0.63 m and the 9 m fan at different volume flow rates is given in Appendix B.

Matching the tip speed of the fans means that the Reynolds number across the blade will differ for a different size of fan. The Reynolds number range, calculated by using Equation 2.1, between the hub and the blade tip of the 0.63 m, 1.542 m and the 9 m B2a-fan is given in Table 4.1. The detailed calculation is given in Appendix B.

Table 4.1: Reynolds number range of the different sizes of B2a-fans

0.63 m		1.542 m		9 m	
Hub	Shroud	Hub	Shroud	Hub	Shroud
1.20e+05	2.49e+05	2.93e+05	6.09e+05	17.10e+05	35.56e+05

4.6 Rotational modelling

The rotation of the domain or parts of the domain is linked to the motion of a reference frame. Two types of rotating reference frames exist:

- Single Frame of Reference (SFR)
- Multiple Frame of Reference (MFR)

The Single Frame of Reference option is used for simulations in which all sub-domains and zones rotate at the same constant speed around the same rotational axis. Walls that are rotating in the same direction and speed around the same axis as the domain can assume any shape. Walls, such as the fan shroud, that are stationary relative to the stationary reference frame, must be surfaces of revolution about the rotational axis (ANSYS Fluent Inc., 2017).

Multiple Frames of Reference are used when individual zones rotate at different speeds and/or rotate around different axes. Each of the zones is then solved separately. A frame transformation is performed at the interface to the next zone. Multiple Frames of Reference are also used when an object or surface is stationary relative to the stationary axis, such as the fan shroud, but is not a surface of revolution around the rotational axis. (ANSYS Fluent Inc., 2017)

Various modeling approaches, as listed by ANSYS Fluent Inc. (2009), exist that can be used to conduct Single- or Multiple Frames of Reference simulations of rotating machinery, such as axial fans. These modelling approaches are called Frame Change Models. The following steady state Frame Change Models exist:

- Frozen rotor model
- Mixing-plane model

Both of these modelling approaches require a three dimensional model and use a multi-zone approach. The Frozen rotor model and Mixing-plane model both assume that the flow field is in a steady-state. The main difference between the two models is the way they treat the interfaces between the sub-domains and between the zones. (Augustyn, 2013).

The Frozen rotor model, also called the Moving Reference Frame (MRF) model, is the simplest and the least computational expensive of the two listed approaches. The Frozen rotor model makes the assumption that the flow between two zones is completely mixed and that the velocity over the interface is therefore constant. Thus the only alteration that is performed is a frame transformation at the interface. The frozen rotor model regards two zones divided by an interface to be directly connected with each other. The rotational interaction between two domains or zones is not accounted for. As a result the stationary domain or reference frame "sees" the rotating component at a stationary position. The frozen rotor model is thus analogous to freezing the rotating domain at a certain position and obtaining flow results from that instant with the fan blade in that position. (ANSYS Fluent Inc., 2017)

Due to the mixed-out flow assumption at the interface, the Frozen rotor model is not applicable in cases, such as low Reynolds number flow, in which the fluid flow did not reach a state of constant velocity over the interface. The same applies when a strong interaction between moving and stationary components or surfaces exist. In such cases the Mixing-plane model is applicable. Flow data is circumferentially averaged on both sides of the adjacent zone interface. The circumferential averaging is performed at several radial positions to create profiles of the flow properties. These profiles are then used to update the flow and the boundary conditions in both zones. Mass- or area weighted averaging can be implemented at the interface. The mixing at the interface removes the unsteadiness that would arise due to the non-uniform flow field and the subsequent circumferential variation in flow properties. This results in a steady-state solution. The Mixing-plane model requires specific boundary conditions to be set upstream and downstream of the interface. The upstream and downstream boundary interfaces are coupled by the Mixing-plane model. This is called a Mixing-plane pair (ANSYS Fluent Inc., 2017).

Initial simulations of the B2a-fan were done using a Multiple Frame of Reference. The blade passage was set to rotate around the positive z-axis, while the inlet- and outlet sub-domains were set as stationary. Both the Frozen rotor and the Mixing plane model were applied but both models showed large deviations from the experimental results. Since the Mixing plane model uses circumferential averaging at the interface, a slight mass imbalance resulted between the inlet and outlet of the domain. Enforcing mass flow conservation across the interface, results in a jump in total pressure across the mixing plane, as stated in ANSYS Fluent Inc. (2017).

It was found that using a Single Frame of Reference provides more accurate results. In this configuration all three sub-domains are rotated at the same rotational speed around the positive z-axis. The rotation of the sub-domains is set equal to the rotational speed of the fan.

4.7 Boundary conditions

In the numerical analyses conducted in this thesis a standard air density and viscosity of 1.2 kg/m^3 and 1.825(10)$^{-5}$ kg/m.s respectively is used in the fluid flow simulation. The following boundary conditions are used in the domain shown in Figure 4.7.

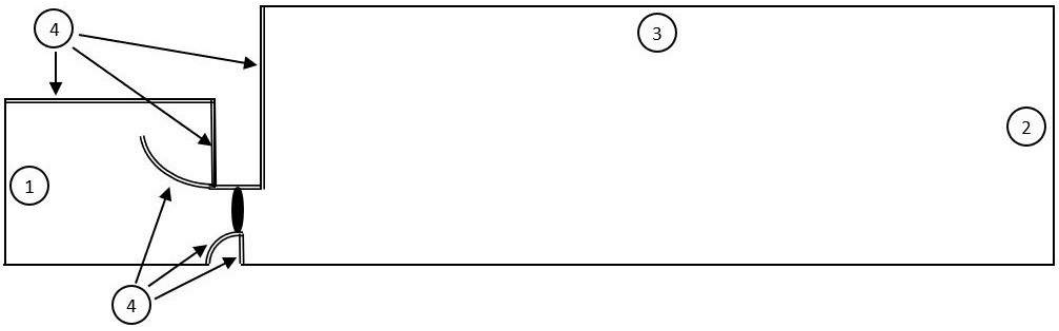

Figure 4.7: Domain outline with boundary conditions

Mass flow inlet (1)

The boundary condition of the domain's inlet face (No. 1 in Figure 4.7) is set as a mass flow inlet. A mass flow inlet boundary condition provides a prescribed mass flow rate or mass flux at the inlet face. The mass flow rate is obtained by multiplying the desired volume flow rate by the density of air ($\rho = 1.2$ kg/m^3) and then dividing by 8, as the domain represents only $1/8^{th}$ of the total fan domain. The mass flow inlet boundary allows the total pressure to vary across the boundary in response to the interior solution. Due to the incompressible flow problem and thus constant air density in the domain, both a mass flow- or a velocity inlet boundary condition can be used as the inlet boundary condition. The disadvantage of the velocity inlet boundary condition is, however, that the resultant solution is more sensitive to placement away from a solid obstruction compared to the solution determined using a mass flow rate boundary condition. Placing the inlet boundary too close to the fan blade can cause the flow properties to become highly non-uniform, resulting in the variation of flow properties with position and time. (ANSYS Fluent Inc., 2017)

To determine the fan's performance, so called fan curves need to be created. These are curves of fan static pressure and -efficiency against volume flow rate. The mass flow rates required for the inlet boundary condition of the simulation are determined from a predetermined range of volume flow rates. The values of the mass flow rate at the inlet are given in Table B.1 in Appendix B.

Pressure outlet (2)

A pressure outlet boundary condition is set for the outlet of the total domain (No. 2 in Figure 4.7). The pressure outlet boundary condition is used to set the static pressure to zero and thus simulating an 'open to the environment' condition.

Pressure inlet (3)

A pressure inlet boundary condition is set on the upper part of the outlet domain (No. 3 in Figure 4.7). The reason for not using a pressure outlet boundary condition is because initial tests, with a pressure outlet boundary condition set at the outlet upper shroud, showed that air is drawn in from the outlet upper shroud, especially for high flow rates. Therefore using an inlet- instead of an outlet boundary reverses the direction of the flow regarded as backflow. Thus, using a pressure inlet boundary condition the outward flow is regarded as backflow. The greatly reduced number of cells experiencing backflow, using the pressure inlet boundary condition, improves convergence and reduces the computational time of the solver (ANSYS Fluent Inc., 2017).

An additional difference between the pressure inlet and -outlet boundary condition is the definition of the gauge pressure. The pressure inlet boundary condition uses a gauge total pressure, while the pressure outlet boundary condition uses a gauge static pressure. This, however, does not have a significant effect on the solution since the velocity of the flow over this boundary is small. Additionally ANSYS Fluent Inc. (2017) states that the total pressure specified will be used as a static pressure if flow exits through a pressure inlet boundary.

Walls (4)

Wall boundary conditions are assigned to the remaining boundaries, shown by the number 4 in Figure 4.7. Surfaces that would not exist as a solid surface in a physical setup, such as the ones that are part of the outlet sub-domain, are modelled as a slip wall with a zero shear stress. These surfaces are created in the simulation to create a control volume and to direct the flow.

A non-slip wall boundary condition is set for the fan blade, the ball-nose hub and the bell mouth shroud. The hub and the blade rotate around the axis at a constant rotational velocity, thus the wall boundary is defined as a moving wall, relative to the adjacent cell zone at 0 rad/s. The hub and blade thus rotate with the rotating domain. The shroud on the other hand remains stationary. Since all three sub-domains rotate at a constant rotational speed around the positive z-axis, the shroud wall boundary must counteract the movement to remain static relative to the fan blade. Therefore the shroud wall boundary is defined as a moving wall, relative to the adjacent cell cell zone at a negative rotational speed. For the case of the 1.542 m diameter B2a-fan the rotational speed of the 3 sub-domains is 78.54 rad/s, while the shroud rotates at a speed -78.54 rad/s relative to the cell zone.

4.8 Turbulence modelling

The Reynolds Averaged Navier-Stokes Simulation (RANS) approach is the most widely used approach for industrial flow problems (ANSYS Fluent Inc., 2015). The RANS approach applies a time-averaged procedure to the Navier-Stokes equations, thus considering the mean flow quantities only. An additional Reynolds stress term ($-\rho\overline{u_i' u_j'}$) is also added to the Navier-Stokes equation. The small-scale turbulent fluctuations are thus not directly simulated, which greatly reduces the computational cost and -time. (Versteeg and Malalasekera, 2007)

The Reynolds Averaged continuity and momentum equation is as follows:

Continuity:

$$\frac{\partial \rho}{\partial t} + \frac{\partial}{\partial x_i}(\rho u_i) = 0 \tag{4.3}$$

Reynolds-averaged momentum equation:

$$\frac{\partial \rho u_i}{\partial t} + \frac{\partial}{\partial x_j}(\rho u_i u_j) = -\frac{\partial p}{\partial x_i} + \frac{\partial}{\partial x_j}\left[\mu\left(\frac{\partial u_i}{\partial x_j} + \frac{\partial u_j}{\partial x_i} - \frac{2}{3}\delta_{ij}\frac{\partial u_l}{\partial x_l}\right)\right] + \frac{\partial}{\partial x_j}(-\rho\overline{u_i' u_j'}) \tag{4.4}$$

Several turbulence models that are based on the RANS approach are available. The Spalart Allmaras- and the k-ϵ turbulence model and its variables are applicable examples of RANS based turbulence models. The transport equation for the Spalart Allmaras turbulence model is shown in the following equation:

$$\frac{\partial \rho \tilde{\nu}}{\partial t} + \frac{\partial}{\partial x_i}(\rho \tilde{\nu} u_i) = \frac{1}{\sigma_{\tilde{\nu}}}\left[\frac{\partial}{\partial x_j}\left\{(\mu + \rho\tilde{\nu})\frac{\partial \tilde{\nu}}{\partial x_j}\right\} + C_{b1}\rho\left(\frac{\partial \tilde{\nu}}{\partial x_j}\right)^2\right] + C_{b1}\rho\,\tilde{\nu}\,\tilde{\Omega} - C_{w1}\rho\left(\frac{\tilde{\nu}}{\kappa y}\right)^2 f_w \tag{4.5}$$

The Spalart Allmaras turbulence model, shown in Equation 4.5, is a one-equation model that solves for the kinematic eddy viscosity using a single transport equation. Compared to other one-equation models, the length scale of the Spalart Allmaras model no longer needs to be related to the local shear layer thickness. (Spalart *et al.*, 1994).

The Spalart Allmaras model is able to properly resolve the viscous sub-layer of the boundary, provided the mesh is sufficiently fine. The ideal y+ value of the Spalart Allmaras model is y+ = 1. The near-wall gradients of the transported variables are much smaller than the gradients of the transported variables in other RANS based models. This makes the model attractive for flow problems with wall-bounded flow. (Spalart *et al.*, 1994)

The Spalart Allmaras model is mainly used for aerospace and turbomachinery applications. The model has proven a good performance for boundary layer flow with adverse pressure gradient, especially for two-dimensional flow problems. Three-dimensional, free shear flow and flow with abrupt changes from wall-bounded to free shear flow perform poorly with the Spalart Allmaras model. (Versteeg and Malalasekera, 2007)

The k-ϵ turbulence model is a two-equation model, which uses the solution of two transport equations to define the turbulent velocity- and length scales. The transport equations for k and ε are given in Equation 4.6 & 4.7.

$$\frac{\partial(\rho k)}{\partial t} + \frac{\partial}{\partial x_i}(\rho k u_i) = \frac{\partial}{\partial x_j}\left[\left(\mu + \frac{\mu_t}{\sigma_k}\right)\frac{\partial k}{\partial x_j}\right] + 2\mu_t S_{ij}^2 - \rho\varepsilon \tag{4.6}$$

$$\frac{\partial(\rho\varepsilon)}{\partial t} + \frac{\partial}{\partial x_i}(\rho\varepsilon u_i) = \frac{\partial}{\partial x_j}\left[\left(\mu + \frac{\mu_t}{\sigma_\varepsilon}\right)\frac{\partial \varepsilon}{\partial x_j}\right] + C_{1\,\varepsilon}\frac{\varepsilon}{k}2\mu_t S_{ij}^2 - C_{2\,\varepsilon}\,\rho\frac{\varepsilon^2}{k} \tag{4.7}$$

The k-ϵ model is semi-empirical, basing the values of some of the parameters on experimental data. The model makes use of wall functions to resolve the near-wall region of the flow. The k-ϵ model is robust, economical and applicable for a wide range of turbulent flows, due to several available variants of the model. (Versteeg and Malalasekera, 2007)

The *Realizable* k-ϵ with a *Standard* wall function is used in this thesis. The turbulence intensity is set to 2 % with a 0.01 length scale. The model requires a y+ value in the range of 30<y+<300. The *Realizable* k-ϵ is suitable for complex shear flow with locally transitional flows, vortices and moderate swirl, thus providing good results for boundary layer separation and vortex shedding scenarios (ANSYS Fluent Inc., 2017). Therefore, the *Realizable* k-ϵ is expected to perform well for flows involving rotation. The k-ϵ model, specifically the *Realizable k-ϵ* with the *Standard wall function*, is the least computationally expensive model. (ANSYS Fluent Inc., 2015). Apart from literrature, the use of the *Realizable* k-ϵ with a *Standard* wall function was also based on the study conducted by Louw (2015), which determined the performance of several turbulence models.

4.9 Solution methods and control

The B2a-fan is modelled assuming incompressible flow, thus the pressure-based solver is used. The pressure-based solver computes the velocity field from the momentum equations. A pressure-velocity coupling algorithm is then utilised to determine the pressure and correct the velocity field such that mass conservation (continuity) is fulfilled. The *SIMPLE* pressure-velocity coupling is used, which is ideal for steady-state simulations. The *Least Squares Cell Based* scheme is used to determine the gradients of the solution variables. This scheme provides fair accuracy for highly skewed or distorted mesh and can be used with any mesh type. The *Least Squares Cell Based* scheme is less computational expensive than the *Green-Gauss Node based* scheme. The *PRESTO!* scheme is used for the discretisation of pressure, as it is suitable for highly swirling flows, strongly curved domains and flows with large pressure gradients. The *QUICK* or the *second-order upwind* scheme is used for the discretisation of momentum, turbulent kinetic energy and turbulent dissipation rate. The *QUICK* scheme is a third-order accurate discretisation scheme that provides high solution accuracy, especially for meshes aligned with the flow direction, such as the structured mesh created in the blade passage domain and at the entrance and exit to the blade passage. The scheme is applicable to quad and hex shaped meshes and is specifically suited for rotating and swirling flows. *Fluent* resorts to the *second-order upwind* discretisation scheme for unstructured meshes if *QUICK* is selected. (ANSYS Fluent Inc., 2015)

A surface monitor of the mass flow entering the inlet sub-domain and exiting at the outlet upper shroud and the outlet-out boundary is set up to monitor solution convergence and to make sure that there is no mass imbalance in the domain, i.e. that continuity is fulfilled. Since the total pressure at the inlet is needed to determine the fan static efficiency, it is important to make sure that there are no pressure fluctuations. Thus, a monitor of the mass-weighted averaged total pressure at the inlet was created to monitor solution convergence. The under-relaxation factors are adjusted, depending on the mass flow rate set at the inlet boundary, in order to stabilize the solution and achieve solution convergence.

Chapter 5

Results

In this chapter the results of the numerical analysis are presented. The simulations were conducted using the *Fluent* CFD solver on either a stand-alone computer or on the Rhasatsha high-performance computer (HPC) facility at Stellenbosch University, depending on the size and the required computational time of the simulation.

5.1 Flow visualization

The streamlines of the 1.542 m diameter B2a-fan over the entire flow domain are shown Figure 5.1, in which the flow moves from the left to the right. Flow recirculation can be seen along the bottom of the outlet sub-domain, which occurs due to the backward facing step immediately downstream of the fan. With an increase in distance away from the fan, the exhaust flow of the fan loses momentum and thus flows outwards. The exhaust flow of the fan draws in air through the upper boundary of the outlet sub-domain, which is the reason for using a pressure-inlet boundary condition as discussed in Section 4.7. Numerical analysis showed that the drawn-in air has a low flow velocity.

As shown in Figure 5.2 the flow path differs noticeably for low and high flow rates. Recirculation is expected to occur in the region behind the hub, since a backward facing step is present at the outlet of the blade passage. At a low flow rate ($\varphi = 0.105$) the flow momentum is less, which makes the main fan output stream more succeptable to the effects of the recirculating flow. Figure 5.2 (a) shows reversed flow occurring close to the hub of the fan at a low flow rate. The reversed flow opposes the approaching flow stream. As a result of the flow blockage as well as the low momentum of the flow stream, the exhaust flow of the fan is pushed upwards in the radial direction, hence the fan output stream exits the fan domain at a steeper angle, as evident from the flow paths in Figure 5.2 (a). A smaller second recirculation region, not visible

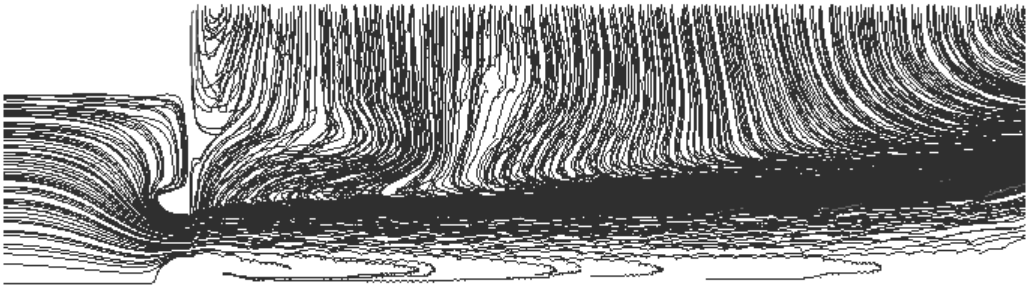

Figure 5.1: The streamlines of the 1.542 m diameter B2a-fan blade at the design point ($\varphi = 0.168$)

in the figure, occurs at the upstream side of the fan blade close to the blade tip. Both recirculating regions increase in size as the flow coefficient decreases.

The recirculation results in flow blockage and consequently a decrease in fan efficiency. According to Kröger (1998), the reverse flow intensifies as the flow resistance is increased, resulting in a more unsteady and transient flow field at a low flow rate.

At a high flow rate the flow momentum is high, thus the flow exits the blade passage domain at a horizontal angle, as seen in Figure 5.2 (c). The small portion of the flow bleeding off downwards in Figure 5.2 (c) is the result of flow rotation and residual recirculation.

Numerical analysis showed that the flow coefficient at which recirculation at the downstream region of the hub and the upstream region of the blade tip commences, decreases as the fan diameter and thus the Reynolds number decreases. Recirculation of the 0.63 m fan occurs at a flow coefficient $\varphi \leq 0.137$, while recirculation in the 1.542 m and the 9 m fan system occurs at $\varphi \leq 0.147$ and $\varphi < 0.158$ respectively. The recirculation can be minimized by locating a disc on the downstream side of the hub or altering the geometry of the ball nose hub (Kröger, 1998).

5.2 Fan performance evaluation

As previously mentioned, the fan pressure-, efficiency- and power curves characterize the performance of the fan. The numerical results obtained from the CFD analysis is compared to the experimental results obtained by Conradie (2010) for the 0.63 m diameter fan and by Louw (2015) for the 1.542 m fan. No experimental data is available for the 9 m B2a-fan, since the size of the fan

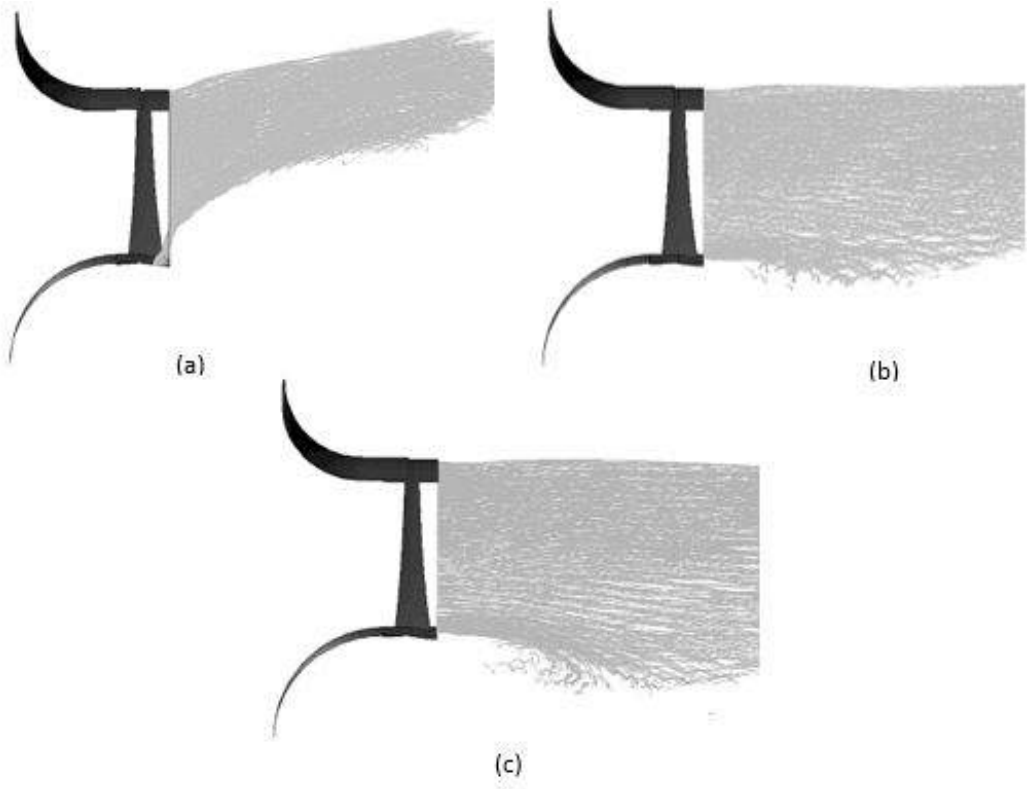

Figure 5.2: The flow pathlines at the downstream interface of the 1.542 m diameter B2a-fan blade at a flow coefficient of: (a) $\varphi = 0.105$ (b) $\varphi = 0.168$ and at (c) $\varphi = 0.211$

does not permit testing in a BS 848 fan test facility.

5.2.1 1.542 m diameter fan results

The numerical flow analysis was conducted using the *Realizable* k-ϵ turbulence model with a *Standard* wall function. This model requires the y+ value along the solid surfaces, i.e. the fan blade, hub and shroud, to be in the range: 30<y+<300. The y+ value at a constant span along the blade chord is shown in Figure 5.3. The y+ value at the minimum-, design- and maximum flow coefficient is plotted. The bold horizontal line indicates a y+ value of 30, which is the lower limit of the required y+ range for the selected turbulence model. The vast majority of the fan blade meets the y+ criteria, with the exception of a small region at the leading- and trailing edge of the fan blade. Due to this the boundary layer in these regions might not be resolved correctly by the turbulence model. Since the region in which the y+ is below the minimum is so small, the contribution to the resulting discrepancy between numerical and experimental results is minimal. Due to the flow conditions and the blade geometry, achieving a y+ value in the desired range in the leading- and trailing

edge region, is impractical, since it comes at a cost of a severely reduced mesh quality.

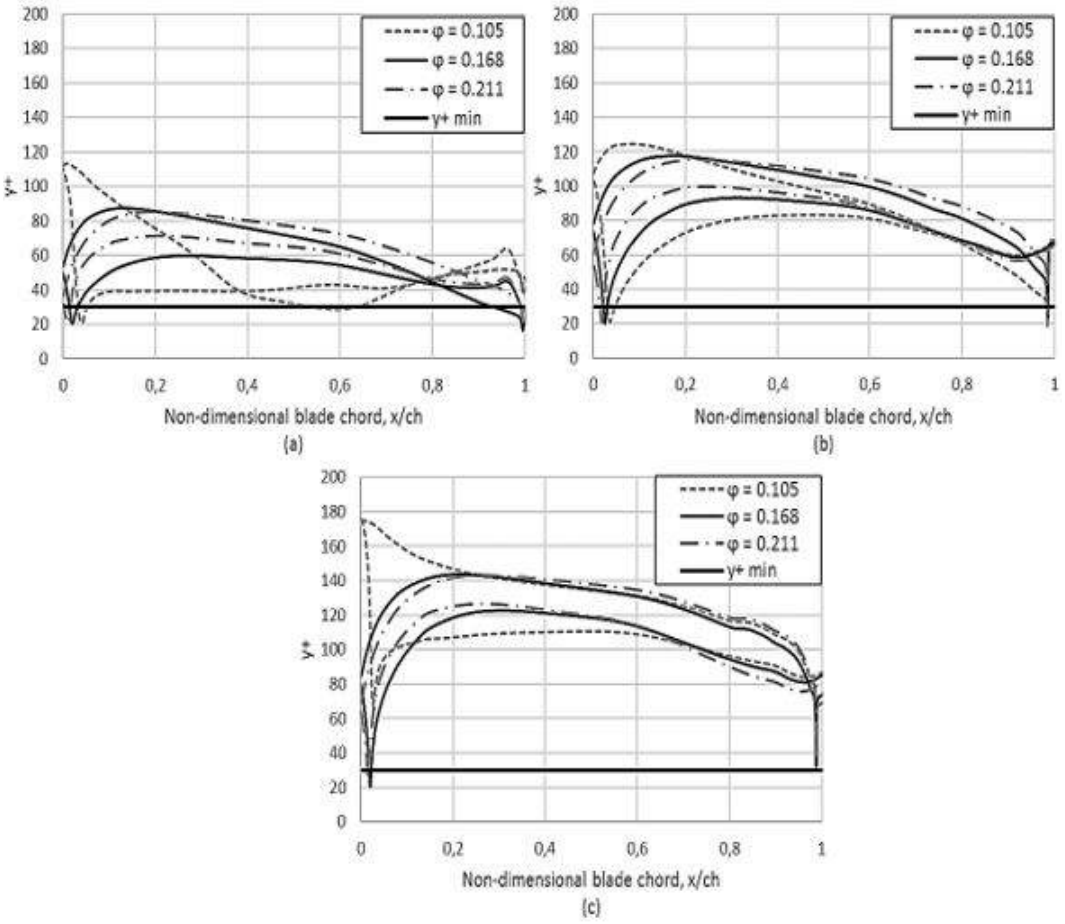

Figure 5.3: The y+ values of the 1.542 m diameter B2a-fan blade along non-dimensional span of (a) s=0.1, (b) s=0.5 and (c) s=0.9

The experimental and the numerical results of the fan static pressure at different volume flow rates is shown in Figure 5.4. The experimental results of the 1.542 m diameter B2a-fan were obtained by Louw (2015) in a BS 848 type A fan test facility at the University of Stellenbosch. The comparison shows a discrepancy between the experimental and the numerical results for off-design conditions. The design point of the B2a-fan lies at a flow coefficient of $\varphi = 0.168$. The numerical analysis computes a higher fan static pressure and efficiency at low flow rates compared to the experimental test. At flow rates higher than the design point, this effect reverses resulting in a lower fan static pressure compared to the experimental test. Effectively this means that the numerical analysis over-predicts the fan static pressure and -efficiency at low flow rates and under-predicts the fan static pressure and -efficiency at high

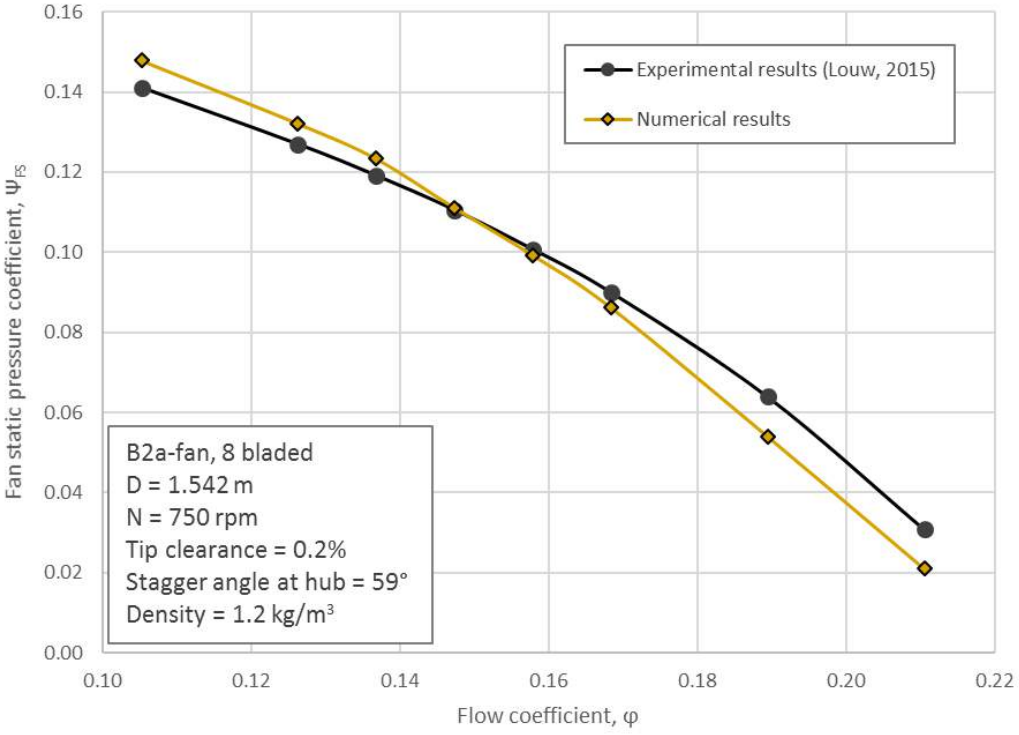

Figure 5.4: Fan static pressure of the 1.542 m diameter B2a-fan

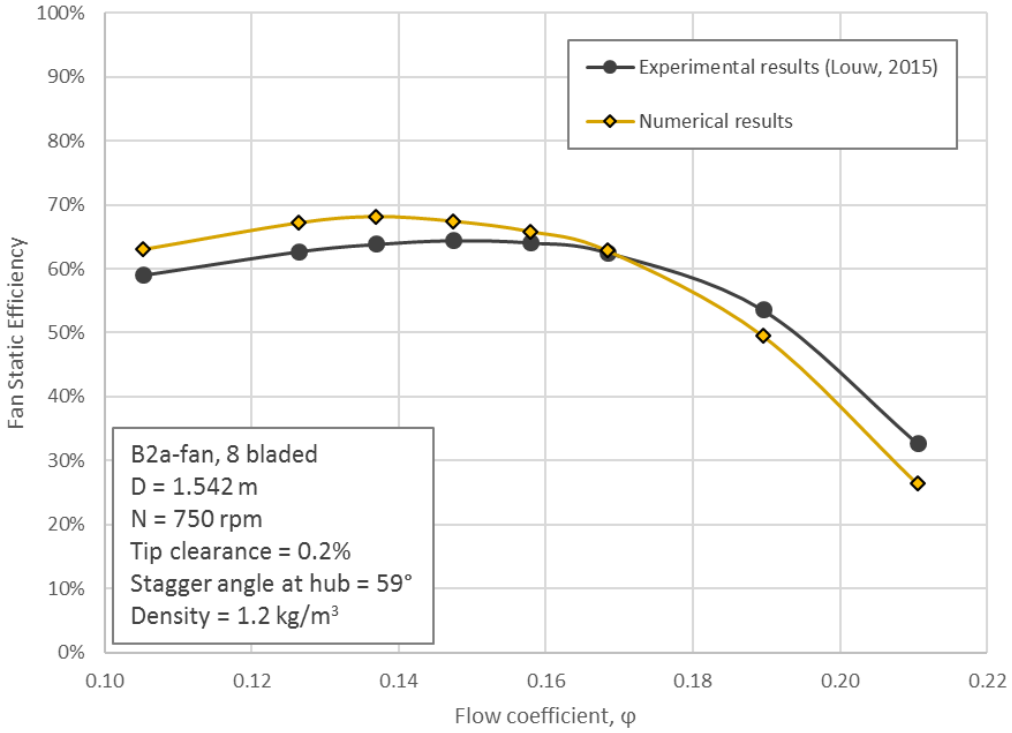

Figure 5.5: Fan static efficiency of the 1.542 m diameter B2a-fan

flow rates.

Figure 5.6 shows the change in power coefficient with flow coefficient. The results show a deviation of the numerical results from the experimental results. The power coefficient of the numerical model is smaller than the power coefficient of the experimental results. This deviation is however near constant over the range of flow coefficients.

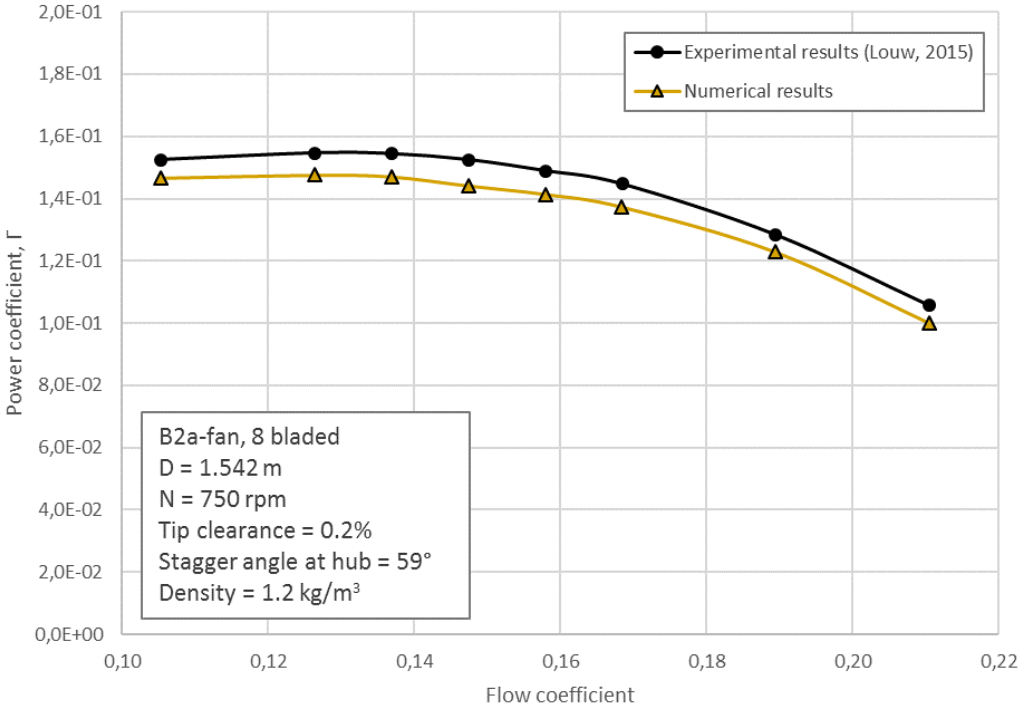

Figure 5.6: Comparison of the experimental- to the numerical results of fan power for the 1.542 m diameter B2a-fan

The CFD analysis conducted by Louw (2015) for the 1.542 m diameter B2a-fan showed the same effect. The over-prediction of fan static efficiency by the numerical model is slightly less in Louw's work. Louw conducted a time-dependent numerical analysis below a flow coefficient of $\varphi = 0.137$, due to the onset of reversed flow patterns near the hub, as discussed in Section 5.1. The instability of the flow increases as the flow coefficient decreases. The analysis by Louw (2015) showed that for the tested flow coefficient range of $0.04<\varphi<0.2$ the numerical model, using the Realizable k-epsilon turbulence model, under-predicts the fan static pressure and -efficiency, except for a flow coefficient in the range of $0.1<\varphi<0.15$, for which the numerical results over-predict the fan static pressure and efficiency compared to the experimental results.

5.2.2 Down-scaled fan performance

The 0.63 m fan model is created by scaling the 1.542 m fan by a factor of 0.40856, as explained in Section 4.5. This not only scales the fan blade and the domain but also the mesh. As a result the inflation layer becomes too thin i.e. a large portion of the wall surfaces has a y+ value below 30. To resolve this issue the first layer height of the inflation layers is increased before downscaling the fan to a diameter of 0.63 m.

The resultant y+ range at a constant span along the blade chord is shown in Figure 5.7. The y+ value at the minimum-, design- and the maximum flow rate is plotted for a span of 0.1, 0.5 and 0.9. As shown in Figure 5.7, the vast majority of the blade chord at the measured blade span ratio has a y+ value greater than 30. Near the hub (s=0.1) a greater portion of the blade has a y+ value below 30. Since it is only a small portion along the blade chord and only close to the hub the predicted effect is minimal.

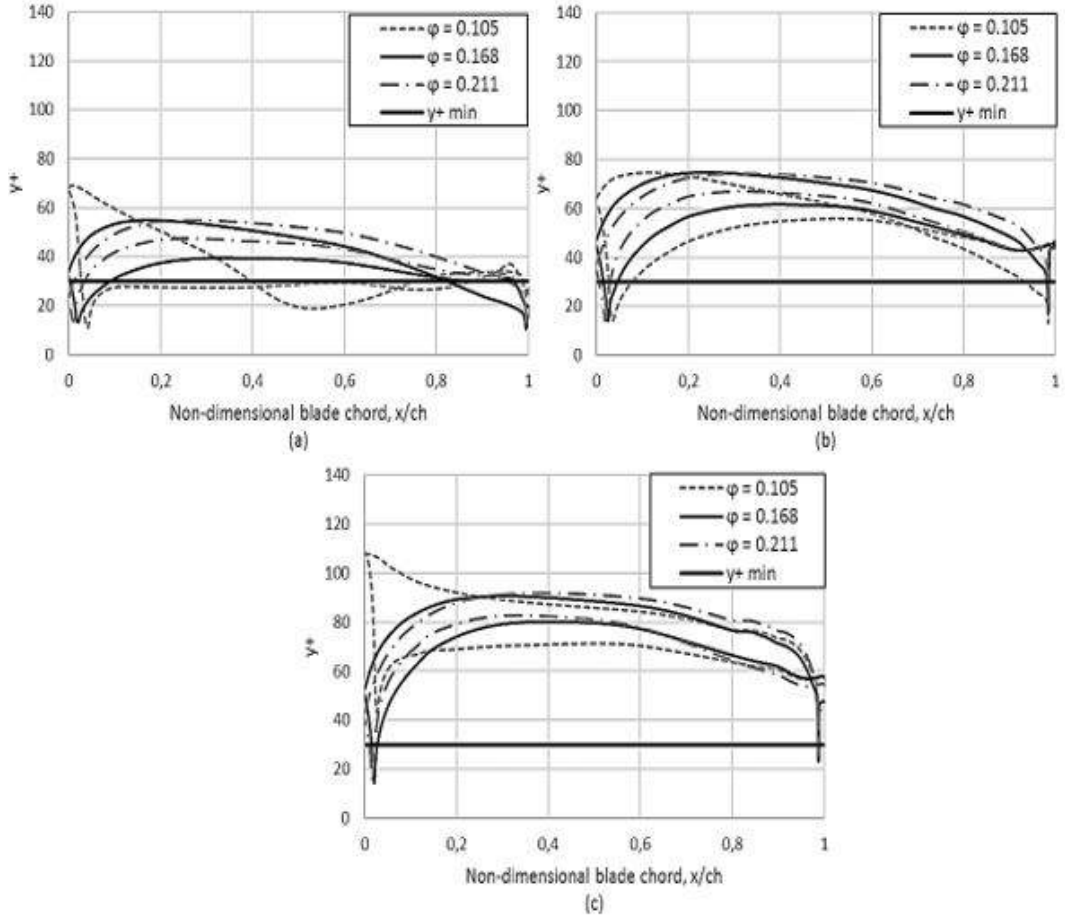

Figure 5.7: The y+ values of the 0.63m diameter B2a-fan blade along non-dimensional span of (a) s=0.1, (b) s=0.5 and (c) s=0.9

As mentioned in Section 3.2, the experimental model of the 0.63 m B2a-fan has a lower tip clearance ($t/d = 0.127$ %) compared to the 1.542 m model ($t/d = 0.2$ %). The numerical model of the 0.63 m, 1.542 m and the 9 m fan all have a 0.2 % tip clearance since they are scaled versions of the 1.542 m model. Before the numerical results of the 0.63 m fan can be compared to the experimental results supplied by Conradie (2010), the effect of the tip clearance difference has to be analysed.

Figure 5.8 & 5.9 show the experimental results of the 0.63 m fan, having a 0.127 % tip clearance, together with the numerical results of the 0.63 m model with a 0.127 % and 0.2 % tip clearance. Comparison of the numerical results of the fan with a 0.127 % and a 0.2 % tip clearance shows that the smaller tip clearance ($t = 0.127$ %) results in a slightly higher efficiency compared to the fan with a 0.2 % tip clearance, due to reduced tip clearance losses. The comparison shows a small difference in fan static pressure and -efficiency between a fan with a 0.127 % and a 0.2 % tip clearance. In fact the average absolute difference in efficiency between the numerical models with different tip clearances is 0.82 % with the largest difference in efficiency occurring in the region close to the maximum efficiency point.

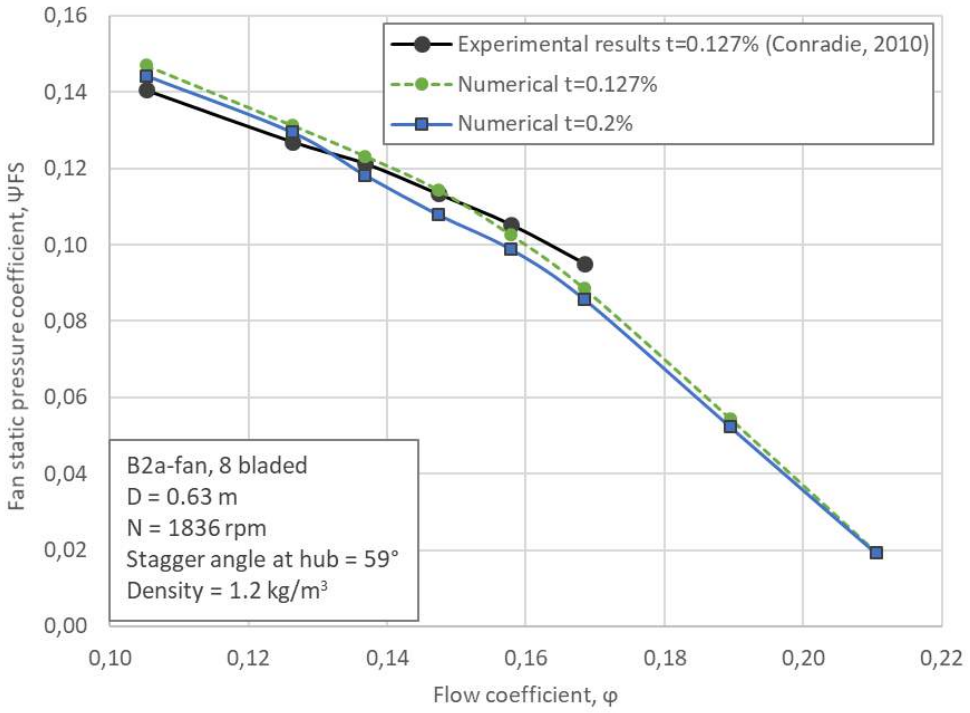

Figure 5.8: Effect of tip clearance on the fan static pressure of the 0.63 m diameter B2a-fan

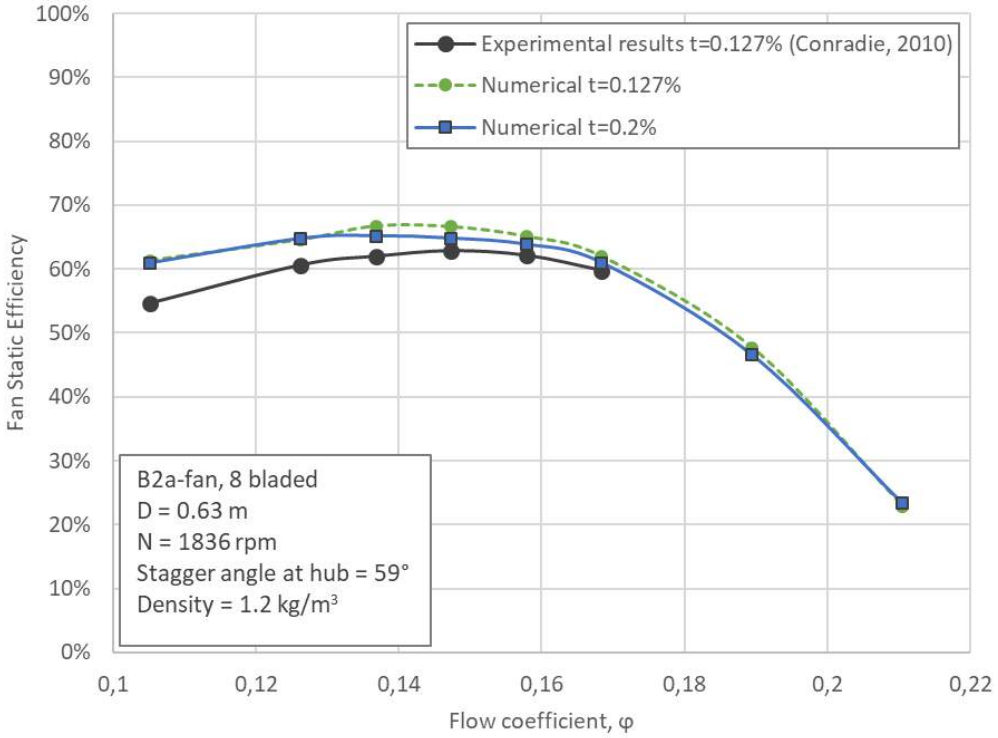

Figure 5.9: Effect of tip clearance on the fan static efficiency of the 0.63 m diameter B2a-fan

A discrepancy between the experimental and numerical results with an equal tip clearance (0.127 %) exists. Similar to the results of the 1.542 m fan, shown in Figure 5.4 and 5.5, the numerical analysis of the fan with a 0.127 % tip clearance computes a higher fan static pressure at a low flow rate and a lower fan static efficiency at a high flow rate. The intersection between the experimental- and numerical fan static pressure curve lies, for both the 1.542 m and the 0.63 m fan, at a flow coefficient of $\varphi = 0.147$. It should be noted that the experimental tests, conducted by Conradie (2010), were performed in a Type B fan test facility, while the numerical models of the 0.63 m, 1.542 m and 9 m diameter fan, as well as the experimental tests of the 1.542 m fan, are based on a Type A setup.

The power coefficient over the range of flow coefficient is shown in Figure 5.10. The results show that the numerical analysis under-predicts the power coefficient.

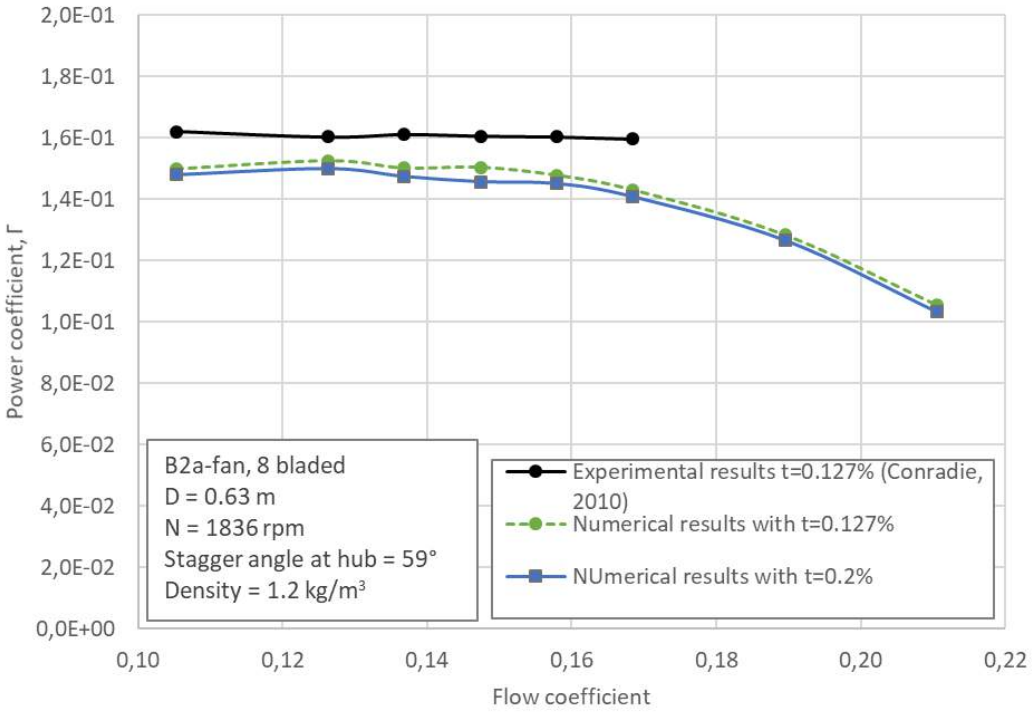

Figure 5.10: Comparison of the experimental- to the numerical results of fan power for the 0.63 m diameter B2a-fan

5.2.3 Up-scaled fan performance

The 1.542 m diameter B2a-fan was scaled by a factor of 5.8366, as explained in Section 4.5. Contrary to the downscaling of the fan, the first layer height of the inflation layer needs to be decreased before scaling the 1.542 m fan to a 9 m diameter size. The domain and its mesh is scaled by the scaling factor, which causes the first layer height to be greater than the first layer height of the 1.542 m diameter model. This results in a y+ range exceeding the range required by the *Realizable* k-ϵ turbulence model with a *Standard* wall function. The y+ range at a constant span along the blade chord for different flow rates is shown in Figure 5.11. As seen in Figure 5.11 the y+ is above the minimum value of 30 except for a very small portion of the blade at the leading and trailing edge of the blade. The y+ exceeds the upper limit of 300 in the region close to the blade tip (s=0.9) at a low flow rate. This region exceeding the y+ range makes up about 3% of the total blade chord, thus the effect of the exceeding y+ on the solution is minimal.

The solution results for the fan static pressure and the -efficiency are shown in Figure 5.12 & 5.13 together with the numerical results of the 1.542 m and the 0.63 m fans. Due to the size of the 9 m fan no experimental data is available.

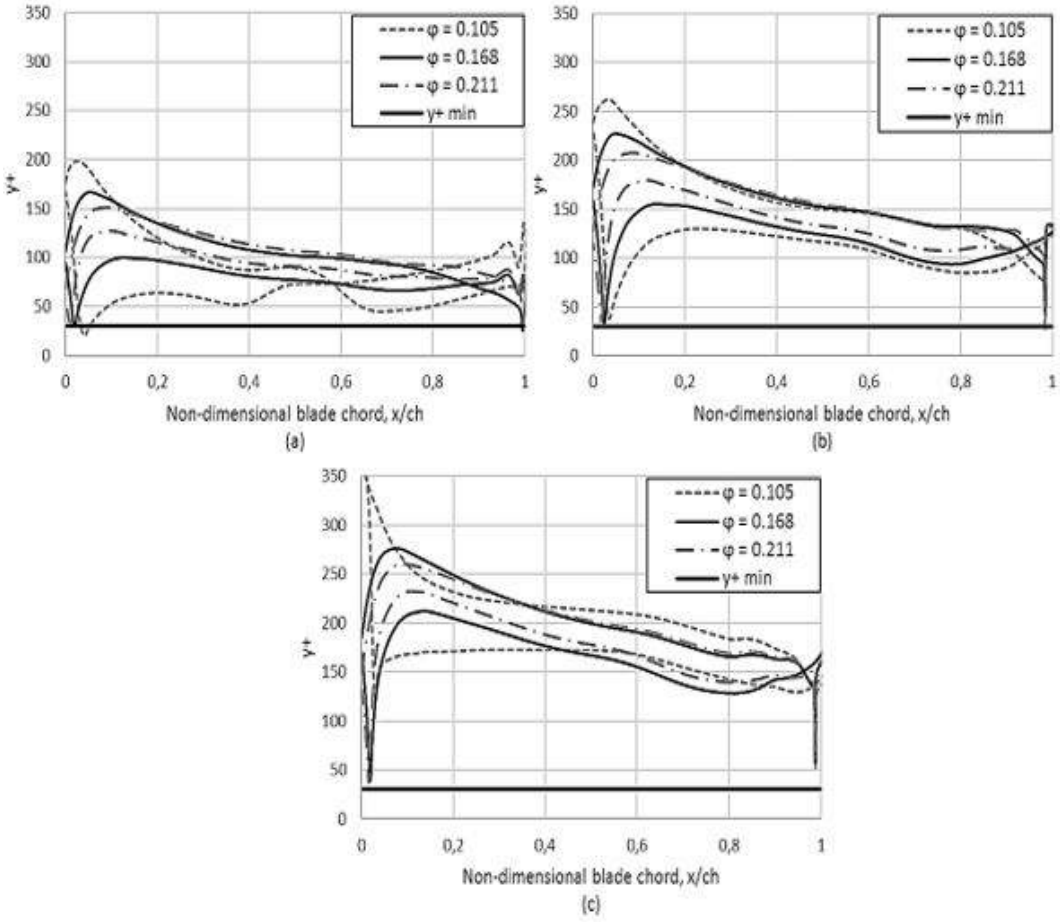

Figure 5.11: The y+ values of the 9 m diameter B2a-fan blade along non-dimensional span of (a) s=0.1, (b) s=0.5 and (c) s=0.9

5.3 Scaling effect

The fan curves of the 0.63 m, the 1.542 m and the 9 m diameter B2a-fans are shown in Figure 5.12 & 5.13. Dimensional analysis showed that the fan static pressure of the model (ΔP_m) should be equal to the fan static pressure of the prototype (ΔP_p), since the ratio of the rotational speed (N) is the inverse of the ratio of the fan diameters (d), shown in Equation 5.1 below. This stems from matching the blade tip speeds.

$$\frac{\Delta P_{p_{sf}}}{\Delta P_{m_{sf}}} = \left(\frac{N_p}{N_m}\right)^2 \left(\frac{d_{p_{fc}}}{d_{m_{fc}}}\right)^2 \tag{5.1}$$

The numerical results, shown in Figure 5.12, show a very small deviation in fan static pressure for a flow rate at and above the design point ($\varphi \geq 0.168$). For a low flow rate the deviation in results increases, reaching a maximum at

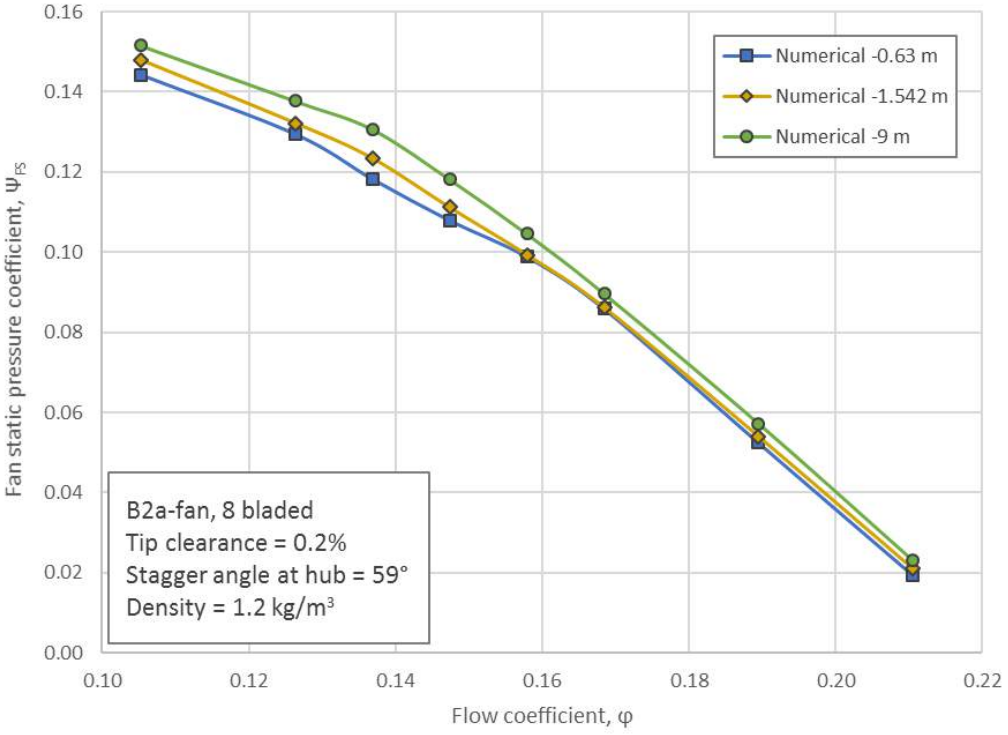

Figure 5.12: Numerical fan static pressure comparison of the geometrically scaled B2a-fans

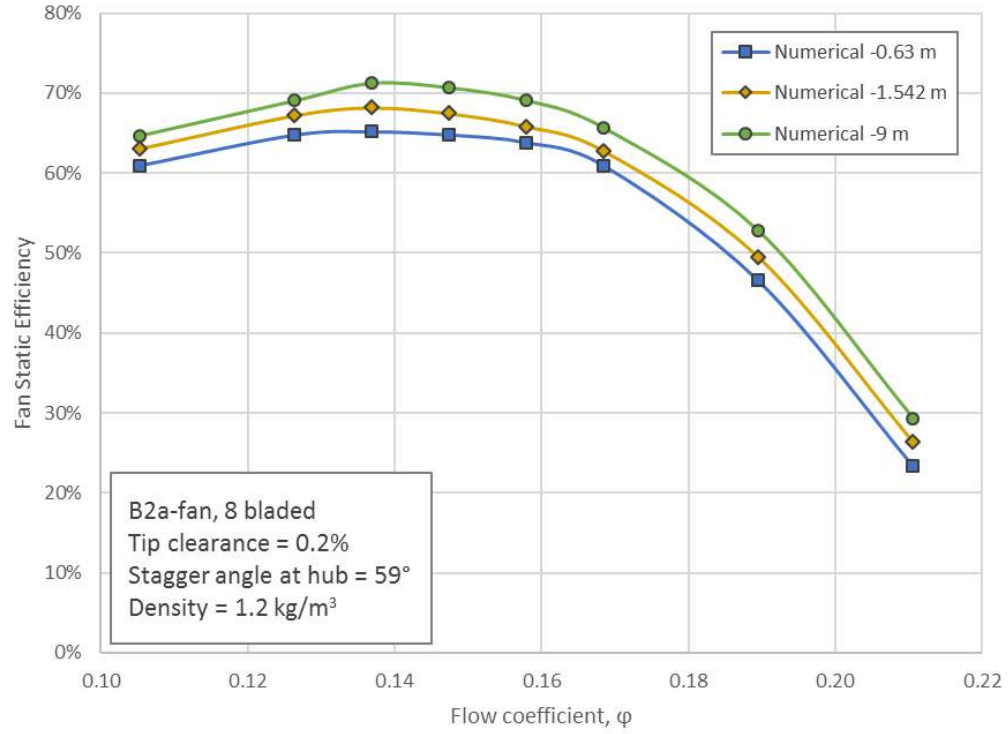

Figure 5.13: Numerical fan static efficiency comparison of the geometrically scaled B2a-fans

the peak efficiency point ($\varphi = 0.137$). A larger deviation is exhibited at a low flow rate than at a high flow rate. A general increase in fan static pressure is seen for an increase in fan size and thus Reynolds number, at the same flow coefficient.

According to the affinity laws the efficiency of the prototype should be equal to the efficiency of the model, as given by Equation 2.7. In reality this is not the case, since the affinity laws neglect viscous effects and changes in Reynolds number. As seen in Figure 5.13, the efficiency increases with an increase in fan size and thus Reynolds number. The literature forecasts that both the efficiency and the corresponding flow coefficient increases with an increase in Reynolds number, as shown in Figure 2.5. This effect is not present in the numerical analysis conducted in this thesis. The shift to a higher fan static efficiency is present but the shift to a higher flow coefficient for an increase in Reynolds number is not. According to Hess (2010) this effect does however depend on the fan geometry, blade spacing, blade angle and the flow regime.

The numerical results for power coefficient of the 0.63 m, 1.542 m and the 9 m diameter fan are shown in Figure 5.14. As shown in the figure the power coefficient of the 1.542 m and the 9 m fan model are close to identical, meaning that only a very small difference exists between the results of the two fans. The numerical analysis of the 0.63 m diameter fan produces a slightly higher power coefficient in the high flow rate region, compared to the results of the 1.542 m and the 9 m fan.

The effect of the Reynolds number on the peak fan static efficiency is shown in Figure 5.15. Each horizontal pair of plotted points represents the Reynolds number at the hub and at the tip of a different size fan. The Reynolds number range between the hub and the tip of each fan is given in Appendix B.2

To provide a more detailed analysis over the Reynolds number range, two extra fans are needed for which the Reynolds numbers fall between the Reynolds number of the 1.542 m and the 9 m diameter fan. As a result a 12 ft (3.66 m) and a 24 ft (7.32 m) fan are included, for which only the peak efficiency point is determined and not the entire efficiency range over a range of flow coefficients. From the fan curves of static efficiency, given in Figure 5.13, it is deduced that the peak efficiency is likely to lie at a flow coefficient of 0.137. Thus, the 12 ft and the 24 ft fan are modelled using a flow coefficient of 0.137. To make sure that this deduction is true, a simulation using a higher and a lower flow coefficient is conducted. The required mass flow rate at the inlet is given in Table B.2, which was calculated by scaling the volume flow rate of the 1.542 m diameter fan using the affinity laws given in Equation 2.4. The rotational velocity is determined as shown in Equation 4.1 & 4.2, resulting in a 33.11 and 16.56 rad/s rotational velocity for the 12 and 24 ft fan respectively.

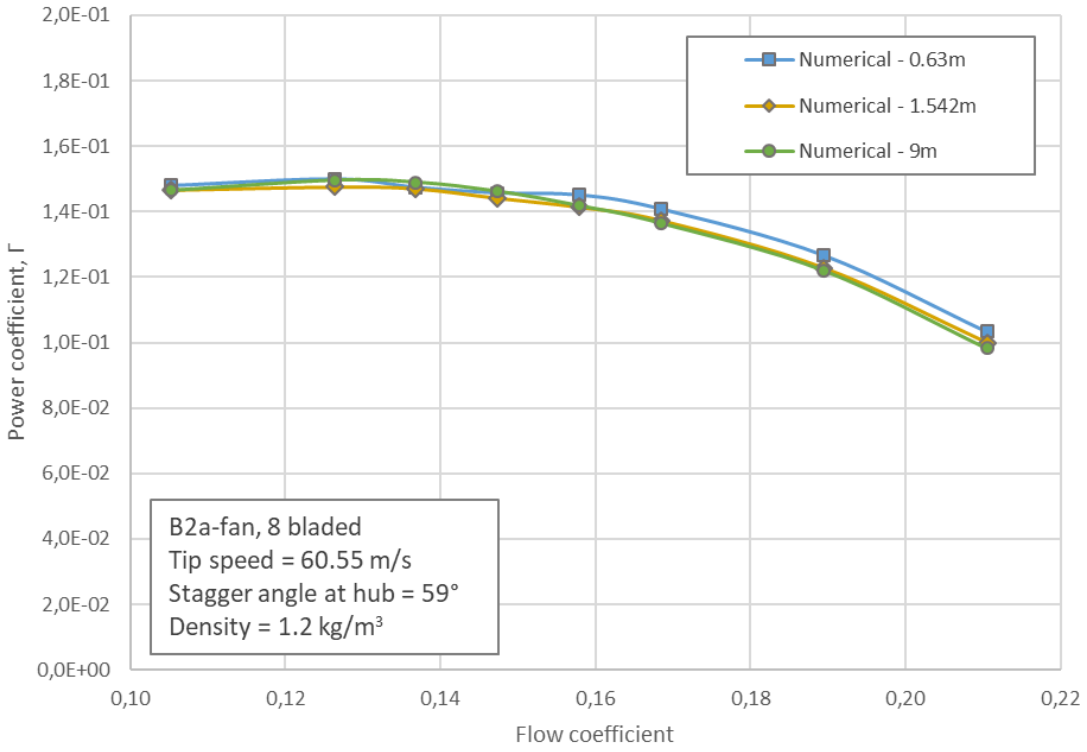

Figure 5.14: Numerical fan power comparison of the geometrically scaled B2a-fan

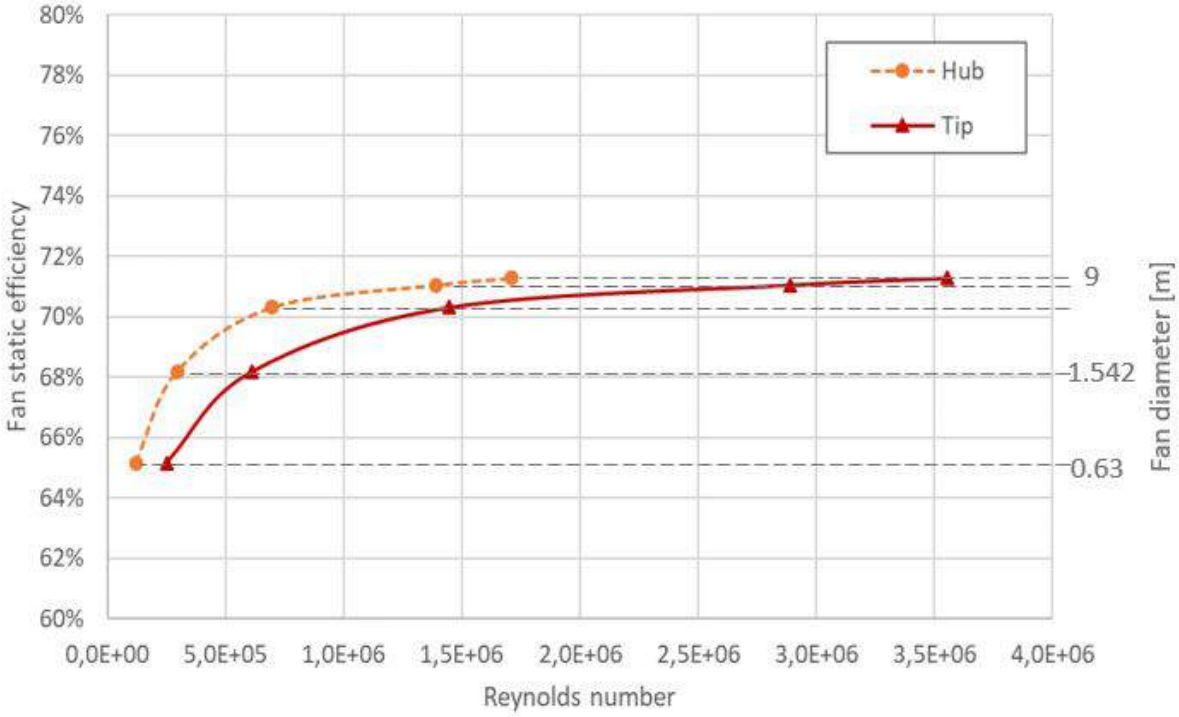

Figure 5.15: The effect of Reynolds number on the peak fan static efficiency of the B2a-fan

The solid line in Figure 5.15 represents the peak efficiency point of a fan at the blade tip. The dotted line represents the peak efficiency of a fan at the same rotational speed but with the Reynolds number based on the blade hub speed. From Figure 5.15 it is evident that the Reynolds number has a logarithmic effect on the peak fan static efficiency. At lower Reynolds number flow a large increase in peak fan static efficiency occurs. The effect of the Reynolds number on the peak fan static efficiency then decreases and eventually no significant change in peak efficiency is experienced for a further increase in Reynolds number. The peak fan static efficiency is then said to be independent of the Reynolds number. This is shown in Figure 2.4. As shown in Figure 5.13 and evident in Figure 5.15, the increase in efficiency between each fan size is in both cases 3.1 % at the peak efficiency point, even though the fan size and the rotational speed between the 1.542 m and the 9 m fan changes by a factor of 5.84 compared to a 2.45 factor change between the 1.542 m and the 0.63 m fan. This is attributed to the logarithmic trend of the Reynolds number effect shown in Figure 5.15.

Comparing the Reynolds number range between the hub and the blade tip in Figure 5.15 & 5.16 shows that the Reynolds number range significantly increases with an increase in fan size. Therefore the 0.63 m diameter fan is likely to experience laminar flow over the blade, while the flow over the 9 m diameter fan blade is likely to be fully turbulent. A transitional flow regime is thus likely to be present on parts or even over the entire blade span of fans with a diameter between 0.63 m and 9 m. The size or Reynolds number range of the transitional flow regime does however depends on the surface geometry, -roughness, turbulence level and the pressure variation along the surface (Cengel and Cimbala, 2010).

Figure 2.8 shows, as discussed in Chapter 2.3, the variation of the friction coefficient with an increase in Reynolds number. In the laminar flow regime the friction coefficient is the highest at a low Reynolds number, which then decreases with an increase in Reynolds number. In the turbulent flow regime the friction coefficient increases with an increase in Reynolds number until it reaches a constant magnitude and no further increase in friction coefficient occurs. As discussed in Chapter 2.2 and 2.3, the viscous/ Reynolds number dependent losses diminish as the Reynolds number increases, such that inertia/Reynolds number independent losses, such as tip clearance losses, dominate. This decrease in Reynolds number dependent losses creates the logarithmic trend of the Reynolds number effect on the fan static efficiency, as seen in Figure 5.15.

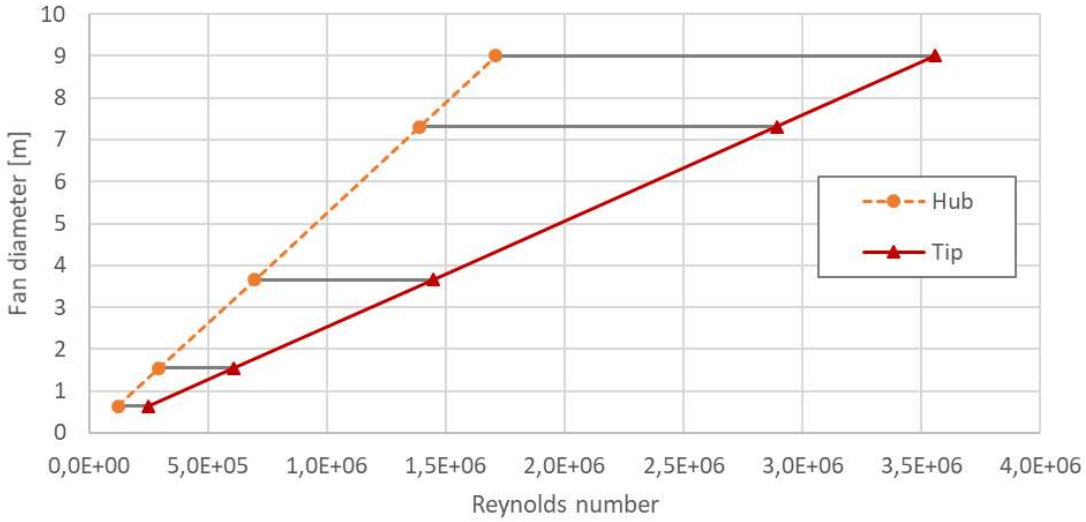

Figure 5.16: The change in Reynolds number range over the blade for a range of geometrically scaled fans with equal tip speed

5.4 2-Dimensional airfoil simulations

The numerical analysis of the B2a-fan shows a discrepancy between the experimental and numerical results. Therefore a two-dimensional numerical analysis is conducted to investigate if differences between the numerical and experimental lift- and drag coefficients exist, which would subsequently influence the fan static efficiency of the fan. In addition, the effect of Reynolds number and turbulence model on the lift- and drag coefficient is investigated.

The NASA LS 0413 airfoil, which is the same used in the B2a-fan, is modelled with a unit length chord. A rectangular flow domain is created with a height of 8 times the blade chord length and a length of 6 and 20 times the chord length in the upstream and downstream direction respectively. The domain is shown in Figure 5.17.

The lift- and drag coefficient is determined at a blade angle of attack of 0°, 5°, 10° and 15°. The blade's center of rotation is, as specified by McGhee and Beasley (1976), at a distance of 0.25 times the chord length from the leading edge along the camber line of the airfoil. The lift- and drag coefficient are determined by Equation 5.2 and 5.3 respectively. An air density of 1.2 kg/m^3 is used in the numerical analysis.

Figure 5.17: Domain extends of the 2-dimensional analysis

$$C_L = \frac{F_L}{0.5\rho U^2 ch} \tag{5.2}$$

$$C_D = \frac{F_D}{0.5\rho U^2 ch} \tag{5.3}$$

A velocity inlet boundary condition is set at the inlet and a pressure outlet boundary condition with a zero gauge pressure is set downstream of the airfoil at the outlet. A slip wall with zero shear stress is set on the upper and lower horizontal domain boundary. A velocity inlet boundary condition is used to obtain the desired Reynolds number flow over the blade. A velocity of 33.458 m/s is set at the inlet to obtain a Reynolds number of 2.2E+06 over the blade, which is the lowest Reynolds number at which experimental data for the LS 0413 airfoil, provided by McGhee and Beasley (1976), is available. The experimental analysis, conducted by McGhee and Beasley (1976), and the numerical analysis both use a chord-based Reynolds number.

To investigate the effect of Reynolds number on the lift and drag coefficient and to obtain results that are comparable to the three-dimensional fan blade, the velocity was set as to match the Reynolds number to that of the midspan of each of the 3-dimensional fan blades. The midspan was chosen as it provides a good average of the lift and drag coefficient experienced over the span of the blade, since the chord of the B2a-fan blade is longer at the hub and shorter at the tip. In addition to that the angle of attack of the blade, as shown in Figure A.4 in Appendix A is highest at the hub and decreases towards the tip. Therefore the maximum lift and drag acts at the blade hub, decreasing to a minimum at the tip of the blade.

A numerical analysis with four different turbulence models was conducted to provide a comparison of the numerical results obtained using the different turbulence models to the experimental results provided by McGhee and

Beasley (1976). The analyses were conducted at a Reynolds number of 2.2E+06. The Realizable $k-\varepsilon$ with the Standard wall function, the Transitional SST and the Spalart-Allmaras model are tested at varying angles of attack, as shown in Figure 5.18, 5.19 & 5.20. Additionally an *XFoil* analysis at varying angles of attack is conducted.

XFoil is a program specifically designed for the analysis of subsonic isolated airfoils. The program is interactive with a collection of options that allow the user to design, analyse and optimise two-dimensional, isolated airfoils under a variety of flow conditions. *XFoil* assumes that the flow domain boundaries are infinitely far away from the airfoil and thus have no effect on the flow over the airfoil. The program uses an integral boundary-layer approach to account for viscous effects and a panel method to predict the outer (potential) flow (Pierce, 2008).

The Realizable k-ε with the Standard wall function requires a y+ in the range 30<y+<300, while the Transitional SST and Spalart Allmaras model fully resolve the boundary layer, requiring a $y \leq +1$. The *XFoil* analysis is conducted with a set Mach number of 0.15 and a forced transition point at a 0.075 chord length. This correlates to the conditions set in the experimental analysis by McGhee and Beasley (1976).

The results of the 2-dimensional airfoil analysis with different turbulence models are shown in Figure 5.18, 5.19 & 5.20. It is evident that the Realizable k-ε model experienced the largest deviations with respect to the experimental results, with the model over predicting both the lift and the drag. The deviation is however near constant over a change in angle of attack. Both the Transitional SST and the Spalart Allmaras model show a good correlation with the experimental lift coefficient at a low angle of attack. At an angle of attack of 10° and 15° the lift coefficient of both models deviate from the experimental results, while no change in the drag coefficient occurs.

At a small angle of attack the Transitional SST model under predicts the drag, resulting in large deviations from the experimental results for the lift to drag ratio. The Spalart Allmaras model has a very small deviation in drag over the change in angle of attack with respect to the experimental results. The results of the *XFoil* simulation shows that it predicts the same lift as the Spalart Allmaras model but predicts a lower drag. The predicted drag by the *XFoil* model is very close to the experimental results except for slight under prediction of the drag at a 5° and 10° angle of attack. Due to over predicting the lift but correctly predicting the drag, a lift-to-drag ratio larger than the experimental lift-to-drag ratio results from the *XFoil* analysis. A similar trend and correlation between the numerical results obtained using different turbulence models was determined in the study by Pierce (2008).

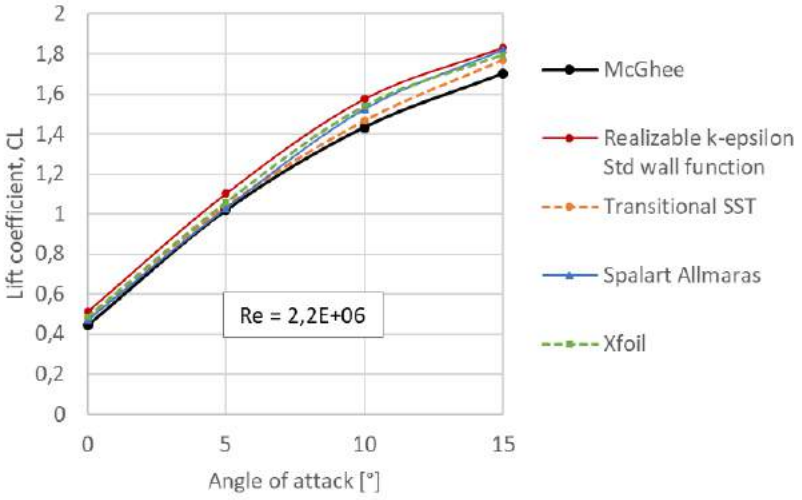

Figure 5.18: Comparison of the lift coefficient (C_L) between different turbulence models of a 2D airfoil at varying angle of attack

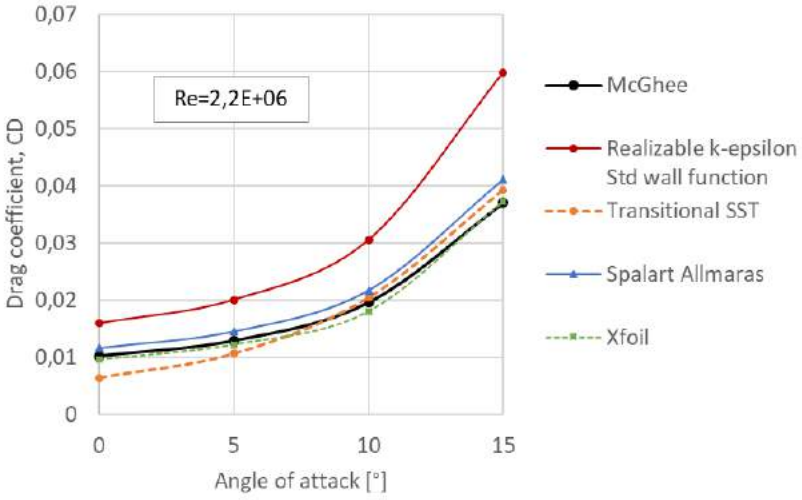

Figure 5.19: Comparison of the drag coefficient (C_D) between different turbulence models of a 2D airfoil at varying angle of attack

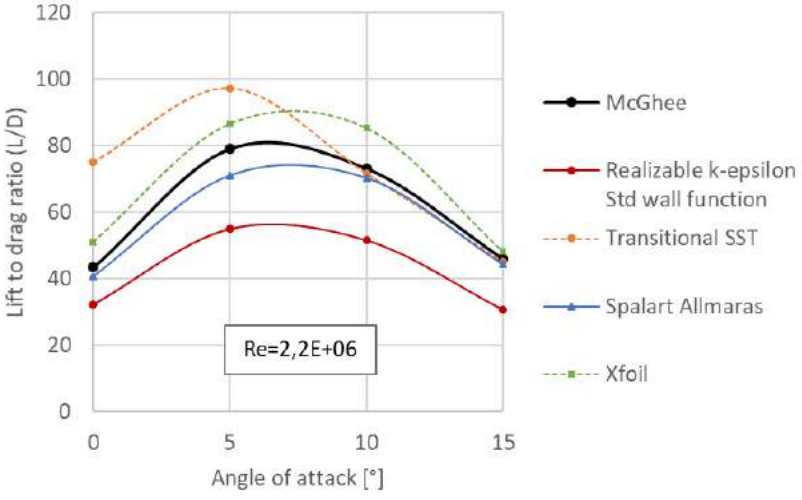

Figure 5.20: Comparison of the lift to drag ratio between different turbulence models of a 2D airfoil at varying angle of attack

The results in Figure 5.18, 5.19 & 5.20 show that the Spalart Allmaras model produces more favourable results than the Realizable k-ε and the Transitional SST model. The numerical analysis shows that the main advantage the Spalart Allmaras model has over the other two turbulence models is the more accurate and consistent prediction of the drag coefficient with a change in the angle of attack, thus producing a lift-to-drag ratio closest to the experimental results.

The comparison of different turbulence models against experiment results and each other showed that the Spalart Allmaras turbulence model predicted a more favourable result than the Realizable k-ε model, which is the turbulence model used in the 3-dimensional analysis of the B2a-fan blade. Therefore the Spalart Allmaras model is compared to the Realizable k-ε model for lower Reynold numbers. The results are shown in Figure 5.21, 5.22 & 5.23. Considering the effect of Reynolds number on each individual model shows a decrease in lift and an increase in drag with an increase in Reynolds number. A near constant deviation with changing angle of attack between the Spalart Allmaras model and the k-ε model is visible from the results for models at the same Reynolds number. The results in Figure 5.23 show a large improvement in lift-to-drag ratio using the Spalart Allmaras model.

The Spalart Allmaras model proved to provide more favourable results than the k-ε model, which is the model used in the three-dimensional analysis of the B2a-fan blade. That begs the question if the large difference in results between the k-ε and the Spalart Allmaras turbulence model would also be present in a three-dimensional analysis of the fan blade. A numerical analysis of the three-dimensional B2a-fan is conducted using the Spalart Allmaras model. The results of the analysis are shown in Figure 5.24 & 5.25 for the 0.63 m fan and in Figure 5.26 & 5.27 for the 1.542 m fan.

The results of the analysis showed a relative close agreement of the Spalart Allmaras and the k-ε model in the three-dimensional analysis. The over- and under-prediction of the fan static pressure and efficiency at a low- and high flow rate respectively, is also present in the results of the Spalarat Allmaras turbulence model. In fact the over- and under-prediction are slightly worse compared to the results of the k-ε model. This might be attributed to the fact that the Spalart Allmaras model is said to perform poorly for three-dimensional flow, as discussed in Section 4.8. The rotation/curvature correction function, available on *ANSYS Fluent*, has been been used in conjunction with the Spalart Allmaras model, as the results of the standard Spalart Allmaras model produces even greater deviations from both the experimental results and the numerical results using the k-ε turbulence model.

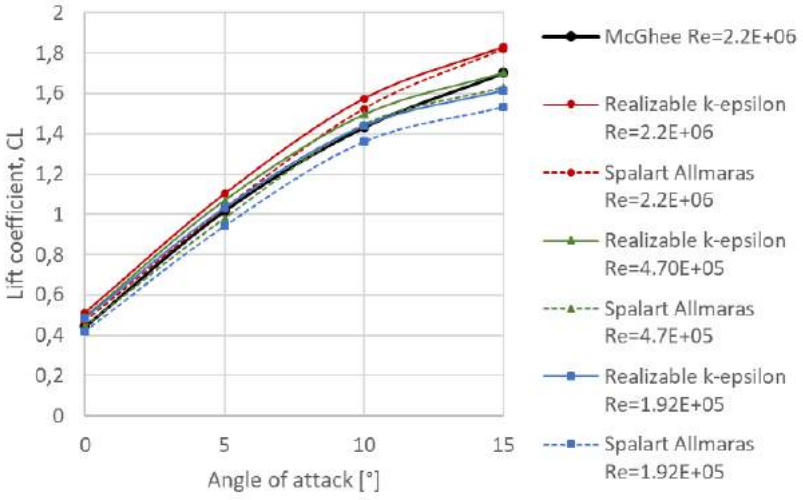

Figure 5.21: Comparison of the lift coefficient (C_L) between the k-ε and the Spalart Allmaras turbulence model of a 2D airfoil at varying angle of attack

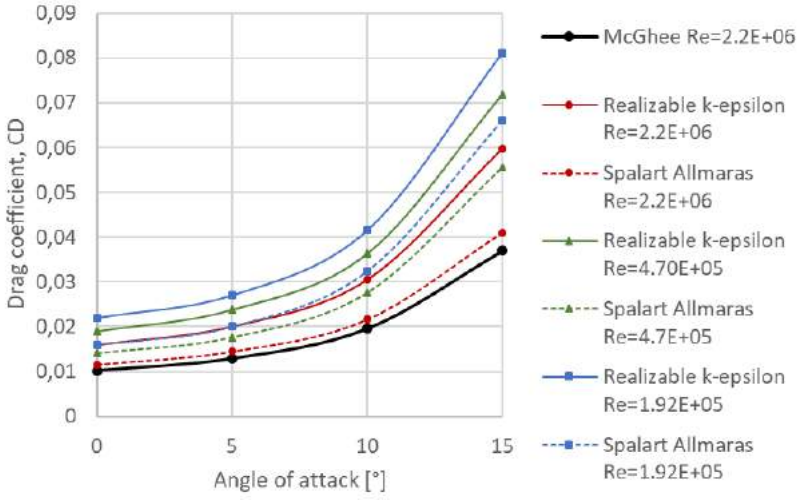

Figure 5.22: Comparison of the drag coefficient (C_D) between the k-ε and the Spalart Allmaras turbulence model of a 2D airfoil at varying angle of attack

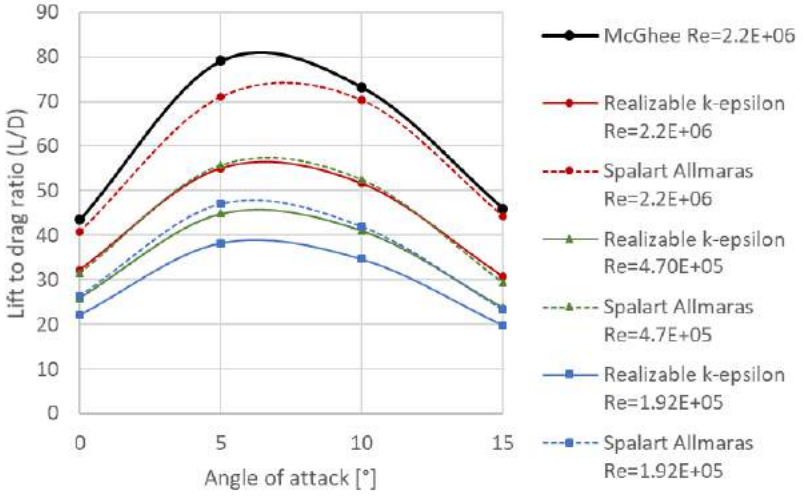

Figure 5.23: Comparison of the lift to drag ratio between the k-ε and the Spalart Allmaras turbulence model of a 2D airfoil at varying angle of attack

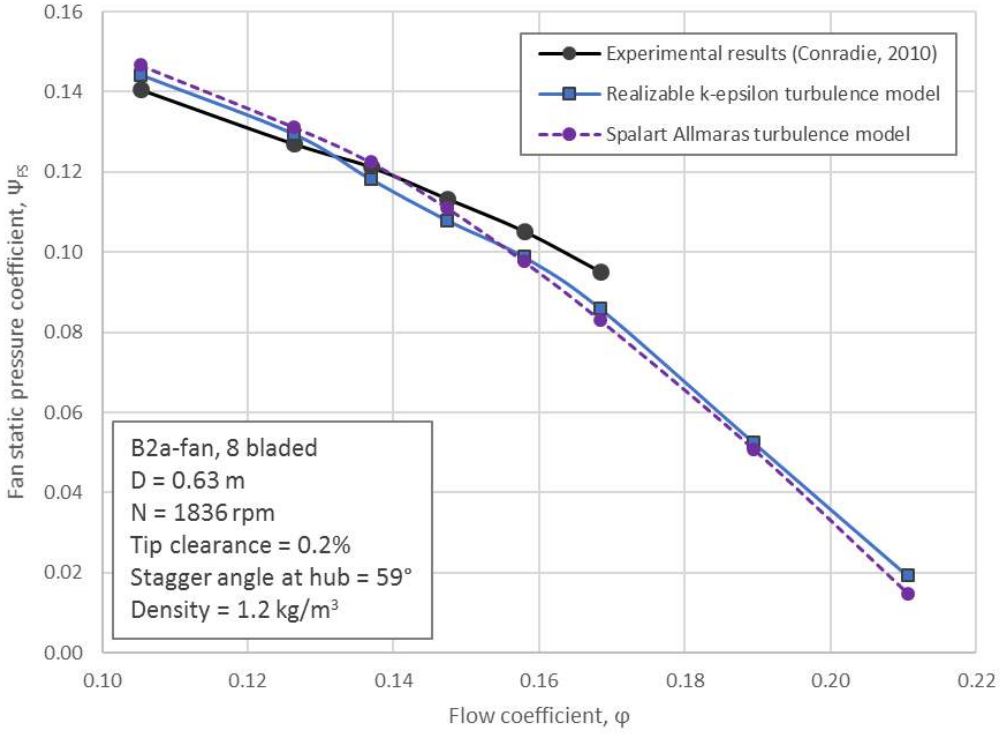

Figure 5.24: Comparison of the Spalart Allmaras model to the results of the Realizable k-epsilon and experimental model for the 0.63 m fan

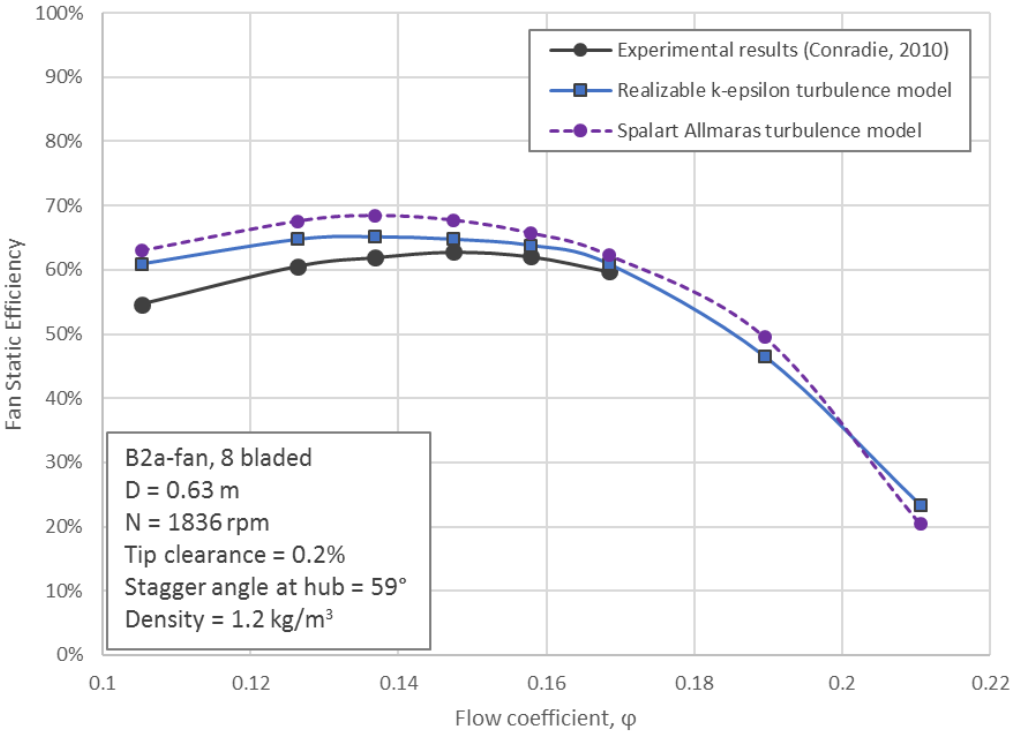

Figure 5.25: Comparison of the Spalart Allmaras model to the results of the Realizable k-epsilon and experimental model for the 0.63 m fan

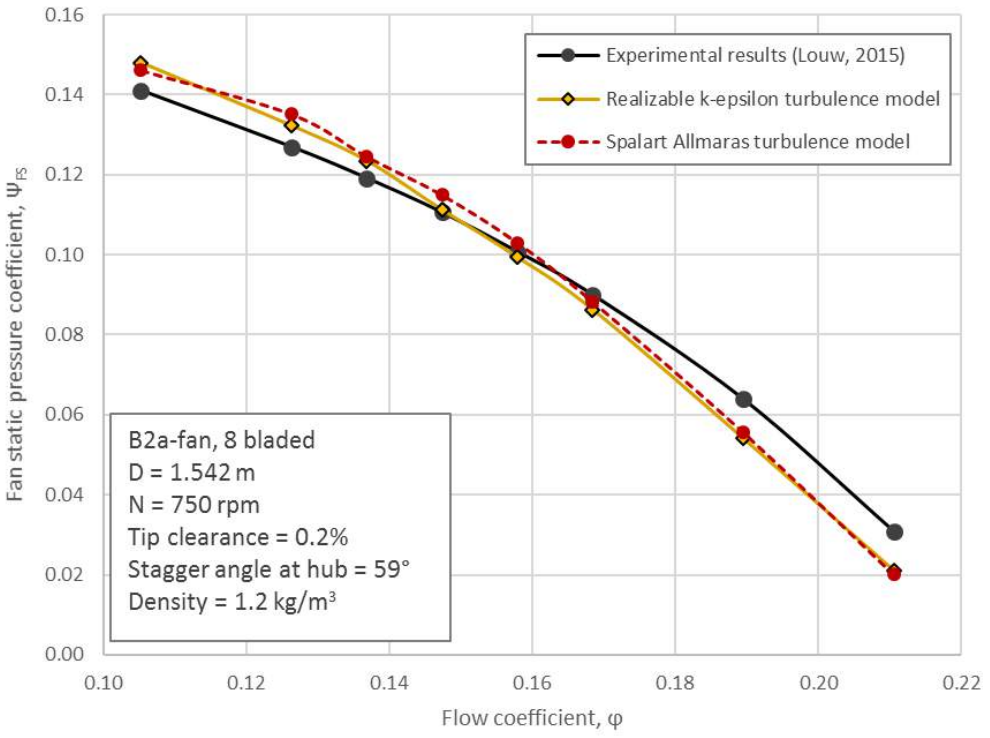

Figure 5.26: Comparison of the Spalart Allmaras model to the results of the Realizable k-epsilon and experimental model for the 1.542 m fan

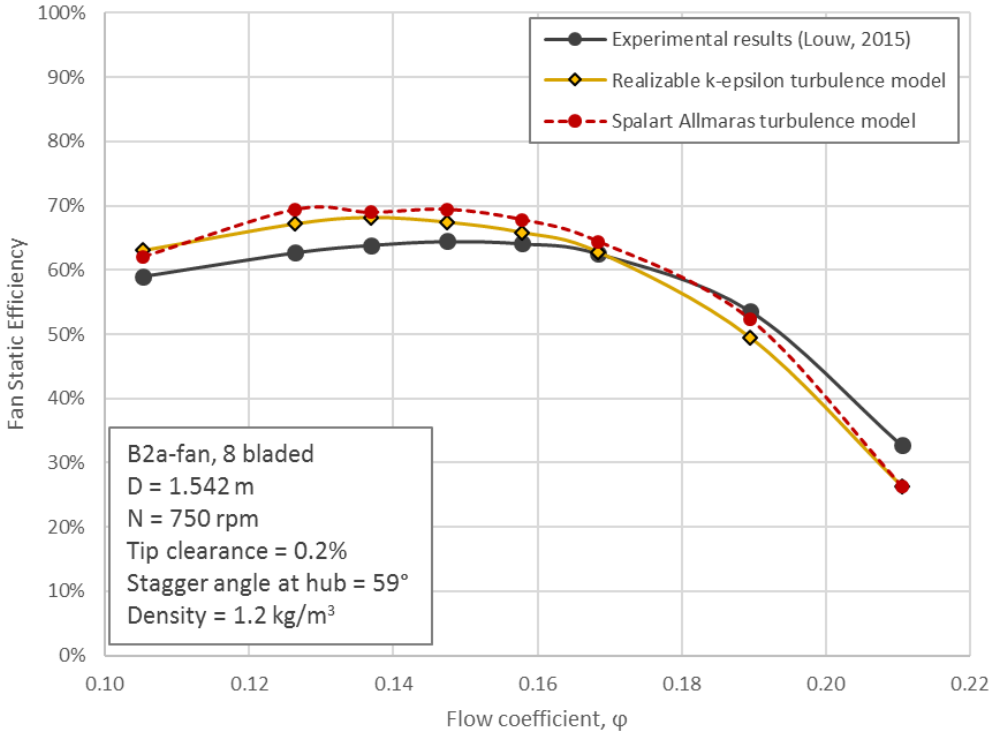

Figure 5.27: Comparison of the Spalart Allmaras model to the results of the Realizable k-epsilon and experimental model for the 1.542 m fan

The effect of Reynolds number on the lift and drag of the 2-dimensional airfoil was investigated. The Realizable k-ε turbulence model with a Standard wall function model is used in the two-dimensional analysis to create comparative results to the three-dimensional analysis of the fan. As shown in Figure 5.28, 5.29 & 5.30 the lift coefficient increases while the drag coefficient decreases with an increase in Reynolds number of the flow. Therefore the lift to drag ratio also increases as the Reynolds number increases. The results show that the effect of the Reynolds number on the magnitude of the lift and drag coefficient intensifies with an increase in angle of attack. This results in a large variation in lift and drag over the Reynolds number range for an airfoil at a high angle of attack. At a low angle of attack (0 degrees) the lift is near constant, while only a small decrease in drag occurs from a low to a high Reynolds number.

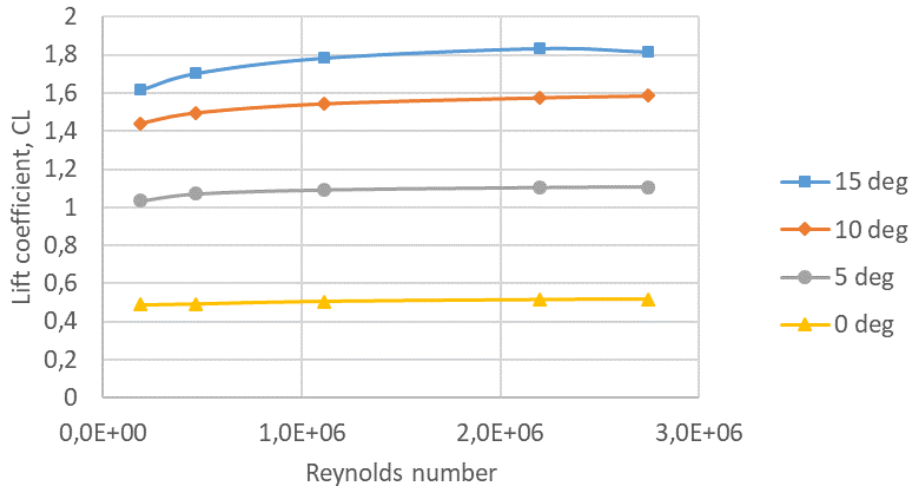

Figure 5.28: The effect of Reynolds and blade angle of attack on the lift coefficient using the Realizable k-ε turbulence model

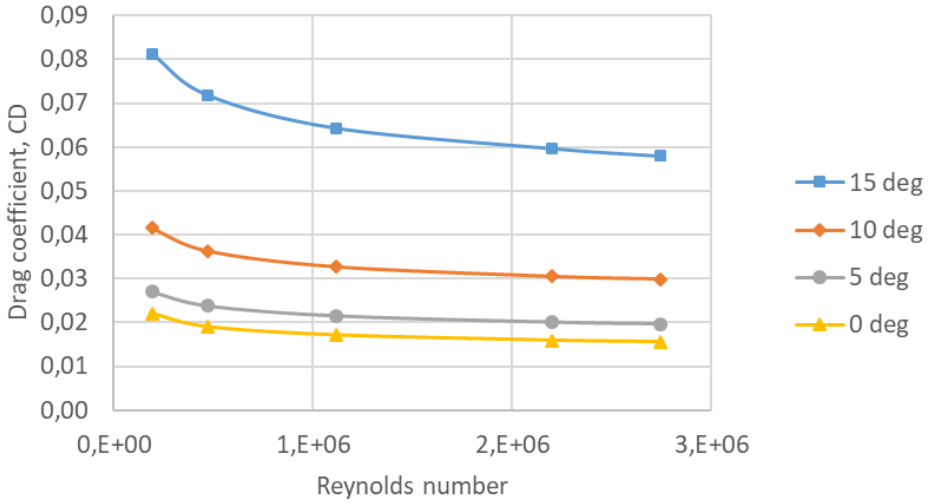

Figure 5.29: The effect of Reynolds and blade angle of attack on the drag coefficient using the Realizable k-ε turbulence model

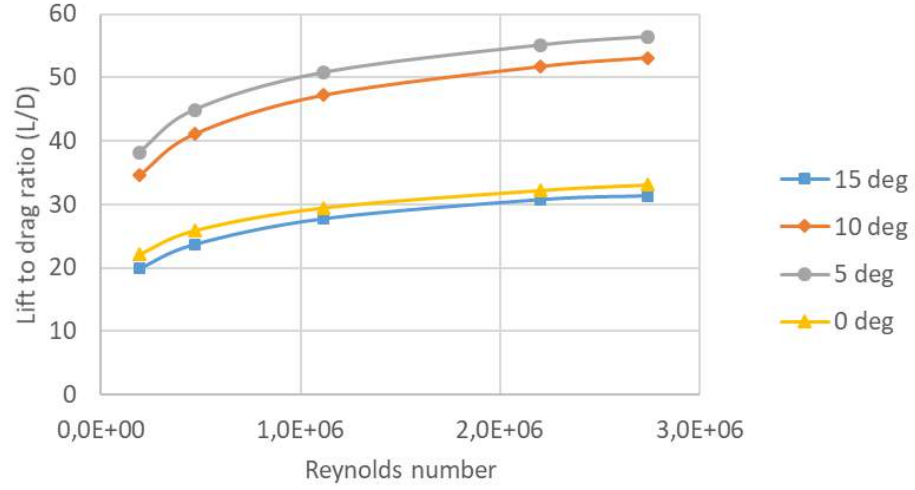

Figure 5.30: The effect of Reynolds and blade angle of attack on the lift to drag ratio using the Realizable k-ε turbulence model

5.5 Analysis of results

5.5.1 3-dimensional fan analysis

The present chapter investigates the accuracy of numerical analyses of axial fans of different sizes and Reynolds numbers. The B2a-fan was assessed and compared to experimental results obtained by Louw (2015) and Conradie (2010). The effect of fan size and Reynolds number is subsequently investigated. A 2-dimensional analysis of the lift and drag coefficient over an airfoil is also conducted, exploring the impact of different turbulence models and Reynolds number on the solution.

The results show a discrepancy between the numerical- and the experimental results at a volume flow rate smaller and higher than the volume flow rate of the fan's design point. The over- and under-prediction of fan static efficiency, shown in Figure 5.5, is analogous to a clockwise rotation of the fan curve around the design point of the fan. Interestingly, the same trend occurs for a change in blade setting angle, as shown in Figure 5.31. Similar to a decrease in blade setting angle, the numerical results of the 1.542 m and 0.63 m show an over-predion at a low flow rate and a under-prediction at a high flow rate. In addition the intersection point or 'rotational point' of the curve is at the design point ($\varphi = 0.168$ or 16 m^3/s) for both the 1.542 m and the 0.63 m results, as well as for the change in blade setting angle shown in Figure 5.31. In the study by Bruneau (1994) the blade was rotated to provide a variation in blade setting angle i.e. the angle between the blade and the plane perpendicular to the axis of rotation.

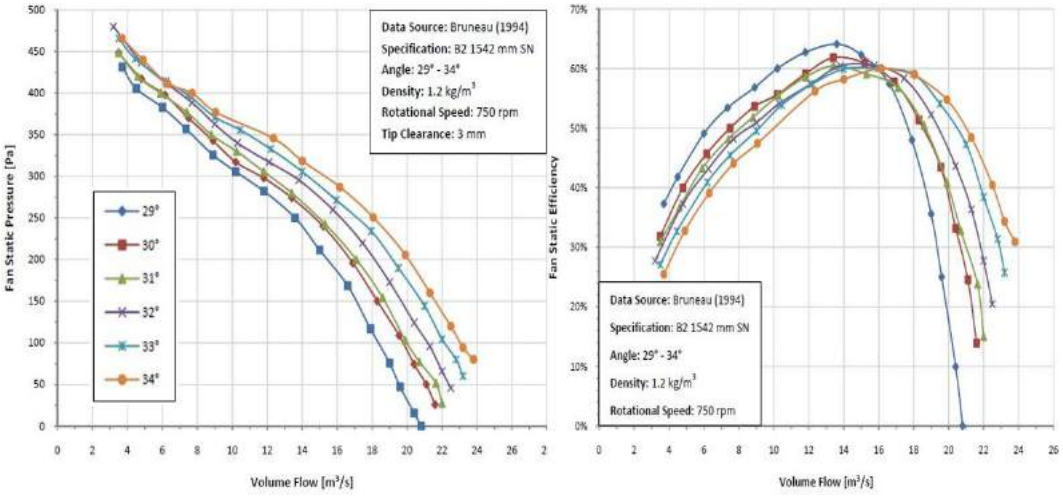

Figure 5.31: Effect of blade angle on the fan static pressure and -efficiency (Bruneau, 1994)

In the results by Bruneau (1994), shown in Figure 5.31, the decrease in blade setting angle results in a decrease in fan static pressure as well as an increase in fan static efficiency at a low flow rate and a decrease in fan static efficiency at a high flow rate. The same trend is also seen for other fan types, such as the B1, B2 and V fan, as shown in the study by van der Spuy *et al.* (2012). This shows that there might be a relation between the under- and over prediction at a high and low flow rate of the numerical study and the blade setting angle. As seen in Figure 5.31, a one degree change in angle has a significant impact on the results.

An explanation for the similarity of the numerical results to the results of the changed blade setting angle, is an under-prediction of the incidence losses by the numerical model. Given the flow condition shown in Figure A.6, a decrease in the blade setting angle (γ) causes a decrease in incidence angle (i) and angle of attack (α), which reduces the drag over the blade and results in an increase in fan static efficiency. The fan static efficiency thus increases with a decrease in blade setting angle for a volume flow rate lower than the volume flow rate of the maximum efficiency point (16 m^3/s). This is visible in Figure 5.31. For a flow rate larger than the flow rate of the maximum efficiency point, the relative velocity component (U_r), shown in Figure A.6, will lie left of the chord line, such that $\beta > \gamma$. An increase in volume flow past the volume flow rate of the peak efficiency point thus results in an increase in incidence angle, which results in increased drag over the blade and flow separation i.e. the incidence losses increase. A fan at a lower blade setting angle (γ) will thus reach its peak efficiency at a lower volume flow rate and will have a lower fan static efficiency for flow rates higher than the flow rate of the maximum efficiency point.

This suggests that the numerical model may be under-predicting the incidence losses, thus producing the same shift of the fan static efficiency curve as caused by the reduction in blade setting angle. At the same axial velocity (U_a) and rotational speed (U_c) the numerical results correlate to the results of a blade with a lower incidence angle (i), as demonstrated in Figure 5.31. The above reasoning does however require further investigation.

5.5.2 2-dimensional airfoil analysis

The two-dimensional analysis shows an increased deviation between the numerical and the experimental results with an increase in angle of attack. The angle of attack is the angle formed between the average relative velocity vector of the incoming and outgoing flow and the blade chord. As shown in Figure 5.32 (b), an increase in angle of attack (α), for a fan with a fixed blade setting angle and rotational speed (U_c), is caused by a decrease in axial velocity ($-\Delta U_a$), which

corresponds to a decrease in flow coefficient (φ). The dotted velocity triangles depict the flow at the peak efficiency point, which is, by judging the highest lift-to-drag ratio in the two-dimensional analysis shown in Figure 5.23, at a 5° angle of attack. An angle of attack below the peak efficiency angle of attack, as shown in Figure 5.32 (a), is achieved by increasing the axial velocity ($+\Delta U_a$) and hence, the flow coefficient. Therefore the results of the two-dimensional at a low angle of attack are comparable to the results at a high flow coefficient (φ) in the three-dimensional fan blade analysis and vice versa.

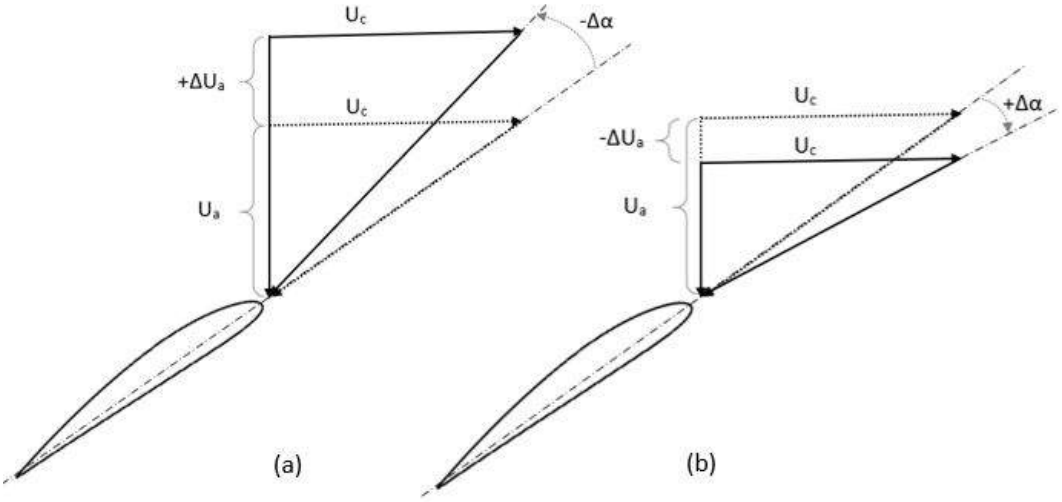

Figure 5.32: Effect of flow rate on the angle of attack

This means that the large deviation seen between the numerical- and the experimental results at a high angle of attack in the two-dimension analysis, translates to a large deviation in results at a low flow coefficient in the three-dimensional analysis. This confirms the theory of the over-prediction of the flow deviation and blockage by the numerical model at low flow coefficient, which in effect over-predicts the fan static pressure and efficiency at a low flow coefficient.

The unsteady and transient flow occurring at a low flow rate and thus at a high angle of attack is visible by the very high position of the drag curve at 15° in Figure 5.29. The drag coefficient at 15° is approximately three times higher than the drag coefficient at an angle of attack of 0°. The results in Figure 5.30 also show a large decrease in lift-to-drag ratio at a low Reynolds number for all angles of attack. This is possibly caused by the increased dominance of the laminar flow regime at a low Reynolds number.

The change in lift-to-drag ratio with Reynolds number, shown in Figure 5.30, for a two-dimensional analysis shows a strong similarity to the change in fan static efficiency with Reynolds number of the three-dimensional analysis, as shown in Figure 5.15. This shows that the fan static efficiency is related to the airfoil's lift-to-drag ratio. Radial flow occurring at a low flow rate and three-dimensional losses, such as tip clearance- and annulus losses, are not included in the two-dimensional analysis. Since Figure 5.15 is a plot of the maximum efficiency, a direct comparison of the two-dimensional analysis is the 5° angle of attack curve shown in Figure 5.30. The comparison shows that, while the three-dimensional analysis exhibits a small gradient of fan static efficiency to Reynolds number at a high Reynolds number, the two-dimensional analysis showed a noticeably higher gradient of lift-to-drag ratio to Reynolds number. This shows that three-dimensional losses, such as tip clearance- and annulus losses, have a greater impact on the fan static efficiency at a high Reynolds number than at a low Reynolds number.

Chapter 6

Conclusions and Recommendations

The overall objective of this investigation was to study the effect of scaling on the performance of axial flow fans for the purpose of forming a better understanding of the effects arising from scaling and to improve accuracy of fan scaling methods. The accuracy of an CFD analysis for the purpose of scaling was examined.

6.1 Concluding remarks

In order to fulfil the objectives, the study was subdivided into smaller investigations. The first investigation was set to determine and assess the parameters that influence the performance of axial flow fans and investigate their variation in magnitude and dominance with scaling. The effect of Reynolds number on fan performance was established and the losses present in the axial fan were identified and discussed.

The performance of the scaling formula derived by Pelz *et al.* (2012) was determined. The fan static efficiency of a 1.542 m diameter scaled fan model was determined by using the experimentally obtained fan performance of a 0.63 m diameter B2a-fan. The predicted results were compared to the experimental results of the 1.542 m fan. The down-scaling performance of the Pelz scaling method was also tested by using the experimental data of the 1.542 m B2a-fan and predicting the fan performance of a 0.63 m diameter fan. The results showed that the method over-predicts the change in efficiency in both the upscale and downscale scenarios.

The comparison of the Pelz scaling method to the numerical analysis showed that the Pelz scaling method performed better for case of scaling up, with the exception of the region close to the design point, as the numerical fan static ef-

ficiency curve intersects the experimental efficiency curve at the design point. The difference between the results of the Pelz scaling method and the experimental results is smaller than the difference between the numerical- and experimental results. Even though the results of both the numerical analysis and the Pelz scaling method showed significant deviation in comparison to the experimental results, for the case of scaling down, the deviation of the numerical results were smaller.

The relative accuracy of numerical analysis in relation to the fan performance was determined. For this investigation detailed CFD analyses of a 0.63 m, 1.542 m and a 9 m B2a-fan were conducted. The fan static pressure, -efficiency and fan power of the 0.63 m and 1.542 m fan were used to access the accuracy of the numerical analysis in comparison to experimental results. The effect of fan size and Reynolds number was investigated. The fan performance over a range of flow rates of a 0.63 m, 1.542 m and 9 m B2a-fan was assessed and a comparison was drawn between the fans. The results show that an increase in fan static efficiency and -pressure occurs for an increase in fan size and subsequently Reynolds number. The resultant difference between the 0.63 m and 1.542 m, and between the 1.542 m and 9 m diameter fan is approximately the same, even though the difference in size of the later is more than twice that of the 0.63 m and 1.542 m fan. This is attributed to the logarithmic trend of the Reynolds number effect on fan performance. Two additional B2a-fans with a diameter of 3.66 m and 7.32 m were modelled for an investigation of the Reynolds number effect on the fan static efficiency.

A prediction was made that the difference between the numerical- and experimental results indicate an under-prediction of the incidence losses by the numerical model. This prediction is based on the similarity in results to results obtained for a change in blade setting angle. Further research is however required for conclusive reasoning.

A two-dimensional numerical analysis was conducted to determine the accuracy of the turbulence models and determine the effect of Reynolds number on the lift and drag characteristics of an airfoil. The two-dimensional analysis showed an over-prediction of lift and drag by the Realizable k-ε turbulence model. The investigation showed that the Spalart Allmaras turbulence model produced more accurate results than the Realizable k-ε model for a range of Reynolds numbers. The Spalart Allmaras turbulence model was thus tested in the three-dimensional analysis of the B2a-fan, for which it produced no significant decrease in deviation between the numerical- and experimental results. This is attributed to the modest performance of the turbulence model in three-dimensional flow problems. The effect of Reynolds number on the lift-to-drag ratio of an airfoil showed that purely three-dimensional losses have a greater effect on fan performance at a high Reynolds number than at low Reynolds

number flow.

6.2 Recommendations for future work

Even though the study reached its objectives a need for further research exists in the following areas:

- Even though the results of the 0.63 m were proven to be applicable for this study, it is recommended to repeat the experimental test of the 0.63 m diameter fan to extend the results to a higher flow rate range. The fan should also be tested at a 0.2 % relative tip clearance to be directly comparable to the 1.542 m diameter B2a-fan.
- A research potential exists concerning the Pelz scaling method. A future investigation of the applicability of the Pelz method on a variety of fan models can be conducted, testing the machine dependency of the scaling method.
- A more detailed analysis of individual losses in an axial fan and the similarity of their magnitude in comparison to a CFD model can be investigated.

List of References

ANSYS Fluent Inc. (2009 April). Moving zones. Available at: `http://studylib.net/doc/10035486/moving-zones-in-ansys-cfx-tutorial`.

ANSYS Fluent Inc. (2015 February). Lecture 7 -turbulence modeling. Lecture notes.

ANSYS Fluent Inc. (2017). *ANSYS Fluent 17.0 Users guide*. ANSYS Inc.

Augustyn, O.P.H. (2013). *Experimental and numerical analysis of axial flow fans*. Master's thesis, University of Stellenbosch.

Bahrami, M. (2009 February). Lecture notes: Introduction and properties of fluids. [Online]. Available at: `http://www.sfu.ca/ mbahrami/ensc283.html`. Published by Simon Fraser University.

British Standard (2007). *Industrial fans - Performance testing using standardized airways*. 848-1:2007. British Standards Institution, London, United Kingdom.

Bruneau, P. (1994). *The design of a single rotor axial flow fan for a cooling tower application*. Master's thesis, University of Stellenbosch.

Cengel, Y.A. and Boles, M.A. (2011). *Thermodynamics - An engineering approach*, chap. 6. 7th edn. McGraw-Hill.

Cengel, Y.A. and Cimbala, J.M. (2010). *Fluid Mechanics - Fundamentals and Applications*. 2nd edn. McGraw-Hill.

Conradie, P. (2010). *Edge fan performance in air-cooled condensers*. Master's thesis, University of Stellenbosch.

Denton, J. (1993 September). Loss mechanisms in turbomachines. In: *International Gas Turbine and Aeroengine Congress and Exposition*. Cambridge University Engineering Department.

Grimes, R., Walsh, E., Quin, D. and Davies, M. (2005 November). Effect of geometric scaling on aerodynamic performance. *AIAA Journal*, vol. 43, no. 11, pp. 2293–2298.

Hess, M. (2010). *Aufwertung bei Axialventilatoren - Einfluss von Reynolds Zahl, Rauheit, Spalt und Betriebspunkt auf Wirkungsgrad und Druckziffer*. Ph.D. thesis, Technische Universität Darmstadt.

Hutton, S. (1954). Component losses in kaplan turbines and the prediction of efficiency from model tests. *Proceedings of the Institution of Mechanical Engineers*, vol. 168, no. 1, pp. 743–762.

Kröger, D.G. (1998). *Air-cooled heat exchangers and cooling towers*, chap. 7, pp. 711–715. D.G. Kröger.

Lennon, S. (2011 August). Advances in dry cooling deployed at south african power stations. In: *2011 Summer Seminar*. Electric Power Research Institute.

Louw, F., Bruneau, P., von Backström, T. and van der Spuy, S. (2012 June). The design of an axial flow fan for application in large air-cooled heat exchangers. In: *ASME Turbo*.

Louw, F.G. (2015). *Investigation of the flow field in the vicinity of an axial flow fan during low flow rates*. Master's thesis, University of Stellenbosch.

McGhee, R. and Beasley, W. (1976). Effects of thickness on the aerodynamic characteristics of an initial low-speed family of airfoils for general aviation applications. Tech. Rep., National aeronautics and space administration (NASA), Langley research center, Hampton, Virginia, USA.

McPherson, M. (2009). *Subsurface ventilation and environmental engineering*, chap. 10, pp. 2–49. 2nd edn. Chapman & Hall, London.

Moody, L.F. (1926). The propeller type turbine. *ASCE Trans*, vol. 89, p. 628.

Mühlemann, E. (1948). Zur aufwertung des wirkungsgrades von uberdruckwasserturbinen. *Schweizerische Bauzeitung*, vol. 66, no. 24.

Ndebele, P. (2015). Technology innovations: Solar grid-based (csp). In: *South African International Renewable Energy Conference (SAIREC)*. South Africa Solar Thermal and Electricity Association (SASTELA).

Palmer, T. and Ainslie, A. (2006). Country pasture/forage resource profiles - south africa.
Available at: `http://www.fao.org/ag/agp/agpc/doc/counprof/southafrica.htm`

Patdiwala, U., Patel, H. and Parmar, P. (2014). A review on tip clearance flow and secondary flow losses in linear turbine cascade. *IOSR Journal of Mechanical and Civil Egineering*, vol. 11, pp. 33–37.

Pelz, P. and Stonjek, S. (2013). A second order exact scaling method for turbomachinery performance prediction. *International Journal of Fluid Machinary and Systems*, vol. 6, no. 4, pp. 177–187. ISSN 1882-9554.

Pelz, P.F. and Hess, M. (2010 April). Scaling friction and inertia losses for the performance prediction of turbomachines. *13th International Symposium on Transport Phenomena and Dynamics of Rotating Machinery (ISROMAC-13)*, , no. 122.

Pelz, P.F., Stonjek, S. and Matyschok, B. (2012). The influence of reynolds number and roughness on the efficiency of axial and centrifugal fans. In: *Fan 2012*.

Pfleiderer, C. (1955). Der strömungsmechanismus im laufrad und die schaufelarbeit. In: *Die Kreiselpumpen für Flüssigkeiten und Gase*, pp. 101–142. Springer.

Pierce, W. (2008). *Evaluation and performance prediction of a wind turbine blade*. Master's thesis, University of Stellenbosch.

Rhoden, H. (1952 June). Effects of reynolds number on the flow of air through a cascade of compressor blades. paper 2919, Cambridge University.

Saul, S. and Pelz, P. (2016). Influence of compressibility on fan efficiency and fan effiency scaling. In: *International Rotating Equipment Conference*.

Spalart, P.R., Allmaras, S.R. *et al.* (1994). A one equation turbulence model for aerodynamic flows. *RECHERCHE AEROSPATIALE-FRENCH EDITION-*, pp. 5–5.

Staufer, F. (1925). Einflüsse auf den wirkungsgrad von wasserturbinen. *Z. VDI*, vol. 69, pp. 415–415.

Stonjek, S. and Pelz, P. (2014 June). Introduction of an universal scale-up method for the efficiency of axial and centrifugal fans. In: *ASME Turbo Expo 2014*.

Symscape (2013). Polyhedral, tetrahedral, and hexahedral mesh comparison. [Online]. Available at: `http://www.symscape.com/polyhedral-tetrahedral-hexahedral-mesh-comparison`.

Teicher, U., Rosenbaum, T., Nestler, A. and Brosius, A. (2017). Characterization of the surface roughness of milled carbon fiber reinforced plastic structures. In: *Cirp Conference on Composite Materials Parts Manufacturing*, pp. 199–203.

Tindale, M. and Sagris, T. (2013). Direct dry cooling in the power sector. *Managing Water Use in Scarce Environments*, pp. 78–79.

van der Spuy, S.J., von Backström, T.W., Kröger, D.G. and Bruneau, P.R. (2012). Testing an axial flow fan designed for air-cooled steam condenser application. In: *Fan 2012*.

Versteeg, H. and Malalasekera, W. (2007). *An introduction to computational fluid dynamics- The finite volume method*. 2nd edn. Pearson Education Limited. ISBN 978-0-13-127498-3.

Appendices

Appendix A

Fan geometry and performance data

The B2a-fan is modelled in the present study. The fan is a modification of the B2-fan, designed by Bruneau (1994). The modification is detailed by Louw (2015), who cylindrically fitted the airfoils making up the fan blade. Louw (2015) also corrected dimensional errors that were present in the manufactured B2-fan model, thus reducing the discrepancy between the numerical- and experimental results. The difference between the B2-fan and the B2a-fan is shown in Figure A.1. The dimensions of the fan are given in section A.1. A detailed description of the airfoil and the blade characteristics are given thereafter.

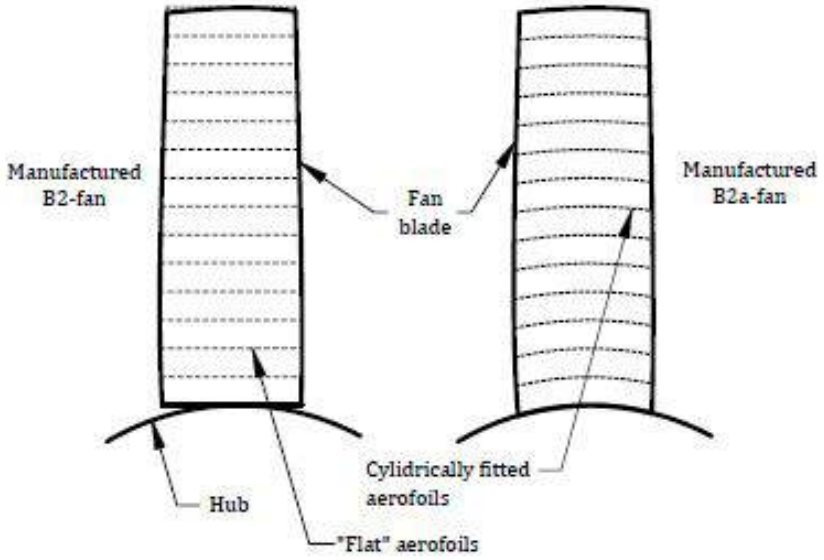

Figure A.1: Difference between the B2- and the modified B2a-fan blade (Louw, 2015)

A.1 Fan dimensions

A schematic of the B2a-fan is shown in Figure A.2 below.

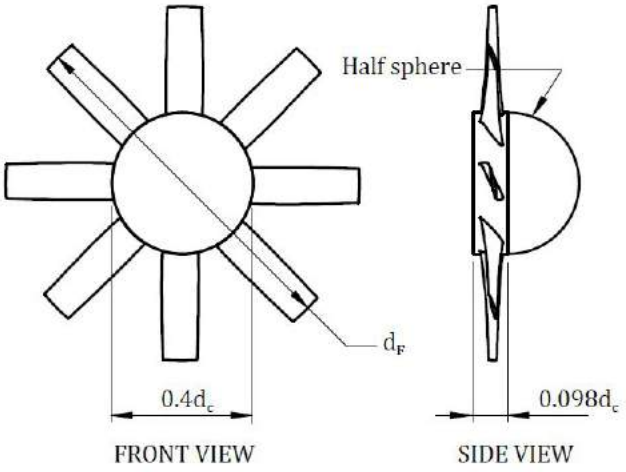

Figure A.2: Schematic of the B2a-fan (Louw, 2015)

The specifications of the B2a-fan are as follows:

Casing diameter:	1.542 m
Hub diameter:	0.6168 m
Number of blades:	8
Chord length at the hub :	0.184 m
Chord length at the tip:	0.153 m
Hub-tip ratio:	0.4
Tip clearance:	3 mm (0.2%)
Rotational speed:	750 rpm
Stagger angle (ζ) at the hub:	59°

The B2a-fan is made up of a combination of the NASA LS 0413 and the LS 0409 airfoil (McGhee and Beasley, 1976), thus creating a thick blade at the hub, using the LS 0413 airfoil ($\Delta y/x = 0.13$), thinning towards the tip using the LS 0409 ($\Delta y/x = 0.09$). The airfoil profile is pictured in Figure A.3.

The radially stacked airfoils that make up the geometry of the B2a-fan are shown in Figure A.3, showing the twist of the blade in the span wise direction. The variation of the blade angle (Defined in this thesis as γ but given in the

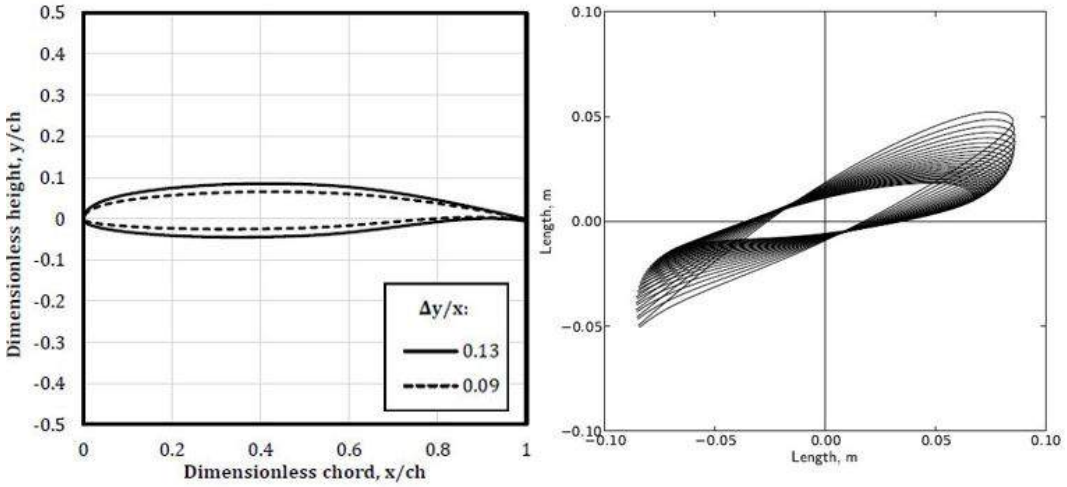

Figure A.3: Profile view of the LS 0413 and 0409 airfoil airfoil and the blade twist of the B2a-fan (Louw *et al.*, 2012)

figure as β') and chord length (ch) along the blade span is described by the plot in Figure A.4, where the blade angle is the angle between the chord and the plane of rotation. Thus:

$$\beta' = 90° - \zeta \ [°] \tag{A.1}$$

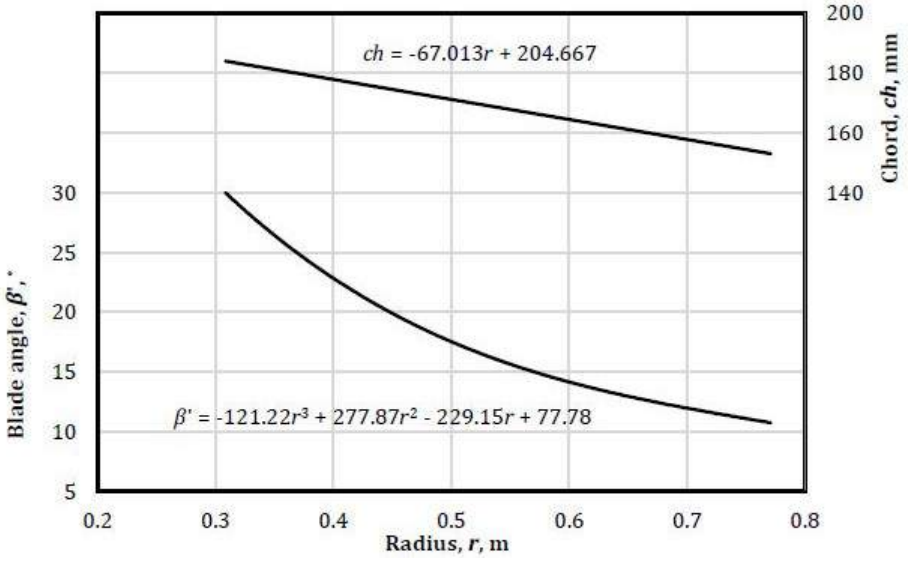

Figure A.4: Change in blade angle and chord length along the span of the B2a-fan blade (Louw, 2015)

The lift and drag characteristic of the LS 0413 airfoil is given by McGhee and Beasley (1976) and is shown in Figure A.5.

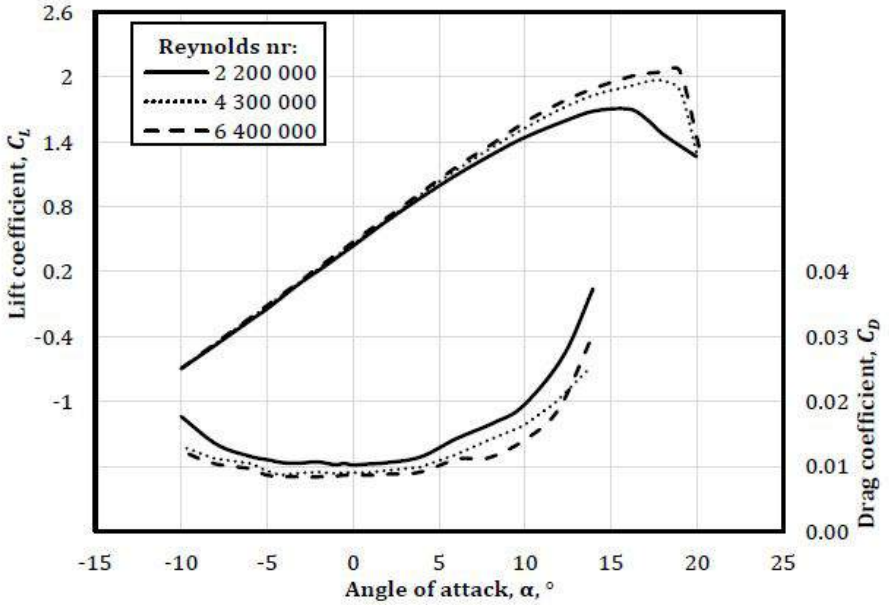

Figure A.5: The lift- and drag coefficient of the NASA LS 0413 airfoil for a variation in angle of attack and Reynolds number (McGhee and Beasley, 1976)

The experimental test of the LS 0413 airfoil, conducted by McGhee and Beasley (1976), used a fixed transition at x/c = 0.075. The centre of rotation was set at 0.25 ch from the leading edge the airfoil.

A sketch of an airfoil with the velocity triangle and definition of the various angles is shown in Figure A.6.

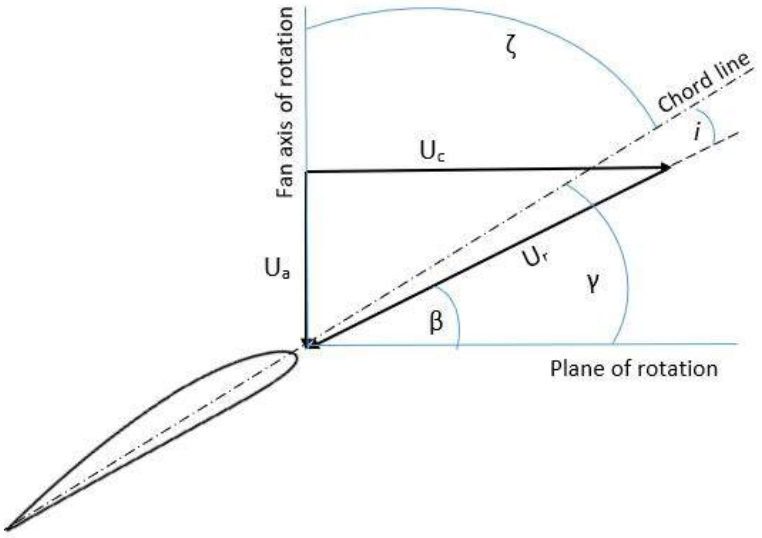

Figure A.6: Blade angle nomenclature for a high flow rate condition

A.2 Scaling formula performance

The comparison between the numerical results of the 1.542 m diameter B2a-fan and the results predicted for the 1.542 m fan by the Pelz scaling method when up-scaling from 0.63 m diameter fan is shown in Figure A.7. The results show that the numerical results of the 1.542 m fan has a greater deviation to the experimental results than the predicted results of the Pelz scaling formula. An exception is for a flow coefficient close to the design point, for which the numerical analysis produces a far greater conformity with the experimental results.

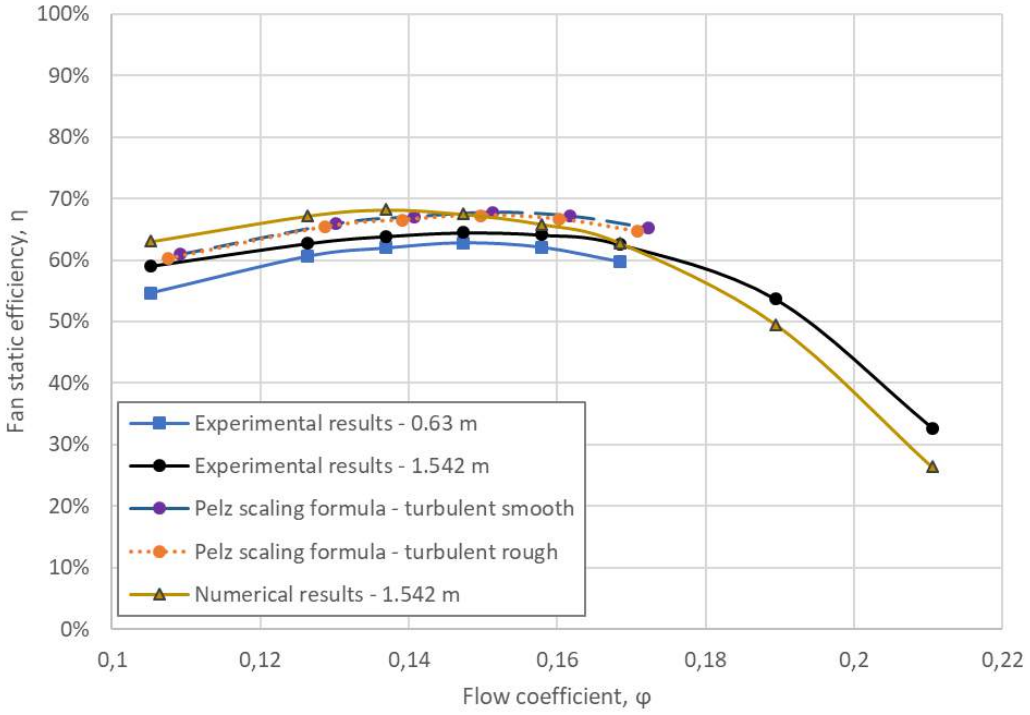

Figure A.7: Comparison of the performance prediction by the Pelz scaling formula to the numerical results for the 1.542 m diameter fan

Figure A.8 shows that the numerical results of the 0.63 m B2a-fan over-predict the fan static efficiency, compared to the experimental results of the 0.63 m fan, while the results of the Pelz scaling formula under-predict the efficiency when down-scaling from a 1.542 m diameter fan. The difference between the numerical- and the experimental results is smaller than the difference from the results of the Pelz scaling formula to the experimental results.

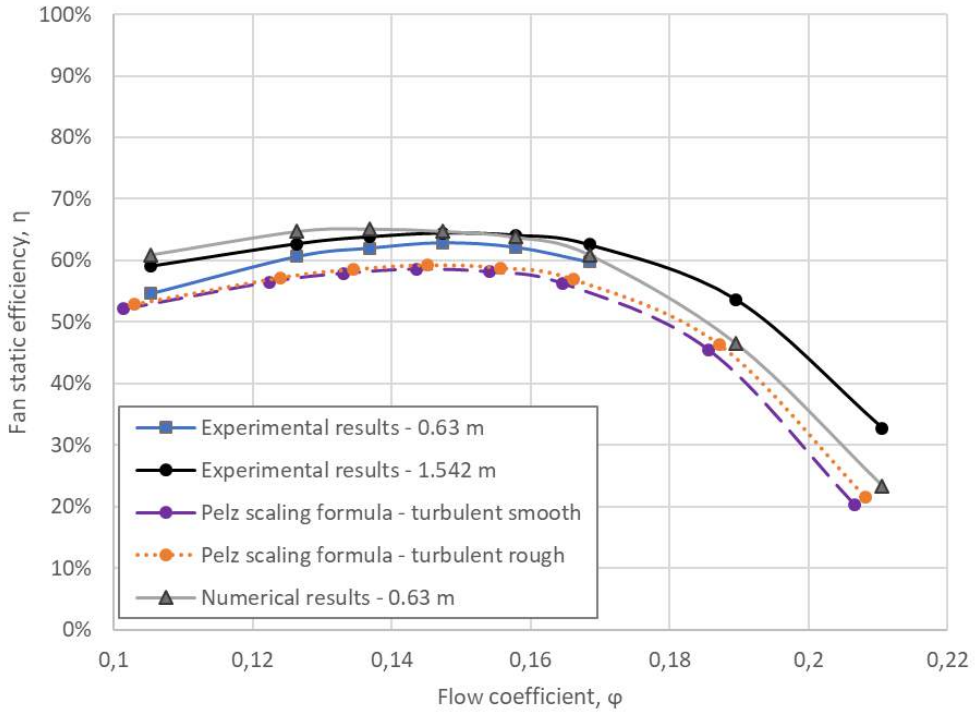

Figure A.8: Comparison of the performance prediction by the Pelz scaling formula to the numerical results for the 0.63 m diameter fan

Appendix B

Sample Calculation

B.1 Volume- & mass flow rate scaling

A sample calculation of the mass flow inlet for the 0.63 m and the 9 m fan at the design point of 16 m^3 is given below:

Rotational speed of the 0.63 m fan:

$$\begin{aligned} (\omega r)_p &= (\omega r)_m \\ 78.54\left(\frac{1.542}{2}\right) &= \omega_m\left(\frac{0.63}{2}\right) \\ \Rightarrow \omega_m &= 192.236\ rad/s \end{aligned} \tag{B.1}$$

$$\frac{\omega_p}{\omega_m} = \frac{N_p}{N_m} \tag{B.2}$$

Scaled volume flow rate ($\dot{V}$) of the 0.63 m fan:

$$\begin{aligned} \dot{V}_m &= \frac{\dot{V}_p}{\left(\frac{N_p}{N_m}\right)\left(\frac{D_p}{D_m}\right)^3} \\ \dot{V}_m &= \frac{16}{\left(\frac{78.54}{192.236}\right)\left(\frac{1.542}{0.63}\right)^3}\ \left[m^3/s\right] \\ \Rightarrow \dot{V}_m &= 2.671\ m^3/s \end{aligned} \tag{B.3}$$

Scaled mass flow rate ($\dot{m}$) of the 0.63 m fan for a single blade section:

$$\begin{aligned} \dot{m} &= \frac{\rho\ \dot{V}_m}{no\ of\ blades} \\ \dot{m} &= \frac{1.2\ \dot{V}_m}{8} \\ \Rightarrow \dot{m} &= 0.4006\ kg/s \end{aligned} \tag{B.4}$$

Rotational speed of the 9 m fan:

$$\begin{aligned} (\omega r)_p &= (\omega r)_m \\ 78.54\left(\frac{1.542}{2}\right) &= \omega_m\left(\frac{9}{2}\right) \\ \Rightarrow \omega_m &= 13.45652\ rad/s \end{aligned} \tag{B.5}$$

$$\frac{\omega_p}{\omega_m} = \frac{N_p}{N_m} \tag{B.6}$$

Scaled volume flow rate ($\dot{V}$) of the 9 m fan:

$$\begin{aligned} \dot{V}_m &= \frac{\dot{V}_p}{\left(\frac{N_p}{N_m}\right)\left(\frac{D_p}{D_m}\right)^3} \\ \dot{V}_m &= \frac{16}{\left(\frac{78.54}{13.45652}\right)\left(\frac{1.542}{9}\right)^3} \\ \Rightarrow \dot{V}_m &= 545.05\ m^3/s \end{aligned} \tag{B.7}$$

Scaled mass flow rate ($\dot{m}$) of the 9 m fan for a single blade section:

$$\begin{aligned} \dot{m} &= \frac{\rho\ \dot{V}_m}{no\ of\ blades} \\ \dot{m} &= \frac{1.2\ \dot{V}_m}{8} \\ \Rightarrow \dot{m} &= 81.7575\ kg/s \end{aligned} \tag{B.8}$$

The scaled volume flow rate and subsequent mass flow rate at off-design flow rates for the 0.63 m, 1.542 m and the 9 m diameter fan is given in Table B.1. A numerical assessment of two additional fans with a diameter of 12 ft (3.658 m) and 24 ft (7.315 m) was conducted, as described in Section 5.3. The volume- and mass flow rate, based on Equations B.1 - B.4, is given in Table B.2.

Table B.1: The volume flow rate and subsequent mass flow rate of the different sizes of B2a-fans

0.63 m		1.542 m		9 m	
Vol. flow	$\dot{m}$	Vol. flow	$\dot{m}$	Vol. flow	$\dot{m}$
1.6692	0.2504	10	1.5	340.6562	51.0984
2.0031	0.3005	12	1.8	408.7874	61.3181
2.1700	0.3255	13	1.95	442.8530	66.4280
2.3369	0.3505	14	2.1	476.9187	71.5378
2.5038	0.3756	15	2.25	510.9843	76.6476
2.6707	0.4006	16	2.4	545.0499	81.7575
3.0046	0.4507	18	2.7	613.1811	91.9772
3.3384	0.5008	20	3	681.3124	102.1969

Table B.2: The volume flow rate and subsequent mass flow rate of the 12 and 24 ft B2a-fan

1.542 m		12 ft (3.66 m)		24 ft (7.32 m)	
Vol. flow	$\dot{m}$	Vol. flow	$\dot{m}$	Vol. flow	$\dot{m}$
12	1.80	67.516	10.127	270.067	40.510
13	1.95	73.142	10.971	292.572	43.886
14	2.10	78.768	11.815	315.078	47.262

B.2 Reynolds number

Using Equation 2.1 the Reynolds number of the 0.63 m, 1.542 m and the 9 m fan is determined. The Reynolds number at the hub and the tip of the blade is calculated to determine the Reynolds number range over the span of the blade.

$$
\begin{aligned}
1.20\,(10^5) &< Re_{\,0.63m} &< 2.49\,(10^5)\\
2.93\,(10^5) &< Re_{\,1.542m} &< 6.09\,(10^5)\\
6.95\,(10^5) &< Re_{\,3.66m} &< 14.45\,(10^5)\\
13.9\,(10^5) &< Re_{\,7.32m} &< 28.90\,(10^5)\\
17.10\,(10^5) &< Re_{\,9m} &< 35.56\,(10^5)
\end{aligned}
$$

Appendix C

Mesh dependency study

A mesh dependency study for the computational domain is conducted. The Realizable k-ε turbulence model with the *Standard* wall function was used for the numerical analysis of the B2a-fan. The model requires a y+ value in the range: 30<y+<300.

The mesh dependency study was conducted at the design flow rate of the fan ($\varphi = 0.168$). As mentioned in Chapter 4, the outlet sub-domain is divided into three zones, with each zone having a different mesh density. The mesh dependency of each zone was individually assessed. The optimum mesh density of an individual zone was determined and subsequently used for the mesh dependency study of the next zone. The mesh density of each zone was increased and decreased by 40%. The results of the mesh dependency study of the outlet sub-domain is shown in Table C.1 - C.3. Zone 1 is immediately upstream of the blade domain and zone 3 is the zone furthest away from the blade domain.

Table C.1: Mesh dependency of the Zone 1 in the outlet sub-domain

Zone 1 mesh dependency		
No. of Elements	P_{fs}	η
7120	206.64	66.58 %
11860	206.66	66.56 %
16600	206.74	66.59 %

The results of the mesh dependency study showed a very small difference in fan static pressure and -efficiency of the different mesh densities. The original mesh, which is the middle value in each mesh dependency study, is thus used.

Table C.2: Mesh dependency of the Zone 2 in the outlet sub-domain

Zone 2 mesh dependency		
No. of Elements	P_{fs}	η
820529	206.43	66.50 %
1366071	206.66	66.56 %
1910399	206.33	66.66 %

Table C.3: Mesh dependency of the Zone 3 in the outlet sub-domain

Zone 3 mesh dependency		
No. of Elements	P_{fs}	η
1088849	206.70	66.57 %
1807317	206.66	66.56 %
2536056	206.49	66.55 %

The mesh dependency results of the blade passage are shown in Table C.4.

Table C.4: Mesh dependency of the blade passage sub-domain

Blade passage mesh dependency		
No. of Elements	P_{fs}	η
396348	189.82	62.84 %
661248	189.73	62.80 %
932136	189.16	62.60 %

The mesh dependency study of the blade passage domain showed a very small change in fan performance therefore the original mesh with 661248 elements is used. A 0.2 % change in efficiency exist between the original mesh and a 40 % finer mesh.